IKE Institut für Kernenergetik
und Energiesysteme

THREE-DIMENSIONAL MODELING AND SIMULATION OF VAPOR EXPLOSIONS IN LIGHT WATER REACTORS

Maxim Schröder

August 2012 **IKE 2-150**

Universität Stuttgart

IKE Institut für Kernenergetik und Energiesysteme

Three-dimensional modeling and simulation of vapor explosions in Light Water Reactors

von der Fakultät Energie-, Verfahrens- und Biotechnik der Universität Stuttgart zur Erlangung der Würde eines Doktor-Ingenieurs (Dr.-Ing.) genehmigte Abhandlung

vorgelegt von

Maxim Schröder

geboren in Temirtau/Kasachstan

Hauptberichter: Prof. Günter Lohnert, Ph.D

Mitberichter: Prof. Dr.-Ing. Eberhard Göde

Tag der mündlichen Prüfung: 6. Juli 2012

ISSN – 0173 – 6892

August 2012 IKE 2-150

Universität Stuttgart

Acknowledgement

I would like to thank most sincerely Manfred Bürger for his considerate and patient support and guidance during my PhD work at IKE. He encouraged me to think independently, to see globally and to identify matters of substance. The experience he shared with me was paramount in helping me find my long-term career goals.

I would also like to express my gratitude to my advisor Professor Lohnert, who provided me with a technical insight and a practical view of nuclear science. Our discussions were always fruitful and stimulating in advancing my knowledge in the nuclear field.

Michael Buck was also essential to the success of this work by his assistance, friendship and backing in providing me with a wide breadth of experience in numerical analysis and model development. I am also very grateful for the friendly help of Georg Pohlner, with whom I worked closely in resolving many problems.

Finally and most importantly, I would like to thank my beloved wife Olga. Her support, motivation, patience and love have carried me through the challenging time of my graduate studies.

Abstract

Steam explosions can occur during a severe accident in light water nuclear reactors with the core melting as the consequence of interaction of molten core materials with water inside the reactor pressure vessel (in-vessel steam explosions), or after a failure of the reactor vessel due to the release of molten materials into the reactor cavity likely filled with water (ex-vessel steam explosions). Such steam explosions may significantly increase risks of severe accidents threatening the integrity of the reactor pressure vessel, of the primary containment and possibly even of the reactor building. The loss of integrity of the primary containment and reactor building would cause a release of large amounts of fission products into the atmosphere and a contamination over a large area. Eliminating the risk of steam explosions in reactor accident scenarios would contribute to enhancing the effectiveness of accident management procedures, e.g. concept for the external cooling of the reactor vessel or the cooling of the molten core in the flooded reactor cavity.

The main parameters influencing the outcome of a strong steam explosion are a limitation of the fragmented melt mass mixing with water, the melt jet fragmentation, the void buildup during premixing, the solidification at the surface of melt drops during the premixing and pressure escalations during detonation. Asymmetries caused by geometrical constraints (e.g. wall proximity, distributed melt pouring) are likely during an accident with core melting and can have a strong impact on the explosion strength.

Previously, asymmetric configurations have been investigated with two-dimensional models using 2D approximations. Until now, open questions concerning the fragmentation of the melt, the mixing phase with water, the extent of the mixing region and pressure increases under asymmetric conditions remained due to the uncertainties existing with the approximated approach. This led to unsatisfactory answers as to the role of geometrical restrictions. In order to give a more adequate solution to the problem and be able to predict the explosion strength in a conservative manner, the two-dimensional premixing and explosion codes IKEJET/IKEMIX and IDEMO were extended to 3D in the present work. Additional modeling improvements have been made with regard to applicability to real reactor conditions. The enhancements focus in particular on the breakup of thick melt jets in deep water pools and on the solidification of melt fragments during the mixing phase with water.

Asymmetries and their impact on the formation of explosive mixtures were investigated using the extended program codes. Variations to the melt delivery, pool depth and melt pouring configuration are considered. The melt fragmentation, void production, extent of the mixing zone due to geometrical constraints and the loads on adjoining structures are discussed in detail. The focus is on the assessment of

three-dimensional effects in the mixing and detonation phases. In this regard, two- and three-dimensional calculations were performed for each configuration. An investigation of the influence of the 3D geometry, i.e. geometrical restrictions on mixing, extent and distribution of melt and coolant, is discussed. Pressure loads and impulses on adjoining structures are obtained and the results are critically discussed. The calculations performed show the capability of the codes to correctly represent the main aspects of premixing and explosion stages of steam explosion in non-symmetrical scenarios and to adequately predict the pressure loads on the adjoining structures.

Kurzfassung

Effektive Kühlmassnahmen zur Milderung der Folgen schwerer Störfälle mit Kernschmelze in Leichtwasserreaktoren erfordern den Einsatz von Wasser auch noch in späten Phasen des Unfallablaufs. Hierbei kann es zum Kontakt von Kernschmelze und Wasser kommen. Hier ergibt sich potentiell ein erhöhtes Risiko von Dampfexplosionen. Diese können den Unfallablauf durch Gefährdung der benachbarten Strukturen erheblich verschärfen und zum Integritätsverlust des Reaktordruckbehälters oder des Primärcontainments führen. Es käme zu einer erheblichen Freisetzung radioaktiver Stoffe in die Umgebung und zu einer unmittelbaren Gefährdung der Menschen. Ein Ausschluss kritischer Wirkungen von Dampfexplosionen würde generell eine günstigere Beurteilung von Kühlungsmöglichkeiten mit Wasser erlauben uns so zusätzlich Optionen für Massnahmen des Accident-Managment eröffnen, wie z.B. das Konzept der Aussenkühlung des Reaktordruckbehälters oder das Konzept der Kühlung von ausgetretener Schmelze in einem Wasser-Pool in der Reaktorgrube.

Das Hauptziel der Arbeit ist es, den Effekt von Asymmetrien auf zentrale Aspekte (wie z.B. die Fragmentierung von Schmelzestrahlen, Voidbildung, Erstarrung der Schmelzetropfen in der Vorvermischung sowie Druckeskalationen in der Explosionsphase) in Reaktoranwendungen zu untersuchen. Hierfür wurden im Rahmen der Dissertation die bestehenden zweidimensionalen Programmcodes zur Vorvermischung und Detonation auf 3D erweitert. Zusätzlich wurden die Modelle hinsichtlich der Anwendbarkeit auf Reaktorszenarien weiterentwickelt. Zwei wichtige Punkte sind hierbei die Fragmentierung von Schmelzestrahlen und die Erstarrung von Schmelzetropfen. Die Fragmentierung bestimmt die Grösse des Schmelzetropfens und beeinflusst somit die Voidbildung und die Entwicklung der relativen Krustedicken an den Schmelzetropfen in der Vorvermischung. Der Erstarrungsprozess ist ein wichtiger Aspekt für die Feinfragmentierbarkeit einzelner Tropfen und für die Explosivität der ganzen Mischung. Geometrisch bedingte Asymmetrien können die Explosivität der Mischung und die resultierende Explosionsstärke durch eine räumliche Verformung und Verzerrung des Mischungsbereiches erheblich beeinflussen. Die Distanz von dem „Epizentrum“ der Druckeskalationen zu den Strukturen spielt eine grosse Rolle und ist bei der Bestimmung der während des Detonationsvorganges resultierenden Belastungen durch eine Dampfexplosion entscheidend.

Die im Rahmen der Dissertation erweiterten Programmcodes JEMI und IDEMO-3D stellen ein anwendbares Werkzeug zur Analyse der Mischungsvorgänge von Schmelze und Wasser sowie der Detonationsprozessen in 3D dar. Damit wurden asymmetrische Reaktorszenarien untersucht, für welche der Schmelzeeintrag, die Wasserhöhe und die Ausfliesskonfiguration variiert wurden. Der Einfluss von Asymmetrien auf die Bildung explosiver Konfigurationen wurde in Bezug auf die

Strahlfragmentierung, die Voidbildung und die seitliche Ausdehnung des Mischungsgebietes kritisch diskutiert. Gekoppelte Berechnungen zu Reaktorszenarien und Prädiktion von Strukturbelastungen bei Dampfexplosionen sind mit den hier entwickelten Programmcodes möglich.

Table of Contents

Nomenclature

Latin symbols

A	-	coefficient (Epstein-Hauser correlation)
a	m^2/s	thermal diffusivity $a = \lambda/(\rho c_p)$
a	m/s^2	acceleration
B	-	coefficient (Epstein-Hauser correlation)
c_p	J/kgK	specific heat capacity
D,d	m	diameter
E	$Pa \cdot m$	Young modulus
F,f	-	factor
g	m/s^2	gravity acceleration
h	J/kg	specific enthalpy
h	$W/(m^2K)$	heat transfer coefficient
K	$kg/(m^3s)$	friction coefficient
L	m	characteristic length
M,m	kg	mass
$\dot{m}$	kg/s	mass flow
N	$Pa \cdot m^3$	stiffness
p	Pa	pressure
Q	J	Enthalpy
R	m	Radius
t	s	time
T	K	Temperature
u,v,w	m/s	velocity
V	m^3	volume

Greek symbols

α_i	-	phase volume fraction
α	-	void $\alpha = \alpha_g/(\alpha_g + \alpha_l)$
δ	m	crust thickness
Γ	$kg/(m^3s)$	volumetric evaporation and condensation rate

λ	m	wave length (shear flow instability)
λ	$W/(mK)$	thermal conductivity
η	m	wave amplitude (Kelvin-Helmholtz instability)
ν	m^2/s	kinematic viscosity
ρ	kg/m^3	density
σ	N/m^2	surface tension
σ	N/m^2	Stefan-Boltzmann constant $\sigma = 5.67 \cdot 10^{-8}\, W/(m^2 K^4)$

Subscripts

λ	wave length
amb	ambient
b	basic amplitude
corr	correction, corrected value
bound	boundary
bulk	bulk
crust	crust/ solid layer
D, d	melt droplet
E, e	entrainment
f, fl	fluid
fb	film boiling
film	vapor film
fr	fragmentation
fric	friction
fus	heat of fusion
g	gas
int	interface, interfacial
j, jet	melt jet
l, liq	liquid
lt	transition value (liquid-transition)
lv	transition value (liquid-vapor)
liqui	liquidus
m	melt
new	new time step
old	old, previous time step

p, pac	melt particle
pool	melt pool
rad	heat radiation
rel	relative
s	stripping off, solid
sat	saturation
sep	separation
soli	solidus
strip	stripping
surf	surface
t	transition regime
tot	total
v, vap	vapour
vt	transition value (vapour-transition)

Superscripts

evap	evaporation
loss	loss, heat loss in CFOR
D	melt droplet

Dimensionless numbers

Bo	-	Bond number, $Bo = \rho a L^2 / (\sigma)$
Nu	-	Nusselt number $Nu = hL/\lambda$
Pr	-	Prandl number $\mathrm{Pr} = c_p \mu / \lambda$
Re	-	Reynolds number $\mathrm{Re} = wL/\nu$
We	-	Weber number $We = \rho v^2 d / \sigma$

Computer codes and modules

CFOR	Model to crust formation and solidification of a spherical particle, implemented in JEMI
ESPROSE.m	2D program code to explosion phase, UCSB, USA,
FRADEMO	Fragmentation model of melt drops in fluids based on hydrodynamic fine-fragmentation (IKE)
CULDESAC	Propagation model, AEA Technology, UK
HTMOD	Solidification model for single drops implemented in MC3D, JSI, Slovenia
IDEMO	2D program code for explosion phase, IKE, Germany
IDEMO-3D	3D program code for explosion phase, IKE, Germany
IFCI	Integrated code for premixing and explosion phases, SNL, USA
IKEJET	1D module to breakup of melt jets in water, IKE, Germany
IKEJET/IKEMIX	2D program code for premixing phase, IKE, Germany
IKEMIX	2D module for mixing of fragmented melt in water, IKE, Germany
JASMINE	2D steam explosion simulation code, JAEA, Japan
MC3D	3D program code for premixing and explosion phase, IRSN, France
PM-ALPHA	3D program code for premixing phase, UCSB, USA
TEXAS	1D program code for explosion phase, UCSB, USA
THIRMAL	Premixing program code, ANL, USA
VESUVIUS	Steam explosion simulation code, NUPEC, Japan

Abbreviations

General

1D	One-dimensional
2D	Two-dimensional
3D	Three-dimensional
AM	Accident Management
BWR	Boiling Water Reactor
ECCS	Emergency Core Cooling Systems
FCI	Fuel-Coolant Interactions
INES	International Nuclear and Radiological Event Scale
KH	Kelvin-Helmholtz (instability)
MBC	Melt-Bottom-Contact
PWR	Pressurized Water Reactor
RPV	Reactor Pressure Vessel
RT	Rayleigh-Taylor (instability)
SARNET	Severe Accident Research Network, OECD
SE	Steam Explosions
SERENA	Steam Explosion Resolution for Nuclear Applications, OECD

Institutions

BMWi	Bundesministerium für Wirtschaft und Technologie, Germany
CEA	Commissariat à l'Energy Atomique, France
EdF	Electricitè de France, France
FZK	Forschungszentrum Karlsruhe, Germany
GRS	Gesellschaft für Anlagen- und Reaktorsicherheit, Germany
IAEA	International Atomic Energy Agency
IAPWS	International Association for the Properties of Water and Steam
IKE	Institut für Kernenrgetik und Energiesysteme, University of Stuttgart, Germany
IRSN	Institut de Radioprotection et de Sûrete Nuclèaire, France
JSI	Jozef Stefan Institute, Lubljana, Slovenia
KAERI	Korea Atomic Energy Research Institute, Daejeon, South Korea
KTG	Kerntechnische Gesellschaft, e.G., German Nuclear Society
OECD	Organisation for Economic Co-operation and Development
UCSB	University of California, Santa Barbara, USA

1 Introduction

1.1 Background

Today, a significant part of electrical energy worldwide is produced by controlled nuclear fission in nuclear reactors. They contribute to both the national and world safeguarded power supply without the emission of greenhouse gases, which are believed to be a cause for global warming. Discussions on the prolongation of the use of nuclear energy are controversial, mainly due to the perceived potential risk posed by nuclear power plants to the public and environment. In order to assess risks accurately and to prevent accidents with an adverse outcome, a rigorous assessment of nuclear reactor safety is of crucial importance for the construction and operation of nuclear power plants.

The operation of nuclear power plants requires mastering extreme operational conditions – very intense heat generation with considerable heat flux under high pressure and possible power excursions as well as extreme heat transport mechanisms with very high flow rates of the coolant through the system. Even after emergency or regular shutdown of the nuclear reactor, heat continues to be produced by the radioactive decay of the fission products. During operation, the decay heat contributes about 7% of the total heat power and decreases logarithmically after the shutdown to ~1% (~38 MW) after one hour. According to a prediction in [1], the sum of the total decay heat produced in one hour after shutdown in a BWR (e.g. Gundremmingen Block B) with a total operating power of 3840 MWth is about 319 GJ. After one day – approximately 3580 GJ. This large amount of decay heat causes in a short time the reaching the fuel cladding temperature of 1477 K in central core regions, when the exothermal reaction of the cladding material (i.e. zirconium-alloy-composition) and water/vapor sets on leading to core damage or even the core melting. In order to avoid any damage to the reactor core being caused by decay heat, the cooling of the reactor core must be always assured.

The Emergency Core Cooling System (ECCS) ensures cooling of the reactor core in events with breaks or leaks in the reactor piping as well as the loss of the main cooling and thus prevents a core damage. Once the emergency cooling systems fail, the reactor core will melt due to decay heat. As the last nuclear accident on March 11th 2011 in Japan at Fukushima-Daiichi nuclear power plant showed, the failure of the ECCS can be resulted from nature cataclysms as strong earthquakes and external floods due to tsunami causing the loss of the offsite power, the emergency power supply and the main heat sink. Reactor core degradation on a grand scale can be a possible consequence, once no cooling in a later phase takes place. After the reactor core melts due to decay heat, large quantities of molten core material would relocate from the reactor core to the lower plenum of the reactor pressure vessel

(RPV) where it would interact with water, lower plenum and RPV structures. Possible consequence may be the structural failure of the lower bulkhead of the RPV due to thermal loads or due to high energetic fuel-coolant interactions (FCI) in the lower plenum. Amongst such high energetic interactions, the so-called Steam Explosion (SE) is initiated by energy transfer from the hot molten fuel, which is either metallic or oxidic, to the cold liquid coolant. In a LWR, a rapid boiling of the coolant ensues and the pressure rises locally. Steam explosions can also occur after failure of the RPV. In such a case, the molten core debris would pour from the failed RPV into the reactor cavity pre-filled with water. The dynamic loads on the cavity wall due to a steam explosion could potentially cause the failure of the cavity structures and the primary piping system producing severe mechanical loads that could threaten containment integrity.

In dealing with reactor safety and its potential consequences, all incidents occurring in civil nuclear installations are today classified in incidents and accidents depending on their probability, severity and public exposure. The International Nuclear and Radiological Event Scale (INES) is an internationally acknowledged public classification of safety-relevant information used for rapid and effective communication by reactor operators and national regulators [2]. According to the INES classification, steam explosions come under severe accidents, with a very low probability of occurrence (less than once per million reactor-years) and are considered beyond-design-basis events. The deterministic analysis of such events is usually required by regulatory guidelines or plant-specific licensing requirements to demonstrate the capability of the plant to mitigate the consequences of such events; [3,4]. Accidents are generally defined as events postulated to potentially inflict damage on one or more of the containment barriers (i.e. the fuel rod cladding, the reactor pressure vessel, the primary and secondary containment). These events are not expected to occur during the plant lifetime. Rather, they are used to establish the design basis for nuclear facilities with regards to basic protection principles, such as the control of reactivity, the ability to cool the core, to contain all radioactive substances and to mitigate the consequences of any exposure to radioactivity.

The first occurrence of a steam explosion can be dated to December 12th 1952, [5]. It occurred in the Canadian NRX test reactor due to the failure of the shutdown rod system and ensuing power excursion. The reactor suffered a partial meltdown; some of the fuel cladding burst and radioactive materials was released into the NRX building. Other accidents, such as the BORAX boiling water reactor, the SL1 reactor and the dedicated power excursion reactor test IDAHO (SPERT) also experienced disruptions by high pressure loads up to 70 MPa. All of these steam explosions were a consequence of reactivity excursions. A full account of past FCI accidents is summed up in [6,7].

The only commercial nuclear reactor ever to be damaged by a steam explosion was Block 4 of the Chernobyl plant, on April 26th 1986, [8]. In this reactor as well, it was an uncontrolled power excursion which led to the dispersion of fuel into the

surrounding water. This was followed by one or two steam explosions leading to the destruction of the reactor vessel and reactor building as well as to the release of large amounts of fission products into the atmosphere and contamination over a large area. The Chernobyl accident is the only one to be classified as a Major Accident, at INES 7 (it is the most severe in the INES classification) highlighting the potency of a steam explosion and its off-site impact [2]. The Fukushima-Daiichi accident being also classified at INES 7 is believed to be caused by hydrogen explosion leading to its large offsite impact.

Steam explosions have also been reported in other industrial non-nuclear facilities such as foundries (steel and aluminum), paper factories and liquid natural gas (LNG) transport. On a geological scale, various conditions can lead to explosive FCI interactions such as in volcanoes, between magma and water, so-called phreatic eruptions, reported on in [9].

1.2 State of the art

Steam explosions are analyzed in the context of reactor safety research, as a possible cause of large-scale and rapid deterioration of the RPV or the containment due to destructive pressure loads. Such loads are the result of strong interactions of the molten core material from the destroyed reactor core with water inside the RPV or the reactor cavity inside the primary containment. Excluding the damage potential from powerful steam explosions would ensure increased safety and could improve the basis for accident management with regards to the water supply used in cooling. In order to investigate the nature and the mechanisms of steam explosions, several research projects have been initiated on a national and international level, both from a theoretical standpoint and on an experimental basis.

A large number of small and large scale experiments were performed in order to identify the initial conditions responsible for triggering and propagating explosive interactions between water and molten core materials and to assess the magnitude of pressure loads in a hypothetic steam explosion in a Light Water Reactor.

The first experimental investigations were single drop experiments with Wood's metal performed at IKE [10,11], or iron oxide and cobalt [12-15] performed at Sandia National Laboratories. The aim was to investigate the connection between the initial conditions (i.e. melt properties, coolant temperature, ambient pressure, relative velocity and solidification of melt drops) and the ability of drops to fragment finely, thus leading to a steam explosion. Fröhlich proposed in [16], that a steam explosion can occur even with small temperature differences between the melting temperature of the molten metal and the boiling temperature of the coolant. The single drop experiments generally provide a solid base for the analysis of single drop explosive potential and its limiting effects. However, the results of these experiments cannot be

simply extrapolated to real reactor conditions with large melt and water masses, since the mixing of fragment melt and water becomes relevant.

Considering the limitations of the single drop experiments, a series of large scale experiments have been performed. In these experiments, both the conversion ratio of the fuel thermal energy into mechanical work and the hydrodynamic limitation of the mixing of fragmented melt and water have been investigated at a large scale (5-200 kg melt mass). The iron/aluminum oxide, Fe-Al_2O_3 was chosen to replicate corium at Sandia National Laboratories [17,18].

A variety of corium compositions was taken at JRC-Ispra FARO [19,20]. Al_2O_3 and corium were used in the KROTOS [21] and PREMIX experiments [22-26] at FZK where they are mixed with water both with and without triggering. The aim was to create a solid base for investigating the following aspects: melt jet break-up, distribution and quenching of melt fragments in mixture, void building and the role of initial conditions, such as initial water sub-cooling, ambient pressure and melt temperature. Particular attention was paid to the interdependencies between these parameters in order to determine their influence.

In order to extrapolate the experimental findings, several multiphase models and thermal-hydraulic codes considering all three phases (water, steam and melt) have been developed at different institutions within the context of different international cooperation programs, e.g. IFCI [27,28], TEXAS [29,30], PM-ALPHA [31], ESPROSE.m [32,33], MC3D [34,35], JASMINE [36], VESUVIUS [37], THIRMAL [38,39], IKEJET/KEMIX [40], IDEMO [41,42]. The aim of these programs was to analyze the complex FCI phenomena especially the break-up of melt jets, triggering from mixing of melt and coolant, fine fragmentation and explosion strength.

The SERENA project (Steam Explosion Resolution for Nuclear Application) in reactor safety research, has been initiated on an international level the goal of which was to enhance the applicability of existing models and codes to existing reactors, [43]. Several FCI codes have been used within the scope of SERENA and SERENA-2 projects, integrating results and analyses. The work was oriented towards benchmarking and test-fitting analysis for the purpose of safety analysis and in order to identify key effects that may limit the explosion strength.

1.3 Objectives of the present work

The main thrust of the present work is to extend existing two-dimensional models IKEJET/IKEMIX and IDEMO which include the premixing and explosion phases of vapor explosion in 2D to 3D, in order to be able to simulate possible non-symmetric conditions in reactor accident scenarios which are likely to have a stronger damaging character. For instance, a lateral melt outflow into water in direct proximity to the RPV and reactor cavity walls or a melt outflow at specific point locations could be considered as typical non-symmetric configurations in reactor applications.

Until now, asymmetric reactor configurations could generally be investigated in two ways: using two-dimensional approximations either with an equal distribution (smearing) in tangential direction of the mixture or by varying the problem size (see Chapter 3). The first approach is questionable from the outset due to the artificial nature of diluting or smearing the mixture in tangential direction, which artificially decreases the melt fraction and the void. In the latter case, a sequence of calculations had to be performed in plane or axis-symmetric coordinates, varying the radial extension of the calculation domain, by which the influence of the non-symmetric geometrical restriction caused by the RPV wall or cavity structures on the progress of the mixture was investigated. Hereby, the extension of the melt dispersion and formation of void as well as its progression, accompanied by dilution or aggregation, is of a particular relevance. It influences the degree to which the mixture may explode during the premixing phase. In the explosion phase, the preceding degree of pre-mixing determines the explosion strength and the pressure loads on the adjacent structures. The distance from the epicenter of the pressure rise to the wall is of crucial importance to the reactor safety due to an attenuation effect from the body of water which has a free surface.

Considering all these aspects, 2D approximations suffer certain limitations in giving an adequate assessment of the mixture build-up and potential pressure loads due to the absence of the third dimension. Thus, the full extension of the mixture, melt fragments and void formation, in tangential direction during the premixing phase cannot be properly estimated, as well as the pressure relief in lateral regions and the reflection of the propagating shock wave in the explosion stage.

The extended three-dimensional models seek to correct these faults and result in greater accuracy in predicting the mixture behavior. The comparison of the full 3D calculations with the 2D approximations for a non-symmetric case is performed in order to weigh up the shortcomings of the 2D approximations with regards to resulting pressure loads at the adjacent structures.

Also, the present work considers improvements of the extended models in predicting the jet break-up under film boiling conditions in deep water pools (e.g. deep reactor cavity filled with water), the Lagrangian description of melt drops as distinct particles resulting from the jet fragmentation, the solidification of melt drops during premixing, the heat transfer in high sub-cooling conditions and the influence of crust formation on fine fragmentation during the explosion stage, for greater realism and to give a reliable prediction of pressure loads on surrounding structures.

Special attention is given to verification of the extended premixing model performed in the FARO experiments pertaining to both the build-up of the mixture and the solidification of melt drops settling at the bottom of the vessel, [44-46].

After verification, calculations are to be performed for realistic reactor scenarios. Here the focus lies primarily on investigating the most challenging case, i.e. the highest pressure loads on the surrounding structures potentially leading to their

failure. In this respect, different parameters such as the melt flow rate, the water level, the outflow configuration (single or multiple melt jets) and the triggering time of an explosion are to be considered under realistic conditions during severe accidents in LWRs.

2 Steam explosion phenomena in reactor applications

In general, steam explosions bear resemblance to conventional explosions. An explosion implies the rapid conversion of energy from one form to another form. Before each explosion is initiated, the energy must be stored in a meta-stable state, i.e. in a form without significant dissipation of available energy. The explosion, i.e. the rapid conversion of the available energy, can be activated by considerably smaller amount of activation energy, called a "trigger". The available energy is then rapidly converted into another form that can perform work in the surroundings, e.g. thermal energy is converted into kinetic energy. A steam explosion in the LWR's during a core melting constitutes a process by which a hot liquid (fuel) transfers its internal energy to a colder more volatile liquid (coolant). The coolant then vaporizes at high pressures and expands, thus performing work on the surrounding structures endangering its integrity.

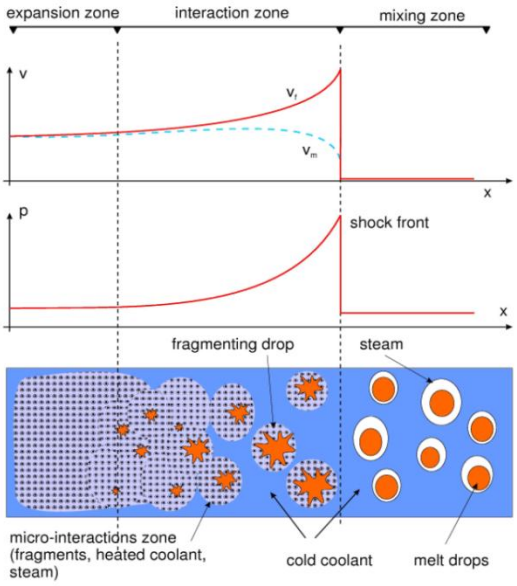

Fig. 2-1: Schematic sketch of a thermal detonation (Buck et al., 1997 [42])

A process for vapor explosion is proposed in Fig. 2-1. It is based on the "thermal detonation concept" of Board and Hall [47]. According to this concept, several sequential sub-processes can be distinguished, as discussed in [48-50]. At first, the high temperature molten material is coarsely mixed in water as small drops surrounded by vapor film. In the second step, the vapor film collapses due to disturbances of internal or external character, so-called "triggering". Thirdly, the hot liquid melt directly contacts the water without solidification. This process is followed by further fine fragmentation and atomization of the melt drop, thereby increasing the interaction surface area and the heat exchange from melt to coolant. Finally, rapid heat transfer and vapor generation cause local pressure rises and pressure pulses.

2.1 Coarse fuel-coolant mixing

The fuel-coolant mixing process can be understood as the formation of a coarsely mixed region with a quasi-stable initial configuration, as described in Board and Hall [47]. In this phase, contact of a hot liquid (corium) with a cold volatile liquid (water) results in a stable vapor film around the molten masses breaking up, allowing large quantities of melt and water to intermix.

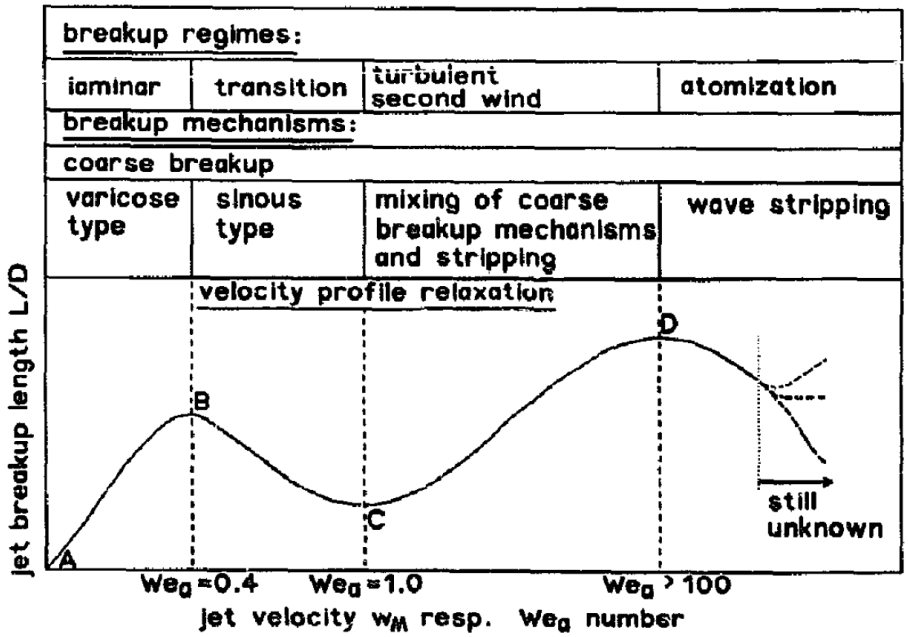

Fig. 2-2: **Sketch of jet breakup length curve with related breakup regimes and mechanisms (Bürger et al. [51])**

The initial fuel-coolant mixing phase is characterized by the sudden impact of the molten material (fuel) in water (coolant) and their mixing. In general, the fuel comes into contact with the coolant in the form of jets or, less commonly, as pre-fragmented drops driven by gravity. In the case of melt pouring in jet form, the jet fragmentation behavior is governed by various mechanisms, resulting from (liquid-liquid) contact and relative movement between the melt and the coolant.

Fragmentation of jets into drops has been discussed by many authors. Numerous experimental and theoretical studies have been carried out to investigate the key mechanisms of jet break-up, [51-55]. Ginsberg [53] identified the different break-up regimes range in relation to the melt jet thickness and the relative velocity between the jet and the coolant: from the varicose axis-symmetric break-up regime at low velocities, over sinuous break-ups to the atomization regime where wave stripping occurs at high velocities, see Fig. 2-2. Fragmentation of narrow jets is driven by the capillary instability and determined by surface effects at low relative velocities, the so called Plateau-Rayleigh or Rayleigh instability [56]. It pertains to the different fragmentation regimes of heavy liquids in a liquid or gas whose relative density is negligible in comparison, for instance water projected in air. In such cases, surface tension is the main cause for instabilities leading to jet break-up.

The turbulent and atomization regimes are characterized by high velocities and intense spray production directly at the onset of jet-coolant interaction, i.e. the jet ingress in water. Fragmentation of larger jets, which are relevant for reactor applications, is governed by Rayleigh-Taylor (RT) and Kelvin-Helmholtz (KH) instabilities. The jet break-up due to Rayleigh-Taylor instabilities can be briefly described as a deceleration of the melt jet in the surrounding liquid. In this case, jet

penetration is resisted by the stagnation pressure arising from the ambient fluid constraining lateral spreading of the melt. The RT instability appears mostly at the jet front implying two interacting fluids with similar densities. Theofanous et al. [57] considered RT instabilities as the operating mechanism, governing jet break-up during premixing. A parametric approach based on RT instabilities is used in the premixing code PM-ALPHA.L.3D, see [57].

In contrast to RT instabilities, the KH instabilities usually occur on the body of the jet, away from the jet front, and are driven by a shear flow and a stripping process due to the strong relative flows along the jet surface. Such strong velocity profiles can be ascribed to an upward steam flow along the jet. Along this interface, corium melt interacts with water at extremely high temperatures in the range of 3000 K. This leads to the formation of thick vapor film around the jet flowing upwards at high velocities along the jet surface driven by the hydrostatic pressure.

Analytical investigations [51,58] and experimental studies [52,54,55] about jet break-up in water pools showed that the fragmentation of jets on a large scale (i.e. large melt masses) is mainly governed by KH instabilities. Dinh et al. [58] additionally concluded that void formation in the coolant pool (i.e. coolant relative density) strongly affects the jet breakup. Also, the initial jet velocity at the pool surface might play an important role both in jet dynamics and fragment distribution in the mixture.

The jet break-up model related to the lateral stripping in thick vapor film conditions, based on KH instability, has been implemented in IKEJET, [40]. The present jet break-up model in IKEJET is also used in JEMI with a further extension for very long jets resulting from large masses pouring out, as discussed in detail in Chapter 4.4.

The melt drops result from jet fragmentation and participate in thermal interactions with the surrounding coolant by film boiling and heat radiation, heating up and vaporizing the water whilst cooling down and solidifying.

2.2 Triggering

As the initial phase of the steam explosion, triggering of a steam explosion can also be considered to be similar to ignition in a combustion process. This refers to the spontaneous or deliberate application of a pressure pulse, a flow perturbation or a local coolant entrainment. It may lead to interfacial instabilities, the subsequent collapse of the vapor film surrounding the melt fragments and direct contact between hot melt and water. This causes a strong increase of heat transfer between the molten material and the coolant and high steam production.

Nelson et al. [59,60] have investigated the triggering of steam explosions in experimental studies at small and immediate scales. Accordingly, various factors affect the triggering of the steam explosion: the initial water sub-cooling, the ambient pressure, the amount of- and spatial distribution of liquid fragmented molten mass, which has not yet solidified, and the steam content in the mixture. For example, an increasing the water sub-cooling decreases the thickness of the vapor film, making a

vapor film collapse, as well as triggering of the mixture, likelier. With increasing ambient pressure, the vapor film density increases and the film becomes more stable against pressure pulses.

In an experimental study with both a small amount of melt and single drops, performed by Abe et al. [61], trigger mechanisms of the vapor explosion have been investigated using tin, lead, zinc and aluminum for the melt and water as coolant. Abe et al. [61] identified that the vapor explosion cannot be triggered if solidification of the melt drop is achieved.

2.3 Explosion propagation

Small and intermediate scale experiments using corium in the composition of the melt have not led to large detonations [21,44]. On the contrary, equivalent melts replicating molten fuel, using for instance alumina [21], oxides of iron and cobalt [59,60] have mostly resulted in violent explosions with high pressure peaks up to 70 MPa. This requires a deeper analysis of possible limiting effects during the explosion phase.

Central enhancing and limiting factors affecting steam explosion process results from the premixing phase. Restricted melt mass in the mixture (melt fragments from the jet break-up) limits the ability of the pressure to escalate rapidly. This can occur both locally in sparse mixture regions and globally as a result of incomplete jet break-up. On the other hand, a dense mixture generates a high void, which counteracts pressure escalations due to its compressibility decreasing the explosion strength. The melt drop size resulting from the jet break-up during premixing plays an important role in steam explosions. Here, smaller drops lead to a quicker fine fragmentation during the shock wave propagation allowing the pressure to rise steeper. However, smaller drops generate more steam during premixing, which counteracts the pressure increase due to its compressibility. Moreover, the smaller drops solidify quicker. The solid crust forming on the drop’s surface constrains or even inhibits the fine fragmentation required for ultra-fast heat exchange and the generation of pressure pulses. On the contrary, larger drops fragment slower. Thus, the contribution to pressure increases from larger drops is significantly smaller. But, the larger drops remain significantly longer liquid, potentially leading to a steam explosion. Solidification during premixing is a possible explanation for the difference in explosion strength between the experiments with corium and alumina melts [62,63]. The solidification of melt drops is discussed in detail in Chapter 4.7.

Other effects playing a role in the explosion propagation are generally of a geometrical nature. The geometrical effects concern the reduction and enhancement effects of pressure waves by 2D expansion or lateral geometrical restrictions and reflections on free surfaces (explosion venting). Investigations and results related to geometrical limitations are presented in Chapter 7.

2.4 Explosion expansion

A steam explosion performs work whilst expanding. The expansion of the resulting high-pressure mixture behind the propagation front, see Fig. 2-1, determines the damage potential of a steam explosion on the surrounding structures. The kinetic energy of this high-pressure mixture may be transmitted to the materials around the interaction zone, thus generating missiles with more or less mass, which are likely to threaten the integrity of the surroundings, both in-vessel and ex-vessel.

3 Need of three-dimensional modeling for reactor applications

Steam explosions are postulated to occur during severe accidents in a Light-Water Nuclear Reactor with meltdown of the reactor core due to failure of the normal and emergency core cooling. The reactor core dries out and melts building a melt pool in the core region. A solid crust developed from cooling of the melt materials by vapor flow encloses the melt pool. Due to high decay heat, a failure of the melt pool arising from further fusing of surrounding structures is expected. The consequence of breaking the crust enclosing the pool is a melt outflow from a failed melt pool into the lower plenum of the RPV partially filled with water. During interactions of the molten core and water, steam explosions can occur inside the RPV (in-vessel steam explosion) yielding high pressure loads on surrounding structures. High loads can challenge the RPV integrity leading to a failure of the RPV and to a release of highly radioactive core materials into the primary containment. Possible failure of the RPV due to thermal (melting through the RPV wall) or dynamic loads (e.g. in-vessel fuel-coolant interactions) results in a release of molten core materials from the RPV into the primary containment (reactor cavity or drywell) expected to be filled with water. Steam explosions can then occur outside the RPV (ex-vessel steam explosion) during fuel-coolant-interactions in the reactor cavity. Pressure loads from an ex-vessel steam explosion could endanger structures of the primary containment, e.g. due to a quick and strong pressure rise in the primary containment or due to creation of missiles during a vapor expansion, challenging the containment integrity. The containment from the nuclear safety point of view is the final radiological barrier retaining the radiation exposure into the environment. The exclusion of critical loads of steam explosions warranting the integrity of the RPV and the primary containment would mean a re-evaluation of cooling with water and opening of additional options for accident management to mitigate severe accidents and resulting radiological consequences for the plant staff and the resident population. In-vessel and ex-vessel fuel coolant interactions are schematically shown in Fig. 3-1.

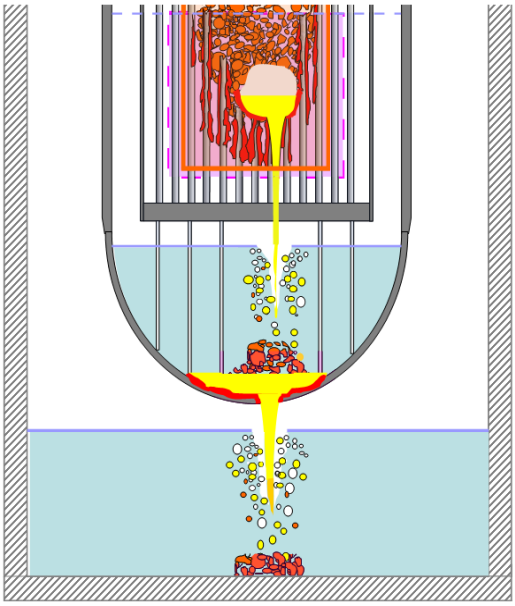

Fig. 3-1: Schematic illustration of the jet breakup and premixing of the melt drops in the water, in-vessel and ex-vessel, [77]

Models and program codes IKEJET/IKEMIX [40] and IDEMO [42] have been developed and validated at the Institute of Nuclear Technology IKE. The models

address the breakup of melt jets, mixing of fragmented melt and coolant, detonation, fine fragmentation and propagation of shock waves in the mixture of melt, steam and water. The program codes allow a better understanding of the steam explosion phenomena, the analysis and prediction of resulting loads at the surroundings. The assessment of that impact is of crucial importance for the reactor safety supporting its continuous improvement in the nuclear power plants worldwide. The programs simulate the premixing (by IKEJET/IKEMIX) and explosion (by IDEMO) stages of a steam explosion in a two-dimensional approach in plane and cylindrical geometry. The models address primarily the central physical effects which act limiting or enforcing for steam explosions:

- Fragmentation of melt during the contact with water. It describes the entry of fragmented melt into water. Both the fragmentation rate and resulted fragment size play an important role during the premixing and explosion.
- High void in the mixture during the premixing due to high melt temperature. It affects the heat exchange between melt and coolant.
- High void in the mixture during the explosion. Due to high compressibility, high steam content acts dampening for local pressure escalation strongly limiting the buildup of shock waves and fine fragmentation of melt.
- Reflexion of pressure waves at free surfaces and adjacent structures. Reflecting waves can have both effects: escalating and counteracting. This depends merely on mixture configuration and geometry determining the direction and intensity of reflexion.
- Velocity compensation between melt drops and coolant in a shock wave traveling through the mixture [64]. This occurs primarily in regions with high melt concentration limiting the fine fragmentation.

Further effects affecting the steam explosion (not considered by the 2D models) are to be mentioned here. The first is the solidification at the surface of melt drops during the premixing with coolant. The second is possible asymmetries in the mixture due to geometrical constraints and confinements. The solidification of melt drops always acts limiting for steam explosions, since a solid crust at the drop surface inhibits or even prevents the drop fine fragmentation during the explosion stage reducing the melt mass participating in the explosion process. Solidification occurs even with high melt temperatures due to the high solidus temperature and the low thermal conductivity of corium. Asymmetries during premixing are expected generally by non-symmetric configurations, e.g. during a sideways melt pouring into water or melt pouring with multiple jets.

Configurations with lateral pouring from the melt pool are supposed to be most likely, since the hottest region in the pool is assumed to be at the upper boundary due to natural heat convection. Scenarios with pool failing on the bottom were still thinkable due to a complex set of thermal loads. However, the development of large melt pools

with critical melt masses is questionable and strong loads can be excluded for explosion scenarios with bottom outflows. In general, a failure of a melt pool leading to melt relocation is expected due to lateral growth of the melt pool and fusing the sideways structures (e.g. core barrel or RPV wall) with its potential failure. Configurations with lateral melt outflows are physically limited by the outflow mass flow rate and velocity. Since the outflow location is expected at upper boundaries, the first local opening leads to quick lowering of the pool level reducing the hydrostatic head and decreasing the melt outflow velocity. Decrease of the outflow velocity restrains the growth of the opening where the melt flows out. Thus, openings cannot increase unlimited. Potentially, melt jets with limited diameter lower than 40 cm and small outflow velocity ~ 1 m/s are expected during melt pouring from a melt pool in the core region. In contrast, higher outflow velocities and thus larger mass flow rates are expected in ex-vessel scenarios due to a moderate overpressure inside the RPV. In ex-vessel scenarios, a lateral failure of the RPV due to thermal loads is rather thinkable than a bottom-break of the RPV. After relocation of molten core materials into the lower plenum of the RPV, a lateral break through the RPV wall is rather likely, since the hottest spot is located in the top region of the melt pool due to heat convection. In addition, a lateral “fish-mouth” breach of RPV due to thermal loads and a moderate overpressure can be also considered. This causes a sideways distributed melt outflow, so-called “multiple jets”, in form of a corona providing an initially better distribution of large melt masses with limited void. Non-symmetric initial pouring can lead to asymmetries in mixtures with local concentrations of melt causing strong local evaporation and void buildup. The latter supports the occurrence of pressure relief paths and extension paths of the mixture. The occurrence of such paths strongly depends upon geometrical constraints. The short-term de-voiding of the mixing region especially of regions with high melt concentrations in direct proximity to structures (e.g. RPV or cavity wall) is quite thinkable due to the difference in the density between vapor and melt during strong mixture fluctuations. High melt concentration in combination with reduced void can support high pressure loads during the explosion phase. Even diluted mixtures with well-distributed melt (low melt content) and limited void can yield strong pressure escalations over long distances during the explosion phase. Also, sparse regions interacting with dense regions can act sustaining or even enforcing to pressure escalations increasing their damage potential. Due to complex interrelation between the factors, it is impossible to analyze these in a separate manner using 2D description.

Summarizing all these factors, the extension and distribution of melt and void due to geometrical constraints is considered to be the central question posed by typical three-dimensional accident configurations, such as lateral or multiple melt pouring into water. The mixture extension (dilution) causes a decrease of the melt concentration and a reduction of the steam content in the mixing zone due to formally a “stretching” of the mixing region. High melt concentrations at adjacent structures expecting in non-symmetric configurations support pressure escalations by high

concentrations of thermal energy. On the other side, such concentrations also cause a very intense evaporation in those regions counteracting local pressure buildup. Void reduction as a result of mixture extension always means an increase of pressure loads as a consequence. Reduction of void in the mixing zone has a large impact on solidification of melt drops by intensifying the heat exchange between melt and coolant due to stable film boiling.

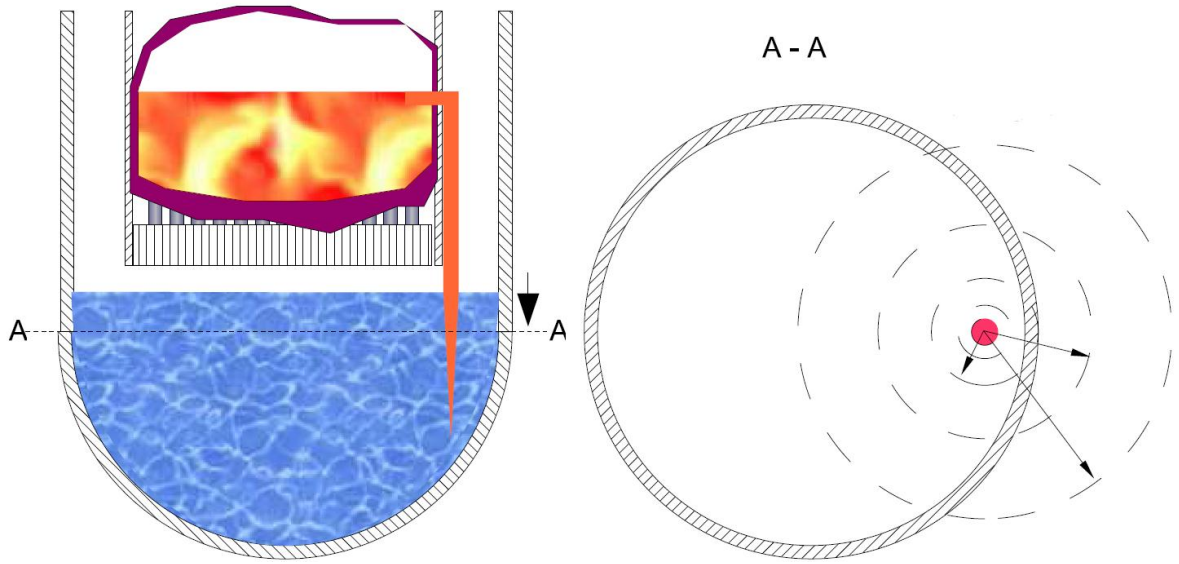

Fig. 3-2: **Non-symmetric melt jet in lower plenum of the RPV (left), variation of radial extension of the calculation domain using 2D approximations in cylindrical coordinate system**

Such complex and multifaceted interactions can be dealt using 2D models only in a limited consideration. Previously, investigations to non-symmetric configurations have been carried out using two-dimensional approximations. For example, for a non-symmetric melt jet close to the RPV wall, a set of calculations with various radial extensions in cylindrical geometry or plane cuts with various deepness have been used for investigating the premixing and the escalation stages of steam explosion. Fig. 3-2 shows an example for an analysis of an asymmetric melt jet pouring into the lower plenum of the RPV close to the RPV wall. The calculation domain radius has been varied in the cylindrical coordinate system. This case was investigated in [65]. This procedure shows weaknesses concerning the mixture extension. By the smallest radial extension, strong concentration of melt can be implied leading to high voiding of the mixing zone. By larger radial domain extensions, the effect of the RPV wall cannot be adequately considered. The largest melt mass in region with limited void was obtained by intermediate distances. The main question addressed the radial and azimuthal extension of the mixture from the regions close to the wall due to high

vaporization and pressure buildup. In the explosion phase, the proximity of structures affects the reflexion of pressure waves. By smaller radial extensions, pressure waves reflect from the wall and focus on the mixture which is locating in so-called “focal point”. This acts enforcing for pressure escalations and loads, which are strongly overestimated in this case. The larger extensions show sufficiently weaker effect of the wave reflexion due to increasing distance to the wall. The truth might be somewhere between the smallest and larger radial extensions. On the water-rich side, stronger dampening effects of water and weaker reflexions are expected for sparser well-extended mixtures. On wall sides, wave reflexions are expected to have a stronger influence. The investigations using the 2D approximations showed open issues concerning the real extension of the mixture in pronouncedly 3D configurations due to existing uncertainties. It was considered as questionable and far from reality.

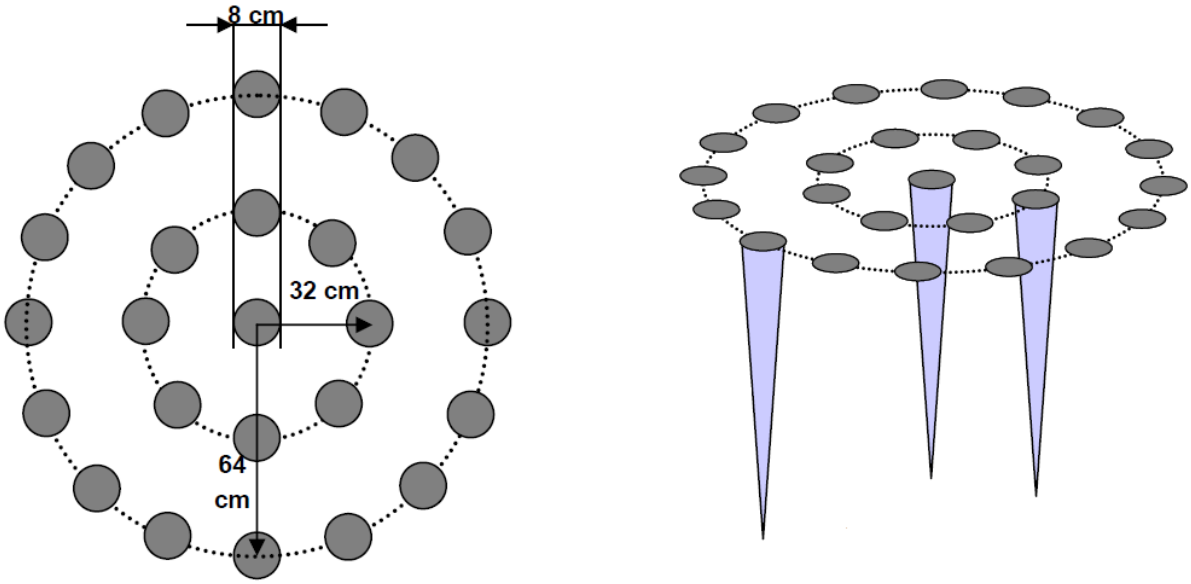

Fig. 3-3: **Multi-jet configuration with 25 jets using 2D approximations in cylindrical coordinate system, extracted from [66].**

In the frame of the OECD project SERENA [66], an in-vessel scenario with the configuration of 25 melt jets have been considered pouring into the lower plenum of the RPV, see Fig. 3-3. The aim of this investigation was to postulate a case with as large as possible melt mass mixing with water. The case postulates a scenario with the following initial conditions: core melting, melt pool building, melt fusing through the core support plate and pouring in form of multiple jets into the lower part of RPV. The melt jets are azimuthally distributed. All 25 melt jets are represented by 2D models as 3 jets in a radial cell with different melt fraction. This causes a dilution of melt content and an azimuthal smearing. The calculations have been performed using 2D premixing and explosion models in cylindrical geometry. The calculations

showed a very high void in the premixing stage and as a result weak pressure escalations during the detonation. The high void is caused by large mass of melt leading to strong steam production as well as rather by constraining for steam escape from the mixing zone and radial extension of the void cloud due to neighboring melt jets.

During the premixing, only the mixture extension in radial and axial direction can be considered by 2D models. The fluid exchange, i.e. the steam outflow and water inflow in the spaces between the melt jets are expected to play an important role during the premixing, since this reduces the void in the mixing zone. Without considering coolant fluctuations in azimuthal direction, the void in mixture is strongly overestimated and thus the mixture explosiveness is underestimated. The solidification of melt drops depends on the flow regimes and accordingly on steam content. Higher void in mixture then means weaker limiting effect of solidification and crust formation.

During the explosion phase, the propagation of the shock wave is also considered only in radial and axial directions. This leads to artificially concentrations of pressure escalations in the center of the calculation domain during the back-running of the shock wave. However, interactions between individual melt jets and mixture regions can act either dampening or enforcing. As a result of this complex interplay of particular effects, an adequate prediction of the explosion strength and resulting pressure loads for scenarios with multiple melt pouring cannot be done in a conservative manner.

Central effects on steam explosion strength are determined: void in mixing zone, melt solidification, lateral extension of void and melt fragment and development of explosion waves. The use of 2D approximations to typical 3D reactor scenarios is questionable due to complex interactions between the melt, coolant and geometry. Thus, it requires an extension of the existing models IKEJET/IKEMIX and IDEMO, in order to provide a tool for analyses of steam explosions in real reactor applications.

4 Three-dimensional premixing model JEMI

The program code JEMI (JEt fragmentation and preMIxing) is a three-dimensional version of IKEJET/IKEMIX developed at IKE for modeling the premixing phase of vapor explosions, presented by Pohlner et al. [40]. IKEJET/IKEMIX describes the fragmentation of molten jets under film boiling pouring into water, the mixing of melt fragments with coolant, heat exchange between melt fragments and surrounding coolant, cooling of the fragments, evaporation and re-condensation of the coolant, settling process of melt drops and the formation of debris beds. In the multi-fluid model of IKEJET/IKEMIX, three phases are considered: melt drops, liquid water and steam each having separate velocities and temperatures. The phases are modeled according to quasi-continuum Eulerian approach. The jet breakup formulation is based on the Kelvin-Helmholtz (KH) model of wave growth due to steam flow along the jet driven by hydrostatic head, see in detail [40,51]. The coherent jet length, the local rate of the fragmentation and mass release as well as the drop sizes are determined separately and represented as a line source of fragments in the separate module IKEJET.

In the scope of the present work the IKEJET/IKEMIX program code has been extended to the 3D version JEMI. The three-dimensional program code JEMI additionally offers a set of extensions performed in order to fit the applicability of the model for reactor scenarios. The jet breakup approach proposed by Bürger et al. [51] has been extended in consideration of the fragmentation of thick melt jets in deep water pools. This configuration is common during the pouring of large melt masses due to failure of the reactor pressure vessel and large breaks in it. Scenarios with large melt masses are expected to have a strong damaging character due to a high potential for the energy release and heat exchange between fuel and coolant. The melt fragments from the jet breakup are represented in JEMI by a Lagrangian formulation, i.e. as single particles or clusters of particles. This allows one to track of each particle avoiding the “smearing” of the melt data within the Eulerian field, i.e. averaging the melt enthalpy and velocities of all particles in the respective discrete cell. Further, the solidification and crust formation at the surface of melt drops, which come from a fragmenting jet and fall in water, is modeled using CFOR (Crust FORmation) model. The CFOR model is initially based on a surface temperature drop approach for a single spherical particle, proposed by Moriyama et al. [36]. This approach has been extended by the author in the present work considering two different temperature profiles in liquidus and solidus regions. The solidification enthalpy (heat of fusion) is described as solidification front and represented as a line source of heat between liquidus and solidus regions.

The objective of this chapter is to refer the basic modeling attributes (performed in IKEJET/IKEMIX [40], adopted and extended in JEMI) and to show the modeling extensions newly developed for JEMI.

4.1 Mathematical model

The JEMI two-fluid formulation uses a separate set of conservation equations of the coolant for each phase. The influence of one phase on another is considered by interaction terms (i.e. the interfacial drag force, phase change, interfacial heat transfer) appearing in the equations. The system of governing equations comprises one constraint equation, two continuity equations, 6 momentum equations, three energy equations for the fluid phases. Compared to IKEJET/IKEMIX, no continuity equation of the melt phase is considered in JEMI due to the Lagrangian approach used for the melt drops. The continuity of the melt phase is satisfied by considering the fragmentation (creation) and settling (destroying) processes in JEMI. From creation to destroying, no mass exchange is considered. Also, the momentum exchange between coolant and melt takes place in a separate formulation.

Conservation of mass

The conservation equations for the coolant phases are given for gas and liquid phases, respectively:

$$\frac{\partial}{\partial t}\alpha_g\rho_g + \nabla\left(\alpha_g\rho_g\vec{v}_g\right) = \Gamma^{evap} \tag{4-1}$$

$$\frac{\partial}{\partial t}\alpha_l\rho_l + \nabla\left(\alpha_l\rho_l\vec{v}_l\right) = -\Gamma^{evap} \tag{4-2}$$

where α is the volume fraction and ρ the density of the liquid and gaseous fluid phases. Phase change term Γ^{evap} means a mass transfer rate due to evaporation/condensation. Γ^{evap} can distinguished in two parts: Γ_{fb} as the evaporation due to hot melt droplets under film boiling (*fb*) and Γ_{bulk} as the evaporation/condensation at the water/steam interfaces (*bulk*) of steam bubbles and water droplets, thus

$$\Gamma^{evap} = \Gamma_{fb} + \Gamma_{bulk} \tag{4-3}$$

The volume fractions of fluid have to obey the volume constraint equation

$$\alpha_g + \alpha_l = \varepsilon \tag{4-4}$$

where ε stands for the porosity. The porosity is determined in due consideration of the melt and jet fractions in the respective volume.

Conservation of momentum

For the gas phase, the momentum conservation equation is given by

$$\frac{\partial}{\partial t}\left(\alpha_g\rho_g\vec{v}_g\right) = -\alpha_g\vec{\nabla}p + \alpha_g\rho_g\vec{g} - \vec{\nabla}\left(\alpha_g\rho_g\vec{v}_g\vec{v}_g\right) - K_{pg}(\vec{v}_g - \vec{v}_p) - K_{\lg}\left(\vec{v}_g - \vec{v}_l\right), \tag{4-5}$$

and for the liquid phase by

$$\frac{\partial}{\partial t}\left(\alpha_l \rho_l \vec{v}_l\right) = -\alpha_l \vec{\nabla} p + \alpha_l \rho_l \vec{g} - -\vec{\nabla}\left(\alpha_l \rho_l \vec{v}_l \vec{v}_l\right) - K_{pl}(\vec{v}_l - \vec{v}_p) - K_{\mathrm{lg}}\left(\vec{v}_l - \vec{v}_g\right) \tag{4-6}$$

where the term with K_{pg} and K_{pl} denotes friction between melt and respective coolant phase (for details see Section 4.2), with K_{lg} interfacial friction between steam and water. Convection of momentum and momentum transfer by phase change are presently not taken into account.

Conservation of energy

The energy conservation equation for the vapor given by

$$\alpha_v \rho_v \frac{\partial}{\partial t} e_v + \alpha_v \rho_v \left(\vec{v}_v \cdot \nabla\right) e_v = \left(\Gamma_{fb} + \Gamma_{rad}\right) \cdot \left(h_{v,film} - h_v\right) - Q_{v,\mathrm{int}} + Q_{v,gc} \tag{4-7}$$

and for liquid by:

$$\alpha_l \rho_l \frac{\partial}{\partial t} e_l + \alpha_l \rho_l \left(\vec{v}_l \cdot \nabla\right) e_l = Q_{fb,l} + Q_{rad,l} - Q_{l,\mathrm{int}} \tag{4-8}$$

where $Q_{fb,l}$ and $Q_{rad,l}$ are the partial heat flux terms for film boiling (*fb*) and heat radiation (*rad*) due to heat transfer between melt droplets and fluid phases. Vaporization (condensation) due to existence of superheated/subcooled coolant $Q_{v,\mathrm{int}}$ and $Q_{l,\mathrm{int}}$ produces vapour / water with saturation temperature T_{sat} and specific enthalpy h_v / h_l. The terms $Q_{v,\mathrm{int}}$ and $Q_{l,\mathrm{int}}$ are the volumetric heat flux from the respective coolant phase to the interface. Here, $Q_{v,\mathrm{int}}$ characterizes the heat transferred from the vapor film into the subcooled water, also containing the heat radiation contribution into the liquid water occurring under film boiling. The term $Q_{l,\mathrm{int}}$ concerns the heat transfer from the liquid water to the vapor film.

$Q_{v,gc}$ means the heat flux due to gas cooling (*gc*). Vapor from film boiling and radiation is produced with film temperature $T_{v,film}\left(> T_{sat}\right)$ and specific enthalpy $h_{v,film}$. Existence of subcooled water leads to partitioning of the total energy into film boiling and radiation due to heatup of water. Γ_{fb} describes the mass exchange contribution from film boiling and Γ_{rad} from heat radiation:

$$Q_{fb,tot} = \Gamma_{fb} \cdot \left(h_{v,film} - h_l\right) + Q_{fb,l} \rightarrow \Gamma_{fb} = \frac{Q_{fb,tot} - Q_{fb,l}}{\left(h_{v,film} - h_l\right)} \tag{4-9}$$

$$Q_{rad,tot} = \Gamma_{rad} \cdot \left(h_{v,film} - h_l\right) + Q_{rad,l} \rightarrow \Gamma_{rad} = \frac{Q_{rad,tot} - Q_{rad,l}}{\left(h_{v,film} - h_l\right)} \tag{4-10}$$

Energies connected with heatup of masses from phase transition do not appear in this representation since bulk enthalpies h_v, h_l are applied in the evaporation/condensation description:

$$\Gamma_{ev} = \quad \Gamma_{fb} + \Gamma_{rad} + \frac{Q_{v,\mathrm{int}} + Q_{l,\mathrm{int}}}{(h_v - h_l)} \tag{4-11}$$

The total volumetric heat flux at the melt side (from the melt drops presented in Lagrangian formulation to coolant) is expressed as:

$$\begin{cases} Q_{d,tot} = Q_{fb,tot} + Q_{rad,tot} \equiv V_{i,j,k} \cdot \sum_{n=1}^{np\_cell} A_n \cdot q_n = V_{i,j,k} \cdot \sum_{n=1}^{np\_cell} A_n \cdot \left(q_{fb,n} + q_{rad,n}\right) \\ Q_{d,tot} = Q_{d,ev,tot} + Q_{d,\mathrm{int},tot} \end{cases} \tag{4-12}$$

where $V_{i,j,k}$ is the volume of the corresponding cell and $\sum_{n=1}^{np\_cell} A_n \cdot q_n$ is an integral of the surface heat flux from each single melt particle q_n with the surface area A_n over all melt drops in this cell np_cell.

$Q_{d,\mathrm{int},tot}$ means the total heat transfer from melt to fluid without phase change. This heat transfer is directed to the interface of steam and water, directly via radiation and conduction over the steam film. $Q_{d,\mathrm{int},tot}$ also contains the heat input into the vapor film for heatup to $T_{v,film}$. The term $Q_{d,ev,tot}$ describes the contribution of the heat transfer from the melt phase to the phase change, here evaporation.

The heat exchange between melt and coolant at the melt side is further discussed in Section 4.6.

4.2 Constitutive laws

Exchange between melt and coolant

The melt drops are represented in JEMI as mass points using a Lagrangian approach. The drag between a single melt drop and the coolant phases is expressed in Section 4.5 in Eq. 4-56. Applying the Lagrangian description of melt into Eulerian field, the drag force of a single particle is multiplied with the number of particles in the respective discrete volume and divided by the volume of the corresponding cell:

$$f_{pl} = n\frac{\overrightarrow{F_p}}{V_p} = \frac{6\alpha_m}{\pi \overline{D}_p^3}\overrightarrow{F_p}, \tag{4-13}$$

and for the gaseous phase:

$$f_{pg} = n\frac{\overrightarrow{F_p}}{V_p} = \frac{6\alpha_m}{\pi \overline{D}_p^3}\overrightarrow{F_p}, \tag{4-14}$$

where n is the number of particles in the respective discrete volume and $\overline{D}_p$ is the mean drop diameter. The indices p, l and g mean melt particles, liquid and gas, respectively. The phase drag terms can be expressed by

$$K_{pl}(\vec{v}_l - \vec{v}_p) = n\frac{\overrightarrow{F_p}}{V_p} = \frac{6\alpha_m}{\pi \overline{D}_p^3}\overrightarrow{F_p} \tag{4-15}$$

and

$$K_{pg}(\vec{v}_g - \vec{v}_p) = n\frac{\overrightarrow{F_p}}{V_p} = \frac{6\alpha_m}{\pi \overline{D}_p^3}\overrightarrow{F_p}\,. \tag{4-16}$$

Exchange between the coolant phases

The formulation of the momentum exchange between the liquid and vapor is taken from IKEJET/IKEMIX [40]. Accordingly, the phase momentum exchange is determined by flow patterns. Vapor bubbles in the water-continuous regime result from film boiling, while water droplets are assumed in the steam-continuous regime. Here, $\alpha_{l,bound} = 0.3$ and $\alpha_{g,baound} = 0.7$ are considered as the boundaries for both regimes. Transition regime is assumed between the boundaries, for which an interpolation is applied according to respective parts of the limiting configurations.

Interfacial friction between liquid and vapor is formulated for three regions: flow of vapor bubbles in liquid ($\alpha_g < 0.3$), churn-turbulent flow ($0.3 \le \alpha_g \le 0.7$) called as transition flow and flow of liquid drops in vapor ($\alpha_g > 0.7$).

Bubbly flow $\alpha_g < 0.3$:

$$K_{\mathrm{lg}} = \frac{3}{4}\cdot\frac{\alpha_g}{D_g}\cdot\frac{\alpha_l}{\alpha_l + \alpha_g}C_D \cdot \rho_l \left|v_g - v_l\right| \tag{4-17}$$

with

$$D_g = \frac{We_{crit}\sigma}{\rho_l}\left|v_g - v_l\right|^2 \tag{4-18}$$

using the criterion for critical Weber number $We_{krit} = 8$ and with

$$C_D = \frac{2}{3}D_v\left(\frac{g\rho_l}{\sigma}\right)^{1/2}\left(\frac{1+17{,}67\cdot \mathrm{f}^{6/7}}{18{,}67\cdot \mathrm{f}}\right)^2, \quad \mathrm{f} = (1-\alpha_v)^{1.5} \qquad . \tag{4-19}$$

D_g is dropped from the friction term K_{lg}. The bubbles move in form of clusters with a steady velocity that does not depend on the bubble size.

Churn-turbulent flow $0.3 \le \alpha_g \le 0.7$:

According to

$$K_{\mathrm{lg}} = \frac{3}{4} \cdot \frac{\alpha_g}{D_g} \cdot \frac{\alpha_l}{\alpha_l + \alpha_g} C_D \cdot \rho_l \left| v_g - v_l \right| \tag{4-20}$$

with

$$D_g = 4 \left(\frac{\sigma}{g \rho_l} \right)^{1/2}, \tag{4-21}$$

and with

$$C_D = \frac{8}{3} (1 - \alpha_g)^2. \tag{4-22}$$

Drag coefficient C_D is resulted from the effective value 8/3 and from the approach for the averaged volumetric flux of the reference flow [67].

$$C_D = \frac{2}{3} D_g \left(\frac{g \rho_l}{\sigma} \right)^{1/2} \cdot \left(\frac{1 + 17{,}67\,\mathrm{f}^{6/7}}{18{,}67\,\mathrm{f}} \right)^2, \quad \mathrm{f} = (1 - \alpha_g)^{1{,}5} \tag{4-23}$$

From Eqs. (4-21) and (4-22) for churn-turbulent flow:

$$C_D = \frac{2}{3} D_g \left(\frac{g \rho_l}{\sigma} \right)^{1/2} \cdot (1 - \alpha_g)^2. \tag{4-24}$$

Further reduction of friction comes with the transition into the flow regime with $\alpha_g > 0.7$.

Flow of liquid drops in vapor $\alpha_g > 0.7$:

$$K_{\mathrm{lg}} = \frac{3}{4} \cdot \frac{\alpha_l}{D_l} \cdot \frac{\alpha_g}{\alpha_g + \alpha_l} C_D \cdot \rho_g \left| v_g - v_l \right| \tag{4-25}$$

with

$$D_l = \frac{We_{crit} \sigma}{\rho_g \left| v_g - v_l \right|^2}, \tag{4-26}$$

using for We_{crit} =12, and with the drag coefficient

$$C_D = \frac{2}{3} D_l \left(\frac{g \rho_l}{\sigma} \right)^{1/2} \cdot \left(\frac{1 + 17{,}67\,\mathrm{f}^{6/7}}{18{,}67\,\mathrm{f}} \right)^2, \quad \mathrm{f} = \alpha_g^3 \tag{4-27}$$

Here, the replacement of von ρ_l by ρ_g essential – steam instead of water as continuous phase.

The calculations performed in the frame of the international OECD project SERENA [45], particularly for FARO L-28, yielded generally a strong void buildup in the mixture, which was considered as too high in comparison to the experimental

indications, as discussed in [66]. Especially, the constant pressure rise over 5 s was impossible to achieve in the calculations due to too high void and weak steam production. The first indication was too high interfacial friction to remove the vapor from the mixing region. With a strong reduction factor of 10^{-3} on the interfacial friction force for more rapid steam removal and lower void in the mixture, it was able in the calculations to obtain the experimental pressure buildup. As in IKEJET/IKEMIX [40] so in JEMI, a reduction factor $f_{\text{int}\,fric} = 10^{-3}$ on friction coefficient is assumed.

$$K_{\text{lg}}^{*} = f_{\text{int}\,fric} \cdot K_{\text{lg}} \tag{4-28}$$

Reduction of interfacial friction has been further discussed in details by many authors; see [40,64,68,69].

4.3 Numerical solution method

For spatial discretization of the differential equations, a finite volume method is applied. For temporal discretization, implicit scheme based on backward differences are used. The non-linear coupled equation system from the discretized conservation equations is solved with a segregated procedure. The numerical scheme for the solution of the non-linear coupled system of differential equations is based on the SIMPLE algorithm, proposed by Caretto et al. [70], and adapted for solving the given problem. For spatial discretization, a staggered grid method is used. Variables like pressure, temperatures, densities are located at the cell centers of each cell (cell center of cell *(i,j,k)* marked by a dot in Fig. 4-1). Unlike this, the velocities are located with their normal components at the respective cell boundaries.

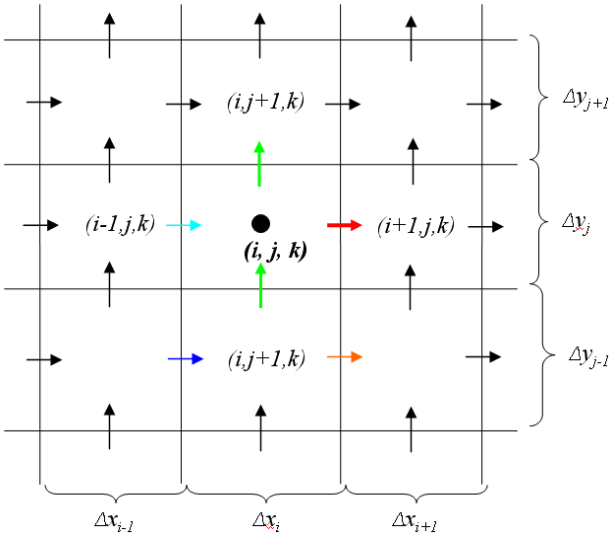

Fig. 4-1: Sketch and nomenclature of locations on a staggered grid.

In the present work, the equation system has been extended. The transient term has been added in the momentum equations. The aim was to manage complex numerical

feedback effects in 3D due to more complexity in the numerics. The data from the previous time step (i.e. densities, fractions and velocities) is used:

Gas:

$$0=\underbrace{-\frac{\partial}{\partial t}\left(\alpha_g\rho_g\vec{v}_g\right)}_{transient\_\_term}-\alpha_g\vec{\nabla}p+\alpha_g\rho_g\vec{g}-\vec{\nabla}\left(\alpha_g\rho_g\vec{v}_g\vec{v}_g\right)-K_{pg}(\vec{v}_g-\vec{v}_p)-K_{\lg}\left(\vec{v}_g-\vec{v}_l\right)+\begin{cases}\Gamma\vec{v}_e, & if\ \Gamma>0\\ \Gamma\vec{v}_g, & if\ \Gamma<0\end{cases} \tag{4-29}$$

Liquid:

$$0=\underbrace{-\frac{\partial}{\partial t}\left(\alpha_l\rho_l\vec{v}_l\right)}_{transient\_\_term}-\alpha_l\vec{\nabla}p+\alpha_l\rho_l\vec{g}-\vec{\nabla}\left(\alpha_l\rho_l\vec{v}_l\vec{v}_l\right)-K_{pl}(\vec{v}_l-\vec{v}_p)-K_{\lg}\left(\vec{v}_l-\vec{v}_g\right)+\begin{cases}\Gamma\vec{v}_e, & if\ \Gamma>0\\ \Gamma\vec{v}_g, & if\ \Gamma<0\end{cases} \tag{4-30}$$

This stabilizes the numerical approach decreasing the number of required iterations for solving the linearized conservation equations. Secondly, the considering the data of the previous time step supports the increase of the time step, which accelerates the calculation and reduces the computational costs.

When a Newton type of solver is used, the non-linear terms need to be linearized with respect to the primitive terms, namely the volume fraction α , pressure p and temperature T . For the purpose of linearization, the non-primitive (non-linear) variables, such as mass flux $\Phi_i=\rho_i A\vec{v}_i$, where i refers to the respective fluid phase is expressed with respect to the primitive terms. The momentum equations are linearized, in contrary to [70], with respect to phase volume fraction and pressure being solved within the continuity equations for each phase.

$$\delta\left(\Phi_i(\alpha,p)\right)=\frac{\partial\Phi_i}{\partial\alpha_i}\delta\alpha_i+\frac{\partial\Phi_i}{\partial p_i}\delta p_i \tag{4-31}$$

where i refers to the respective fluid phase.

The energy equations are linearized with respect to the phase temperature using the new phase velocities calculated before.

$$\delta\Phi_i(T)=\frac{\partial\Phi_i}{\partial T_i}\delta T_i \tag{4-32}$$

Due to the implicit time discretization, the mass and momentum conservation equations as well as the energy conservation equations have to be solved iteratively. This is done in JEMI as follows. First, the momentum equations for gas and liquid are solved for the gas and liquid velocities, using actual values of saturation and pressure.

$$\vec{u}_g^{\,new}=\frac{\alpha_g^2}{K_{pg}+K_{eg}+\frac{\alpha_g\rho_g}{\Delta t}\left(-\Gamma\quad if.\Gamma<0\right)}\left[-\left(\vec{\nabla}p+\rho_g\vec{g}\right)+\left|\frac{K_{pg}}{\alpha_g}\vec{v}_p\right|+\left|\frac{K_{eg}}{\alpha_g}.\frac{\vec{u}_e}{\alpha_e}\right|+\rho_g\frac{\vec{u}_g^{\,old}}{\alpha_g\Delta t}\left(+\frac{\Gamma}{\alpha_g}\frac{\vec{u}_e}{\alpha_e}\quad if.\ \Gamma>0\right)\right] \tag{4-33}$$

$$\vec{u}_l^{new} = \frac{\alpha_l^2}{K_{pl} + K_{eg} + \frac{\alpha_l \rho_l}{\Delta t}\left(-\Gamma \quad if.\ \Gamma < 0\right)} \left[-\left|\left(\vec{\nabla} p + \rho_l \vec{g}\right)\right| + \left|\frac{K_{pl}}{\alpha_l}\vec{v}_p\right| + \left|\frac{K_{eg}}{\alpha_l}.\frac{\vec{u}_g}{\alpha_g}\right| + \rho_l \frac{\vec{u}_l^{old}}{\alpha_l \Delta t}\left(+\frac{\Gamma}{\alpha_l}\frac{\vec{u}_g}{\alpha_g} \quad if.\ \Gamma > 0\right)\right] \tag{4-34}$$

Then, the calculated velocities are inserted in the mass conservation equations of gas and liquid. Applying the Newton type method the mass conservation equations are used to calculate corrections for the pressure and saturation so that the mass flow rates calculated with the corrected pressures and saturations satisfy the discrete mass conservation equations. This involves the linearization of the terms in the mass conservation equations with respect to saturation and pressure, including the dependence of the velocities on these. Successively, the energy equations are linearized with respect to temperature using the new velocities calculated above. The mass conservation equations are solved to determine the corrections for temperature. This iterative procedure has to be repeated until the calculated corrections for pressure, volume fractions and temperature satisfy the residuum conditions. Once the corrections are smaller than the defined residuum, the time step is completed. In case the maximum iteration steps are reached, the procedure is to be continued with a halved time step.

In order to avoid numerical oscillations of liquid and gas velocities in the solution of the linearized momentum conservation equations, a dynamic dampening factor ω_{dyn} on pressure and phase corrections is considered:

$$\omega_{dyn} = \min\left(1.0, \frac{\Delta p^*_{\max}}{\Delta p^*_{corr}}, \frac{\Delta \alpha^*_{\max}}{\Delta \alpha^*_{corr}}\right) \tag{4-35}$$

Δp^*_{corr} is resulted from the solution of the linearized conservation equations. $\Delta p^*_{\max}$ is maximally allowable pressure correction in each iteration for avoiding large corrections and making the converging process smoother. It is used additionally to the standard relaxation factor ω in the solution approach. The final pressure correction can be expressed as a product of the resulted pressure correction and of both relaxation factors, global and dynamical.

$$\begin{cases} \Delta p^* = \Delta p^*_{corr} \cdot \omega \cdot \omega_{dyn} \\ \Delta \alpha^* = \Delta \alpha^*_{corr} \cdot \omega \cdot \omega_{dyn} \end{cases} \tag{4-36}$$

This practical measurement allows one to further reduce the number of required iterations in the solution as well as to exclude the „unreal“ pressure and phase corrections, which cause oscillations and increase computational costs.

The coupling of the Eulerian fields of the fluids and the Lagrangian formulation for the melt droplets is done explicitly, see Chapter 4.5. New position and velocities are estimated for each representative particle considering the states of the continuous fields from previous time step. The new state of the melt drops is then used to determine the heat transfer from each particle to the fluid in the corresponding cell. The heat transfer determines the solidification rate, which gives the new surface

temperature of the melt drop as well as the new crust thickness required for explosion calculation in IDEMO-3D. The heat transfer and friction for the melt drops are described in an implicit way within the two-phase solution for the coolant phases.

4.4 Breakup of melt jets

The jet breakup behavior, i.e. the penetration in water and the fragmentation along the jet body, is described by a separate model for a representative jet. The present formulation of the jet breakup is based on the stripping model of Bürger et al. [51], which is implemented in the two-dimensional premixing model IKEJET/IKEMIX, proposed by Pohlner et al. [40]. It is considered that the lateral stripping due to relative flow along the jet is the major mechanism of the jet breakup, at least for thick jets, several cm of diameter and larger (see discussion in Chapter 2).

The intention of the present work was to review the existing representation of jet breakup in due consideration of known uncertainties of the breakup modeling and the applicability for 3D geometries. In the existing modeling, the fragmentation of the jet is described in 1D separate module. Here, only axial direction is considered. An upward steam flow along the melt jet is applied. The water-steam mixture close to the jet is considered to yield the driving forces determining this upward vapor flow. Thus, the effect of vapor bubbles reducing the total density of the surrounding fluid is taken into account in calculation of the hydrostatic head. The relative flow of steam along the jet produces instabilities at the surface of the jet column resulting in stripping of fragments. The existence of melt fragments in the vapor film and their influence on steam flowing upward along the jet was previously not taken into account.

In extending the premixing model to 3D, the present modeling of jet breakup has been re-analyzed with respect to possible extending from 1D to 3D. For this, the applicability for thick melt jets is considered. Those are thinkable in real reactor applications where pours of large melt masses into deep water pools are expected. Previously, an artificial friction was taken for limiting the relative flow velocities along the jet column. This limitation was required especially for long jets, since the relative flow velocities increase proportionally to the height of the hydrostatic column around the melt jet and overshoot the speed of sound for long jets. This unphysical issue is corrected in the present modeling.

Alternative approach VOF-SLIC, implemented in MC3D [35], has been taken into analysis as a possible replacement of the existing IKEJET model. The VOF-SLIC approach considers the jet as a separate fluid phase using the 3D Eulerian formulation. The main advantage of this approach is the direct coupling to the surrounding fluids as additional continuous phase. However, this is a disadvantage, too. The modeling uncertainties from fluid fluctuations as well as from evaporation and re-condensation can lead to an irregular and self-enforcing jet breakup. Here, high temporary and local fluid velocity and pressure peaks caused by uncertainties in

the modeling and numerics lead to unphysical behavior, e.g. locally intensified fragmentation, strong deformation and even complete disintegration of the jet.

Further, in order to properly describe the jet breakup using a separate phase formulation (e.g. the jet is modeled as a separate phase to water, vapor, and melt drops), a fine resolution of the space close to the jet is required. The fluctuation of the surrounding fluids and the deformation of the jet can then be correctly captured. In large 3D calculation domains, which are usual for real reactor geometries, a fine resolution of the region close the jet means an unproportional increase of computational costs and high requirements to the numerics making such calculations impossible. In contrary, the using of the 1D formulation allows a proper description of the jet breakup even by a coarse discretization due to considering the hydrostatic head for the relative flow and thus decoupling from the local velocities and pressures. This avoids artificial instabilities due to uncertainties in the numerics and modeling. Fluid velocities and pressures are used for determination of hydrostatic head and thus are considered implicitly in 1D formulation. Furthermore, no phase consideration as a 3D field and thus no additional conservation equations for the jet are to be solved in the separate 1D model. Only the porosity corrections in mass conservation should be done for each new time step due to jet movement. Concerning computational costs and memory demand, this is the biggest advantage compared to VOF-SLIC. The further plus to be mentioned is a simple implementation and the extensibility of the model, e.g. taking local fluid velocities and phase volume fractions directly to calculate relative flow velocities for lateral stripping. Therefore, the simplified one-dimensional model for the jet breakup is taken for further use in JEMI.

In the present work, the basic approach of Kelvin-Helmholtz wave growth and sheet stripping, described in [40], has been reviewed. The Kelvin-Helmholtz instabilities have been assumed to be the governing mechanism determining the fine jet breakup. The coarse breakup of thinner jets observed in KROTOS experiments in KS-series is considered as a non-typical case for reactor conditions, although it might occur at the leading edge during the initial stage of the jet penetration in water. The coarse breakup can be excluded as relevant mechanism for jet fragmentation. The coarse breakup at the jet leading edge is caused by Rayleigh-Taylor instabilities or deformation due to vortex formation. Experimentally, no strong deceleration, especially not with thick corium jets, could be detected. Deformation of jets due to large disturbances at the jet surface and turbulent motion may be relevant to some degree but only in an initial phase until establishment of a quasi-steady coherent jet length. In this respect, the present review of the jet breakup modeling addresses the parameterization in the basic Kelvin-Helmholtz approach in view of possible reactor conditions. It refers firstly to questions on the relative velocity between melt and ambient fluid, as well as the density of this fluid. Further, the stripping description (i.e. adaptation parameters related to wavelength for stripping amplitude, stripping surface part and drop diameter) must have a good mathematical basis. It concerns a question, whether a generalized understanding and also adaptation approach over a

wide range of conditions is possible. It is to be remarked that the adaptation parameters do not allow an arbitrary playing and are to be chosen plausibly with respect to the wavelength and the stripping surface area.

The extended approach is mainly based on the wave stripping approach due to Kelvin-Helmholtz instabilities used in IKEJET [40]. The approach based on the relative steam flow in “thick film” is extended for applicability in reactor scenarios with very thick and thus long jets in deep water pools. The mathematical model of the extended approach is presented below.

Extension of the jet breakup modeling for long jets

The jet behavior is described by a separate model for a representative jet, which yields the jet penetration in water and the fragmentation rate along the jet. The jet fragmentation is presently described as stripping of Kelvin-Helmholtz (KH) waves at the sides of the melt jet in relative steam flow [51]. It is assumed that the KH wavelength is small enough to provide a local stripping pattern, depending on the local steam flow. In the previous approach, the steam flow along the jet has been determined by a separate simplified balance of the driving head of the mixture around the jet with a length L and the inertia of the steam flow:

$$\frac{1}{2}\rho_v v_v^2 = \rho_a g\left(L - z\right) \tag{4-37}$$

where z is the axial coordinate measured downwards from the water level along the jet (i.e. the driving head at location z). This separate model has been chosen due to the complications to determine the mean fluid density and velocity of multi-phase flow ρ_v and v_v directly from the premixing. The approach with mean fluid velocities and densities directly taken from the pre-mixing occurs non-applicable, yet, due to uncertainties concerning the determination of ρ_v and v_v, the fluctuation zone as well as dependence on discretization close to the jet.

The interaction effect of the steam flow with the jet and the surrounding mixture had been considered by assuming the velocity profile in the steam flow along the jet. For this, a reduction factor ζ on vapor velocity v_v is defined:

$$v_v = \zeta\sqrt{\frac{\rho_a}{\rho_v} g\left(L - z\right)} \tag{4-38}$$

Although adaptations with this parameter yielded quite good agreement to FARO, KROTOS experiments [21,44,45], this approach is questionable and becomes definitely non-plausible for very thick, i.e. log jets in deep water pools in ex-vessel reactor scenarios. Here, the steam velocity corresponds to the jet length with $v_v \sim \sqrt{L_{jet}}$ and may become very high, even supersonic by very long jets.

Thus, the previous approach [51] implemented in IKEJET/IKEMIX [40] is extended in JEMI by taking into account the friction between the steam and the cloud of melt

particles around the jet, which come from the jet fragmentation. For this, the respective volume part of fragmented melt is to be determined.

Model description

A short model description of the present stripping approach is given as follows. For the steam flow, a steady state approach yields (measured upwards from the jet leading edge):

$$v_v \frac{dv_v}{dx} = g\left(\frac{\rho_a}{\rho_v} - 1\right) - \frac{3}{4} \cdot \frac{c_{Dp}}{D_p} \cdot \alpha_p \cdot \left(v_v - v_p\right)^2 \tag{4-39}$$

With $v_p << v_v$, the result is

$$v_v^2 = \frac{A}{B} - \frac{A}{B} \cdot e^{-2Bx} \tag{4-40}$$

with $A = g\left(\frac{\rho_a}{\rho_v} - 1\right)$ and $B = \frac{3}{4}\frac{c_{Dp}}{D_p}\alpha_p$.

For realistic conditions, it can be seen that v_v rapidly reaches a constant value

$$v_v = \sqrt{\frac{A}{B}} \tag{4-41}$$

which can be treated as varying slowly (in a quasi-steady approach) with local values of ρ_a, D_p and α_p.

From the KH model [51], the wave growth is given by

$$\eta = \eta_0 \, e^{kc_i t} \tag{4-42}$$

with

$$c_i = \frac{1}{\sqrt{3}} \sqrt{\frac{\rho_v}{\rho_m}} \cdot u_a \tag{4-43}$$

For u_a, it is set

$$u_a = f_{fl} \cdot \left(v_v + v_j\right) \tag{4-44}$$

The parameter f_{fl} accounts for the effect of a velocity profile of surrounding flow at the jet. It must be smaller than 1. In a simplified stripping approach (as compared to earlier approaches), the locally stripped drop size is related to a wave amplitude to the wavelength by

$$D_p = f_d \cdot \lambda = f_d \cdot \frac{3\pi\sigma}{\rho_v \cdot u_a^2} \tag{4-45}$$

The factor f_d means the part of the stripping amplitude to strip off. It should also be smaller than 1 in order to remain in plausible size ranges for the stripping amplitude. The simplified linear approach (see Eqs. 4-42, 4-43 and 4-45) can be extended for wave growth. The stripping wave length then corresponds to the amplitude of separation (*sep*) $\eta_{sep} = f_{sep} \cdot \lambda$. It can be determined beyond the basic amplitude (*B*) $\eta_B = f_B \cdot \lambda$ where the stripping process is considered to start. Geometrically, the wave crest approximately corresponds to the approach for D_p, if

$$f_{sep} = f_B + \frac{8}{3} f_d^3 + \left[\frac{16}{3} f_d^3 \left(f_B + \frac{4}{3} f_d^3 \right) \right]^{\frac{1}{2}} \tag{4-46}$$

Fig. 4-2 shows schematically the geometrical description of wave growth modeling.

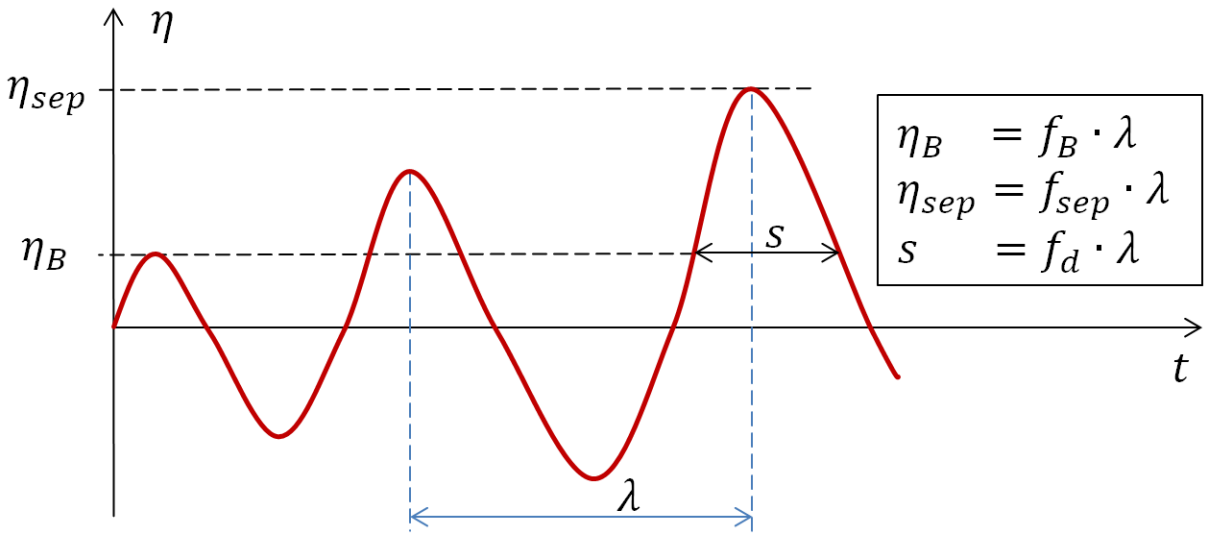

Fig. 4-2: Geometrical description of wave growth modeling.

On the other hand, the mass separation may more simply be considered as flow of melt beyond the basic amplitude η_B over a part of the surface of the jet:

$$\dot{m}_{fr} = \dot{\eta}_B \cdot \frac{F_{strip} \cdot \rho_{melt}}{F_{total}} = \dot{\eta}_B \cdot f_F \cdot \rho_{melt} \tag{4-47}$$

For the factor $f_F = F_{strip} / F_{total}$, a part of the wavelength (f_F) may be taken as characteristic value. For the wave growth, KH yields

$$\dot{\eta}_B = \eta_B \cdot kc_i \tag{4-48}$$

Thus:

$$\dot{m}_{fr} = \eta_B \cdot kc_i \cdot f_F \cdot \rho_{melt} \tag{4-49}$$

Accordingly, f_F also defines the volume part of separated melt drops directly at the melt surface: $\alpha_p = f_f$. However, the reduction of this value is obtained considering that the final separation occurs according to the above discrete approach of drop separation with velocity $\dot{\eta}_{sep}$ rather than that with $\dot{\eta}_B$ in the continuous outflow approach at η_B. Then, the corrected α_p results from the real versus the "continuous" drop velocity as

$$\alpha_{p,\,corr} = \alpha_p \cdot \frac{\dot{\eta}_B}{\dot{\eta}_{sep}} = f_F \cdot \frac{\eta_B}{\eta_{sep}} = f_F \cdot \frac{f_B}{f_{sep}} \tag{4-50}$$

This α_p value is used in the above determination of v_v and thus yields a feedback with the fragmentation which is locally iterated.

The four independent parameters f_{fl}, f_d, f_F and f_B are thus used in the present modeling. The sense of introducing these separate parameters is that they are related to specific parts of the process, which allow consideration of specific effects. Further, this restricts the choice of the parameters as indicated. It is also obvious (and can be demonstrated by the calculations) that the interdependence of the effects yields additional limitations to reasonable choices. Especially, these limitations become visible by trying to get a consistent formulation yielding agreement with the experimental results over a wide range of conditions. Following values are considered as appropriate: $f_{fl} = 0.5$, $f_d = 0.2$, $f_F = 0.25$ and $f_B = 0.7$

The vapor density ρ_v has presently been chosen at saturation values. One may rather think of choosing the density at the melt temperature, assuming rapid adaptation to the cloud of drops close to the jet. However variations with the simplified model showed that the overall influence on fragmentation is not that large, due to the combination with the steam velocity which becomes larger with smaller ρ_v

.

An approach for the lateral drop velocity at separation influencing the lateral cloud dispersion is given by

$$u_p = \dot{\eta}_{sep} = \eta_{sep} \cdot k c_i = f_{sep} \cdot 2\pi c_i \tag{4-51}$$

The jet velocity is taken for the initial drop velocity in axial direction $v_p = v_{jet}$.

Concluding, the approach of jet fragmentation in a vapor film based on the formulation for Kelvin-Helmholtz wave growth had been given with the earlier model based on the determination of v_v without taking into account friction at the melt drops. This deficit has been now corrected. The improved modeling is now available in a simplified formulation for further use in the mixing code. The validation of the extended modeling based on the FARO and KROTOS (as partial results for detonation calculations) experiments has been discussed in Chapter 6.

4.5 Melt drops

In the course of extending the premixing model to 3D, several weaknesses in the existing modeling of the melt phase have been indicated. First, the treatment the melt phase using the Eulerian approach goes beyond the scope of the numerics and the computability due to the complexity and immense computer memory needs. The implementation of the melt phase in the Eulerian approach catastrophically slows down calculations. This means a strong reduction of the simulation time step to microseconds and smaller and an increase of iteration number required for solving the linearized conservation equations in the semi-implicit numerical approach used in JEMI. Second, the use of the Eulerian formulation for the melt phase supports a so-called “data-smearing” from the modeling standpoint. This means, the temperature and the velocities of all melt particle groups are being averaged in the respective discrete volume and presented as one. The “smeared” data is used for the exchange with the coolant phases and then stored back into each melt group in the cell equaling them. Thus, the previous data, especially the temperature, gets lost and the newly calculated data is decoupled from the reality. This averaging approach becomes questionable particularly by melt groups with different ages, e.g. “young” still liquid particles with higher enthalpy and “old” partly or completely solidified particles. The information of solidification status of each melt drop is required in the explosion/detonation phase of steam explosion, see Chapter 2.3

As possible improvement, an approach with classification of different particle groups in each volume cell was considered. Such extended classification (i.e. differentiated by velocities or temperature), intended to be implemented in the program code MC3D [35], is again limited by the numerics and the computability. Here, additional conservation equations for each particle class in each Eulerian cell require to be solved. Moreover, four-dimensional fields for melt phases are needed. Both features mean immense computer memory needs, small time steps and dramatic increase of computational costs making the approach inapplicable.

Another approach to represent the melt phase is the Lagrangian method. Here, the melt drops are described as a representative particle or particle cluster. It is firstly created during jet fragmentation and at the end of its age destroyed by settling to debris bed. Each representative particle or cluster has its own diameter, effective surface (defined by effective number of single particles), age, velocity vector and enthalpy. Depending on the locations, the particle interacts with the coolant phases in the respective volume cell exchanging the momentum and energy. Thus, the exact progress of the cooling, the development of the surface temperature and solidification can easily and correctly be tracked. The surface temperature of the melt drop determines the heat transfer from melt to coolant and thus the void generation. The biggest advantage of the Lagrangian approach is the independence from the grid nodalization. The numerical discretization for the melt phase is solely given by the

number of representative particles, which is determined only by the jet breakup. Additionally, the number of representative particles can be reduced by changing the number of single particles in each cluster on the fly. This makes the approach more flexible. The memory overload, slow-down and abort of the simulation can be avoided. The explicit coupling of the melt phase with the coolant phases is a further advantage of the Lagrangian approach. This brings gains for the computability reducing the computational costs. Also, the data smearing is avoided, since each particle can be tracked.

In the premixing code JEMI, the Lagrangian method for the representation of melt drops have been favored to be implemented due to better applicability compared to the Eulerian approach. For usual applications, the number of particle clusters/groups can be chosen large enough, usually between 10'000 and 20'000. This allows one to follow the development of properties of particles in detail, even with long falling times in deep water pools as well as in configurations with multiple jets. A multi-jet fragments more intensively due to larger stripping surface area.

Model description

Clusters as representative particles are generated as follows: the jet line (center-line) is initially divided axially into a certain number of intervals (given via input) with axial length Δz. For each time step with duration Δt and each interval on the jet (for which fragmentation takes place) a group of particles is generated being initially in a volume:

$$V_d = \pi \cdot \left[(R_j + u_d \cdot \Delta t)^2 - R_j^2 \right] \cdot \Delta z \tag{4-52}$$

into which the mass is stripped off:

$$m_d = \dot{M} \cdot \Delta z \cdot \Delta t \,. \tag{4-53}$$

The number of drops in such a representative particle group is

$$n_d = \frac{3\, m_d}{4\, \pi R_d^3 \rho_m} \,. \tag{4-54}$$

The radius of the melt drop is defined by the jet breakup discussed in Section 4.4.

Each cluster has its own velocity, enthalpy, diameter, age. Additionally, each cluster has its own inner and surface temperatures as well as the crust thickness related to a single particle in the cluster. The development of surface temperature and crust can be exactly determined due to particle tracking by solidification model created the present work. The solidification model is implemented in JEMI in a separate module CFOR, see Section 4.7.

Drop dynamics

For a group of representative drops, the equation of motion is given by

$$m_d \frac{d\vec{v}_d}{dt} = m_d (1 - \frac{\rho_a}{\rho_m}) \cdot \vec{g} + n_d \vec{F}_p \text{,} \tag{4-55}$$

where the drag force on a single spherical particle $\vec{F}_p$ is essentially the hydrodynamic drag, i.e. based on the pressure influences from the surrounding flow. In general form, $\vec{F}_p$ is given by

$$\vec{F}_p = c_d \cdot \frac{1}{2} \pi R_d^2 \cdot \rho_a |\vec{v}_{rel}| (\vec{v}_a - \vec{v}_d) \text{.} \tag{4-56}$$

Mixture densities and velocities of the ambient coolant phases (ρ_a, $\vec{v}_a$) are used in order to consider different flow regimes. They yield an influence of void in mixture on the particle movement. Following assumptions are valid. The ambient fluid corresponds to liquid with $\rho_a = \rho_l$, $\vec{v}_a = \vec{v}_l$ in the water-continuous regime (steam bubbles in water). In the vapor-continuous regime (water droplets in steam), the vapor is ambient, i.e. $\rho_a = \rho_g$, $\vec{v}_a = \vec{v}_g$. In the transition range assumed between flow patterns, the fluid properties (i.e. the density and velocity as well as friction and heat transfer) are derived from the respective values at the chosen boundaries. These are *0.3* and *0.7* of void fraction for liquid and vapor-continuous regimes, respectively. The underlying idea is that the transition states are composed of water-rich and steam-rich patterns, at the conditions of the boundaries of the transition regime, respectively. Practically, linear interpolation is done between the boundaries. For the transition range, between the liquid- and vapor-continuous regimes, the ambient density is expressed by

$$\rho_a = \frac{\alpha_g \rho_g + \alpha_l \rho_l}{\alpha_g + \alpha_l} \tag{4-57}$$

and the ambient velocity:

$$\vec{v}_a = \frac{\rho_g \vec{v}_g + \rho_l \vec{v}_l}{\alpha_g \rho_g + \alpha_l \rho_l} \text{.} \tag{4-58}$$

$\vec{v}_g$ and $\vec{v}_l$ are volumetric velocities relating to the real velocities $\vec{v}_g = \alpha_g \vec{u}_g$ and $\vec{v}_l = \alpha_l \vec{u}_l$, respectively.

4.6 Heat transfer between melt and fluid

Heat transfer from the melt drops to the coolant is described depending on the flow patterns, in a similar way as for friction. The energy balance for a single spherical particle is given by:

$$m_p \frac{\mathrm{d}e_p}{\mathrm{d}t} = q_{surf} \cdot \pi \cdot D_p^2 \,, \tag{4-59}$$

with internal energy e_p and surface heat flux q_{surf}. The heat flux q_{surf} corresponds to the surface temperature of the melt drop T_{surf}:

$$q_{surf} = q_{surf}\left(T_{surf}\right) \tag{4-60}$$

Two mechanisms of the heat transfer are considered: forced convection film boiling and heat radiation. Combining both radiation and forced convection yields the total surface heat flux from the melt drop to the coolant:

$$q_{Surf} = q_{film} + q_{Rad} \tag{4-61}$$

The film boiling is considered to be relevant in the water-continuous regime: the melt drop is surrounded by water. The modeling of the film boiling is based on the description of Epstein and Hauser for forced convection film boiling [71]. For the ambient velocity and properties, the water values have been taken.

The correlation of Epstein and Hauser can be written as

$$q_{film} = h_{film}\left(T_d - T_{sat}\right) = 2.5 \cdot \frac{\kappa_v}{D} \cdot \frac{\mathrm{Re}_l^{\frac{1}{2}}}{\beta} \cdot \frac{\mathrm{Pr}_v\, h_{lv}}{c_{pv}} \cdot \left[\frac{A^3}{24} + \left(\frac{2}{\pi}\right)^2 B^4\right]^{\frac{1}{4}} \,, \tag{4-62}$$

with

$$A = \frac{c_{pv}\left(T_d - T_{sat}\right)}{\mathrm{Pr}_v\, h_{lv}} \,, \tag{4-63}$$

$$B = \beta \frac{\kappa_l}{\kappa_v} c_{pv} \frac{T_{sat} - T_l}{\mathrm{Pr}_v\, h_{lv}} \mathrm{Pr}_l^{\frac{1}{2}} \,, \tag{4-64}$$

$$h_{lv} = h_{v,sat} - h_{l,sat} \tag{4-65}$$

$$\beta = \left[\left(\frac{\rho_\mathrm{l}}{\rho_\mathrm{v}}\right)^{\frac{1}{2}} \cdot \frac{\nu_\mathrm{v}}{\nu_\mathrm{l}}\right]^{\frac{1}{2}} \,, \tag{4-66}$$

$$\mathrm{Re}_l = \frac{\left|\vec{v}_d - \vec{v}_l\right| D}{\nu_l} \,. \tag{4-67}$$

A is related to the superheat of melt to water. *A* can be considered as tending to zero for getting the limiting case $q_l \approx q_{film}$, thus yielding

$$q_l = \frac{\lambda_l}{D}\left(T_{sat} - T_l\right) \cdot 2.5 \left(\frac{2}{\pi}\right)^{\frac{1}{2}} \cdot \mathrm{Re}_l^{\frac{1}{2}} \cdot \mathrm{Pr}_l^{\frac{1}{2}} \tag{4-68}$$

or as Nusselt relation for the heat transfer from the interface to water:

$$Nu_l = 2.5 \cdot \left(\frac{2}{\pi}\right)^{\frac{1}{2}} \cdot \mathrm{Re}_l^{\frac{1}{2}} \cdot \mathrm{Pr}_l^{\frac{1}{2}} \approx 1.99 \cdot \mathrm{Re}_l^{\frac{1}{2}} \cdot \mathrm{Pr}_l^{\frac{1}{2}}. \tag{4-69}$$

This yields a factor ≥ 3 as compared to the classical correlations for solid spheres.

In general, an increase of heat transfer from the melt drops and from the interface to water is expected from interface instabilities and turbulence effects (e.g. separation of bubbles). In contrast, an increase in vapor film thickness due to the additionally considered heat radiation and thus more significant evaporation may yield a reduction of the convective part of heat transfer under film boiling. However, such effects are not included in the present modeling.

The radiation heat transfer to the coolant is taken into account as an additional contribution in all flow regimes: the water-, vapor-continuous and transition regimes. The radiation heat flux per surface unit is given by

$$q_{Rad} = \varepsilon\sigma \cdot \left(T_{Melt}^4 - T_{Coolant}^4\right), \tag{4-70}$$

with emissivity ε and Stefan-Boltzmann constant σ. The emissivity ε is taken as *0.7* for corium. The radiation heat transfer is considered to be independent of water content. Certainly, this becomes problematically for high voided regions, since there is no sufficient water to completely absorb the heat. However, the radiant heat can be absorbed in neighboring regions with higher water content or by neighboring structures. The long range radiation heat flux is considered as a part, which is not absorbed in the considered region and to be transported to the neighboring regions.

As already discussed, the heat transfer from melt droplet to coolant depends on the flow regimes. The radiative heat transfer is practically independent of steam content in mixture in due consideration of long range radiation. It contributes mostly to steam production. In the case of a mixture with void close to 1, heat transfer occurs to distant regions having more liquid phase. The convective heat transfer strongly depends on the flow pattern. It can be neglected by high voided mixtures, since no stable vapor film can exist in vapor. In the transition regime between the water-continuous and vapor-continuous flow patterns, a linear interpolation is applied. Thus, the total heat flux from melt droplet to coolant is expressed by:

$$q_{Surf} = q_{Rad} + C_{FB} q_{film}, \tag{4-71}$$

where C_{FB} is a partition factor on the film boiling part depending on void:

$$C_{FB} = \begin{cases} 1, & \alpha \leq 0.3 \\ 1.75 - 2.5 \cdot \alpha, & 0.3 < \alpha < 0.7 \\ 0, & \alpha \geq 0.7 \end{cases}. \tag{4-72}$$

Fig. 4-3 visually shows the development of the factor C_{FB} on the film boiling as a function of void.

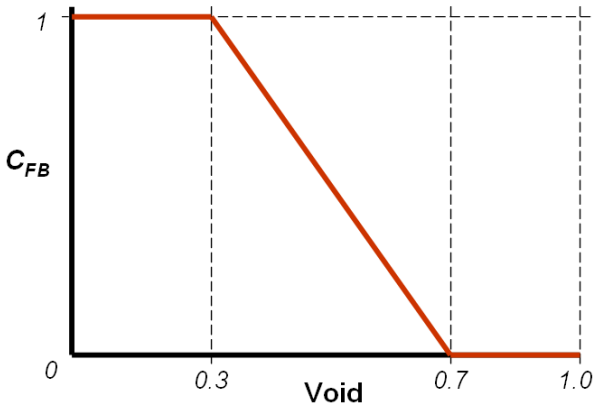

Fig. 4-3: Factor C_{FB} on the film boiling as a function of void

The total volumetric heat flux from the melt drops (presented using the Lagrangian formulation) to coolant correlating with Eq. 4-11 is given as

$$Q_{d,total} = V_{i,j,k} \sum_{n=1}^{npac} \left(A_{surf,n} \cdot q_{surf,n} \right) \tag{4-73}$$

4.7 Solidification of melt drops

Several steam explosion experiments KROTOS [21], PREMIX [22-26] demonstrated a difference in behavior between simulant melts as aluminum oxide Al_2O_3 and the corium. The transfer rate of thermal energy for corium is significantly lower than that for simulant aluminum oxide, as concluded by [72,73]. Moreover, steam explosions were never triggered spontaneously if corium is used; in contrary to easy triggering steam explosions with aluminum oxide. The possible explanation is the smaller fragment size during the premixing in the experiments with corium of ~3 mm to smaller fragments of ~10-15 mm in the experiments with aluminum oxide. This is supposed due to differences in the material properties. Since the corium has a low thermal conductivity, a significant difference between the surface temperature and the inner temperature of a corium drop may develop during moving in the water/steam environment. Therefore, the solidification process can start much earlier by corium than that by aluminum oxide. The smaller fragment size supports the solidification process and the occurrence of a solid layer (crust) at the surface of a hot droplet and thus limits the ability to the spontaneous triggering. Additionally, a strong reduction of the drop surface temperature causes a decrease of the heat transfer to the surrounding fluid, by heat radiation and film boiling as well, affecting the void buildup during the premixing.

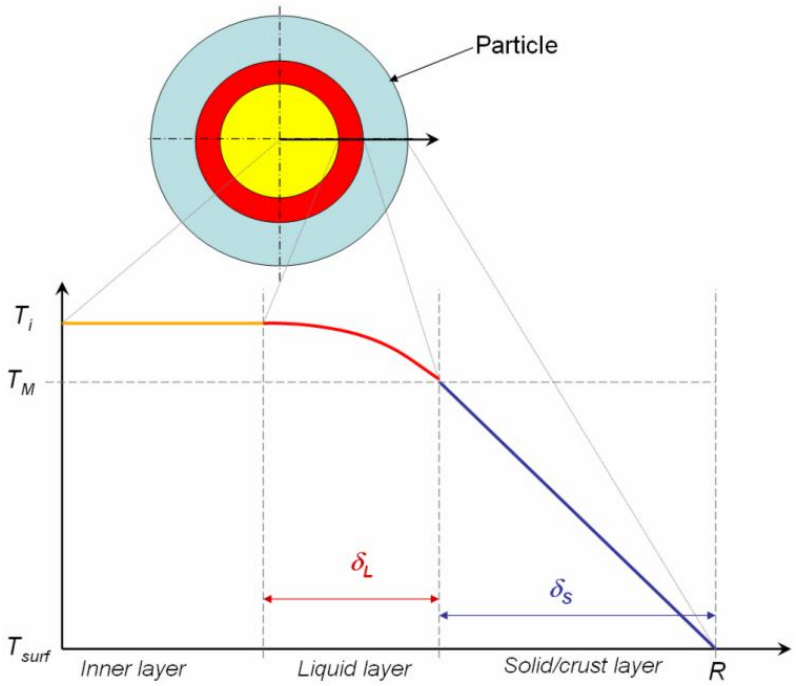

Fig. 4-4: **The surface temperature drop model, two different temperature profile assumed in the liquidus and solidus regions**

During the detonation (and fine fragmentation), the solidification of melt drops is one of the most important effects for the occurrence and the violence of steam explosions. A significant growth of crusts at the surface during the premixing stage can strongly inhibit or even prevent rapid fine fragmentation of melt drops and thus pressure escalations in fuel-coolant interactions.

In the premixing model JEMI, the solidification of the melt drops is described by CFOR (**C**rust **FOR**mation) model. CFOR is initially based on a surface temperature drop approach proposed by Moriyama et al. [74]. In CFOR, Moriyama approach is extended assuming two different temperature profiles in liquidus and solidus regions of a spherical particle. A quadratic temperature profile is assumed for a thermal boundary layer in the liquidus region and a linear profile in the solidus region, see Fig. 4-4. Also the change of the heat flux as function of the drop surface temperature is here considered. The existence of the mushy zone is neglected. Mushy zone is referred to a region between liquidus and solidus point, where the onset of crystallization occurs. The storage and release of the latent enthalpy are assumed at the solidification front corresponding to the melting temperature.

Mathematical model

The concept of the model is illustrated in Fig. 4-4. A particle with the uniform initial temperature T_i cooled at the surface is considered. The transient heat conduction equation for a sphere is given by:

$$\rho c \frac{\partial T}{\partial t} = \lambda \left(\frac{\partial^2 T}{\partial r^2} + \frac{2}{r} \frac{\partial T}{\partial r} \right) \tag{4-74}$$

where T, c, ρ and λ are the temperature, specific heat capacity, density and thermal conductivity, respectively. Boundary conditions at the surface, solid and liquid fronts of a spherical particle can be defined as:

$$\begin{aligned}
&\left[Solidus\ \ layer : r = R \right] : T_L = T_{surf}, \left\{ -\lambda \frac{\partial T_S}{\partial r} = q_{surf}(t) \right\} \\
&\left[Liquidus\ \ layer : r = R - \delta_S \right] : T_L = T_S = T_M, \left\{ -\lambda \frac{\partial T_L}{\partial r} = -\lambda \frac{\partial T_S}{\partial r} + H_{fus} \rho \cdot \frac{d\delta_S}{dt} \right\} \\
&\left[Inner\ \ layer : r = R - \delta_S - \delta_L \right] : T = T_i, \left\{ \frac{\partial T_L}{\partial r} = 0 \right\}
\end{aligned} \tag{4-75}$$

with R is the sphere radius, δ_L and δ_S is the thickness of the liquidus and solidus/crust boundary layers, respectively. H_{fus} stands for the latent enthalpy storages in the particle being released at the solid front $\left[r = R - \delta_S \right]$. No “mushy”-zone is considered: $T_{Liquidus} = T_{Solidus} = T_{melting}$.

According to Eqs. 4-62 and 4-70, the heat flux at the surface of the particle is defined as a function of the surface temperature including the heat flux from the heat radiation and film boiling:

$$q_{surf} = \varepsilon\sigma \cdot \left(T_{surf}^4 - T_{bulk}^4 \right) + h_{FB} \cdot (T_{surf} - T_{bulk}) \tag{4-76}$$

where ε, σ and $h_{FB} = h_{FB}(T_{surf})$ are the emissivity, the Stefan-Boltzmann constant and the heat transfer coefficient for the film boiling as a function of the surface temperature, respectively.

Integration of (4-74) after multiplication with surface $4\pi r^2$ gives:

$$\begin{aligned}
&4\pi\rho \int_0^R c_p \frac{\partial T}{\partial t} \cdot r^2 dr = 4\pi\lambda \int_0^R r^2 \frac{\partial^2 T}{\partial r^2} dr + 4\pi 2\lambda \int_0^R r \frac{\partial T}{\partial r} dr = 4\pi\lambda \cdot R^2 \frac{\partial T}{\partial r}\Big|_R \\
&4\pi\rho \frac{d}{dt} \int_0^R c_p \cdot T \cdot r^2 dr = -4\pi R^2 q_{surf}
\end{aligned} \tag{4-77}$$

Heat loss at time *t* can be defined as:

$$\Delta Q^{loss} = \left\{ Q_{t=0} - Q_{t=t} \right\} \tag{4-78}$$

Thus, the heat loss corresponding to the heat flux at the surface of spherical particle can be represented by

$$-4\pi R^2 q_{surf} = \frac{\Delta Q^{loss}}{\Delta t} = \frac{dQ^{loss}}{dt} \tag{4-79}$$

Further simplifications are to be made:

$$\begin{aligned} &\rho_L = \rho_S = \rho = const, \\ &\lambda_L = \lambda_S = \lambda = const, \\ &c_L \neq c_S,\ \ c_L = const,\ \ c_S = const \end{aligned} \tag{4-80}$$

Motivated by the idea of Moriyama [74], two different temperature profiles are considered in CFOR: a quadratic profile – for the temperature range above the melting temperature T_{melt} (liquidus layer) and a linear profile for the temperature range below T_{melt} (solidus layer).

The linear temperature profile in the solidus/crust layer with the boundary conditions from Eq. (4-75) at the solid front is given by

$$T_S(r) = T_M - \frac{T_M - T_{surf}}{\delta_S}[r - (R - \delta_S)] \tag{4-81}$$

The quadratic temperature profile in the liquidus layer analog to (4-81) is given by

$$T_L(r) = T_i - \frac{T_i - T_M}{\delta_L^2}[r - (R - \delta_S - \delta_L)]^2 \tag{4-82}$$

The heat loss after a certain time can be expressed by a temperature drop in all boundary layers:

$$\begin{aligned} Q_{pac}^{loss} &= 4\pi\rho \cdot \int_0^R c(T) \cdot \left[T_i - T(r)\right] \cdot r^2 dr = \\ &= 4\pi\rho \cdot c_L \int_{R-\delta_S-\delta_L}^{R-\delta_S} \left[T_i - T_L(r)\right] \cdot r^2 dr + 4\pi\rho \cdot c_L \int_{R-\delta_S}^{R} \left[T_i - T_M\right] \cdot r^2 dr + \\ &+ 4\pi\rho \cdot H_{fus} \int_{R-\delta_S}^{R} r^2 dr + 4\pi\rho \cdot c_S \int_{R-\delta_S}^{R} \left[T_M - T_S(r)\right] r^2 dr \end{aligned} \tag{4-83}$$

where the first and second terms yield the contribution of the inner and liquid layers; the third and the last term describe the contribution of the latent heat and the solid/crust layer, respectively.

Integration of Eq. (4-83) gives the total energy loss in particle:

$$Q_{pac}^{loss} = M_L c_L (T_i - T_M) \cdot F_L + M_S c_L (T_i - T_M) + M_S \cdot H_{fus} + M c_S (T_M - T_{surf}) \cdot F_S \tag{4-84}$$

where M_L, M_S, M are the masses of liquidus, solidus parts and the total particle mass. F_L and F_S are the respective profile functions:

$$\left.\begin{aligned} M_L &= 4/3\,\pi(R-\delta_s)^3\cdot\rho \\ M_S &= 4/3\,\pi\left\{R^3-(R-\delta_s)^3\right\}\cdot\rho \\ M &= 4/3\,\pi R^3\cdot\rho \\ F_S &= \frac{\delta_S}{R}\left[\frac{3}{2}-\frac{\delta_S}{R}+\frac{1}{4}\left(\frac{\delta_S}{R}\right)^2\right] \\ F_L &= \frac{\delta_L}{R-\delta_S}\left[1-\frac{1}{2}\frac{\delta_L}{R-\delta_S}+\frac{1}{10}\left(\frac{\delta_L}{R-\delta_S}\right)^2\right] \end{aligned}\right\} \tag{4-85}$$

Connecting and linearizing Eq. (4-84) and Eq. (4-79), we have

$$\begin{aligned} 4\pi R^2 q_{surf} &= \frac{dQ_{PAC}^{loss}}{dt} \equiv \frac{\partial Q_{PAC}^{loss}}{\partial T_{surf}}\frac{dT_{surf}}{dt}+\frac{\partial Q_{PAC}^{loss}}{\partial T_i}\frac{dT_i}{dt}+\frac{\partial Q_{PAC}^{loss}}{\partial \delta_L}\frac{d\delta_L}{dt}+\frac{\partial Q_{PAC}^{loss}}{\partial \delta_S}\frac{d\delta_S}{dt}= \\ &= -Mc_S F_S\cdot\frac{dT_{surf}}{dt}+M_L c_L(T_i-T_M)\frac{\partial F_L}{\partial \delta_L}\cdot\frac{d\delta_L}{dt}+(M_L c_L F_L+M_S c_L)\cdot\frac{dT_i}{dt}+ \\ &+\left\{\begin{aligned} &M_L c_L(T_i-T_M)\cdot\frac{\partial F_L}{\partial \delta_S}+c_L(T_i-T_M)F_L\cdot\frac{\partial M_L}{\partial \delta_S}-c_L(T_i-T_M)\cdot\frac{\partial M_L}{\partial \delta_S}- \\ &-H_{fus}\frac{\partial M_L}{\partial \delta_S}+Mc_S(T_M-T_{surf})\cdot\frac{\partial F_S}{\partial \delta_S} \end{aligned}\right\}\cdot\frac{d\delta_S}{dt} \end{aligned} \tag{4-86}$$

The surface heat flux q_{surf} should satisfy the continuity from Eq. (4-75):

$$T_M-T_{surf}=\frac{q_{surf}}{\lambda}\delta_S \tag{4-87}$$

The energy balance at the solidification front $r=R-\delta_S$ yields

$$H_{fus}\rho\frac{d\delta_S}{dt}=\lambda\frac{T_M-T_{surf}}{\delta_S}-2\lambda\frac{T_i-T_M}{\delta_L} \tag{4-88}$$

The following system equation is to be solved:

$$\begin{cases} \delta_S = f\left(T_{surf}, q_{surf}\right) \\ \delta_L = f\left(\delta_S, \dfrac{d\delta_S}{dt}, T_{surf}\right) \\ \dfrac{dT_{surf}}{dt} = f\left(\delta_S, \dfrac{d\delta_S}{dt}, T_{surf}, \dfrac{dq_{surf}}{dt}\right) \\ \dfrac{d\delta_L}{dt} = f\left(\delta_L, \delta_S, \dfrac{d\delta_S}{dt}, T_{surf}, \dfrac{dT_{surf}}{dt}\right) \\ \dfrac{d\delta_S}{dt} = f\left(\delta_L, \delta_S, T_{surf}\right) \end{cases} \tag{4-89}$$

Solution procedure:

Three general solidification states are distinguished in the considered approach:

1. no solidification: only liquid layer exists, the surface temperature is above the melting point;
2. partial solidification: both liquid and solid layers exist, the surface temperature is below and the inner temperature is above the melting point;
3. complete solidification: the solid layer is equal the radius, both surface and inner temperature are below the melting point.

General numerical procedure can be shown as follows. For the first time step as the particle is just generated, the initial thickness of the liquid layer δ_L needs to be evaluated by the first order of the analytical solution proposed by Moriyama [74]:

$$\delta_L = \sqrt{6\frac{\lambda}{c\rho}dt} \tag{4-90}$$

If no solidification occurs, i.e. only the liquid layer exists and the surface temperature is above the melting temperature, the new temperature at the drop surface T_{surf} and is determined by

$$T_{surf}^{new} = T_i - \frac{q_{surf}}{2\lambda}\delta_L \tag{4-91}$$

The change of surface temperature dT_{surf}/dt is obtained by

$$\frac{dT_{surf}}{dt} = \frac{T_{surf}^{new} - T_{surf}}{\Delta t} \tag{4-92}$$

Simplifying Eq. 4-86 by considering the non-existence of the solid layer, the change of liquid layer $d\delta_L/dt$ and the new layer thickness can be obtained by

$$\frac{d\delta_L}{dt} = -\frac{Aq_{surf} - 4/3\,\pi R^3 \cdot \rho c F_L \dfrac{dT_{surf}}{dt}}{4/3\,\pi R^3 \cdot \rho c (T_i - T_{surf}^{new}) \dfrac{\partial F_L}{\partial \delta_L}} \tag{4-93}$$

If a partial solidification occurs, the change of δ_S additionally is considered. According to Eq. 4-87, the new surface temperature T_{surf} and the change of the surface temperature dT_{surf}/dt are determined using the actual surface heat flux q_{surf} from melt to coolant calculated by the mixing model:

$$T_{surf}^{new} = T_M - \frac{q_{surf}}{\lambda}\delta_S \tag{4-94}$$

where T_M is the melting temperature of the material assuming constant during the solidification. At the melting temperature, the release of the solidification enthalpy is assumed. According Eq. 4-86, the change of the crust thickness (solid layer) $d\delta_S/dt$ is expressed:

$$\frac{d\delta_S}{dt} = \frac{Aq_{surf} + Mc_S F_S \cdot \dfrac{dT_{surf}}{dt} - M_L c_L (T_i - T_M) \dfrac{\partial F_L}{\partial \delta_L} \cdot \dfrac{d\delta_L}{dt} - (M_L c_L F_L + M_S c_L) \cdot \dfrac{dT_i}{dt}}{\left\{ M_L c_L (T_i - T_M) \cdot \dfrac{\partial F_L}{\partial \delta_S} + c_L (T_i - T_M) F_L \cdot \dfrac{\partial M_L}{\partial \delta_S} - c_L (T_i - T_M) \cdot \dfrac{\partial M_L}{\partial \delta_S} - H_{fus} \dfrac{\partial M_L}{\partial \delta_S} + Mc_S (T_M - T_{surf}) \cdot \dfrac{\partial F_S}{\partial \delta_S} \right\}} \tag{4-95}$$

From this, the actual value δ_S is obtained:

$$\delta_S^{new} = \delta_S + \frac{d\delta_S}{dt}\Delta t \tag{4-96}$$

The new thickness of the liquid layer is determined using Eq. 4-88:

$$\delta_L^{new} = \frac{2\lambda(T_i - T_M)}{\lambda \dfrac{T_M - T_{surf}^{new}}{\delta_S^{new}} - H_{fus}\rho \dfrac{d\delta_S}{dt}} \tag{4-97}$$

where H_{fus} is the heat of fusion released during the propagation of the solidification front. Once the liquid and solid layers reach the size of radius $\delta_S + \delta_L = R$, the relation $d\delta_S/dt = -d\delta_L/dt$ is assumed and the inner temperature starts falling. For this, Eq. 4-97 is used resulting:

$$T_i^{new} = T_M + \frac{R - \delta_S^{new}}{2\lambda}\left\{ \lambda \frac{T_M - T_{surf}^{new}}{\delta_S^{new}} - H_{fus}\rho \frac{d\delta_S}{dt} \right\} \tag{4-98}$$

Once the melt droplet solidified completely, i.e. $\delta_S = R$, the surface and inner temperature are calculated by simplifying Eq. 4-86:

$$T_{surf}^{new} = T_i - \frac{q_{surf}}{\lambda} R \tag{4-99}$$

and

$$\frac{dT_i}{dt} = -\frac{Aq_{surf} - 4/3\,\pi R^3 \cdot \rho c F_S \frac{dT_{surf}}{dt}}{4/3\,\pi R^3 \cdot \rho c F_S} \tag{4-100}$$

with

$$T_i^{new} = T_i + \frac{dT_i}{dt}\Delta t \tag{4-101}$$

The data of the melt drop (e.g. temperatures, thicknesses) from the previous time step is required in the solution procedure. The use of the explicit solution is valid since time steps are usually small enough in the mixing part ~10^{-3} s.

5 Explosion model IDEMO-3D

The IDEMO-3D code is a three-dimensional, transient multi-phase model being developed at IKE, as an advanced version of the 2D code IDEMO, proposed in [41,42,75], based on the thermal detonation concept. It describes the escalation and propagation of shock waves. The initial conditions are derived from the premixing phase assuming a pre-mixture of the melt, water and steam on a relatively coarse time scale under film boiling. In IDEMO-3D four phases are considered: melt droplets, fine debris, cold (liquid) and heated (vapor) coolant. These are treated as interpenetrating, quasi-continuous fluids sharing the same pressure. Melt droplets and fine debris are presumed as incompressible. In order to produce initial fluid movement initiating the fine fragmentation, a sufficiently strong trigger must be initially defined. As a result, the fine fragmentation causes strong evaporation of water and local pressure buildup. Once the trigger is strong enough to induce local pressure escalations generating a shockwave, the propagation of the shockwave and further pressure escalations then depend only on the mixture explosiveness characterized by mass fraction of liquid melt prone to fine fragmentation, water and steam content in the mixture region, discussed in detail by [76,77].

In the frame of extending the detonation model to 3D, several deficits in the existing modeling are detected. The development of a solid layer at the surface of melt drops during the premixing phase was not considered meaning that all drops can participate in fine fragmentation. This leads to overestimation of steam explosion magnitude as well as to creation of unreal homogeneities in mixtures. In reality, a solid crust develops at the surface of melt drops due to cooling during the premixing stage. In order to consider the amount of already solidified melt during the premixing, a “rule of thumb” of 15% of the total melt had been used in explosion calculations for corium [77]. The 15%-value comes from a separate consideration for one melt drop being fragmented from a melt jet at different axial locations and falling in water with different falling times. In general, the participation and yield of each drop to pressure escalations is determined by shock wave propagation velocity and the solidification degree, i.e. actual crust thickness. Here, the solid crust counteracts hydrodynamic forces leading to surface instabilities. It limits or even inhibits the drop breakup and further fine fragmentation. Ceramic melts with high densities and low thermal conductivity, as corium in particular, are concerned by solidification due to quicker fall of the surface temperature below the solidus point of the material. The solidified drops (experimentally up to 85%) do not participate in fine fragmentation and not yield to pressure escalations. This was observed in KROTOS experiments with alumina and corium melts [21]. For non-symmetric 3D configurations, the amount of non-solidified and participating melt drops can change in both directions, increasing and decreasing due to initial inhomogeneities caused by asymmetric void and melt distribution. The asymmetric void and melt distribution causes the buildup of regions with differently cooled and crusted melt drops, which leads to complex interactions during pressure escalations on real conditions. Thus, the aim of the present work

was to extend the new 3D detonation model considering the different solidification degree of melt drops in order to cover the influence of solid crusts at the surface of melt drops on fine fragmentation.

5.1 Mathematical model

IDEMO-3D uses four phase formulation. The system of governing equations consists 11 equations:

- Four continuity equations for each phase;
- One constraint equation;
- Two momentum equations: one unfragmented melt and another for a representative fluid comprising the cold (liquid) and hot (vapor) fluid as well as debris;
- Three energy equations for debris, hot and cold fluids (the heat transfer from melt drop to the fluid is negligible in that short time considered during the explosion stage);
- And one transport equation formulating the usage of the melt phase as “fuel” for fine fragmentation.

Two additional conservation equations come from the approach for the discretization of melt drops into crust thickness, discussed in detail in Section 5.3.

Conservation equations

The following conservation equations for mass, momentum and energy can be applied, given here in Cartesian coordinates for simplicity

Conservation of mass applied to melt droplets (*m*), debris (*d*), cold (*c*) and heated (*h*) coolant gives:

$$\frac{\partial}{\partial t}(\alpha_m \rho_m) + \nabla\left(\alpha_m \rho_m \vec{v}_m\right) = -\Gamma_{fr} \tag{5-1}$$

$$\frac{\partial}{\partial t}(\alpha_d \rho_d) + \nabla\left(\alpha_d \rho_d \vec{v}_f\right) = \Gamma_{fr} \tag{5-2}$$

$$\frac{\partial}{\partial t}(\alpha_c \rho_c) + \nabla\left(\alpha_c \rho_c \vec{v}_f\right) = -\Gamma_E \tag{5-3}$$

$$\frac{\partial}{\partial t}(\alpha_h \rho_h) + \nabla\left(\alpha_h \rho_h \vec{v}_f\right) = \Gamma_E \tag{5-4}$$

In Eqs. (5-1) and (5-2) Γ_{fr} is the mass transfer rate due to fragmentation and in (5-3) and (5-4) Γ_E is the entrainment rate of cold coolant due to mixing.

The volume fractions of melt, debris, hot and cold coolant have to obey the volume constraint equation:

$$\alpha_m + \alpha_d + \alpha_h + \alpha_c = 1 \tag{5-5}$$

Conservation of momentum for melt droplets *(m)*, fine debris *(d)* and effective fluid (*f*), implying hot and cold coolant gives:

$$\frac{\partial}{\partial t}\left(\alpha_m \rho_m \vec{v}_m\right) + \nabla\left(\alpha_m \rho_m \vec{v}_m \vec{v}_m\right) = -\alpha_m \cdot \nabla p - \Gamma_{fr} \vec{v}_m + \vec{F}^{D}_{m,f} \tag{5-6}$$

$$\begin{aligned} &\frac{\partial}{\partial t}\left[\left(\alpha_d \rho_d + \alpha_c \rho_c + \alpha_h \rho_h\right)\vec{v}_f\right] + \nabla\left[\left(\alpha_d \rho_d + \alpha_c \rho_c + \alpha_h \rho_h\right)\vec{v}_m \vec{v}_m\right] = \\ &= -\left(\alpha_d + \alpha_c + \alpha_h\right)\cdot \nabla p + \Gamma_{fr} \vec{v}_m - \vec{F}^{D}_{m,f} \end{aligned} \tag{5-7}$$

As already mentioned, during the short time of the fuel-coolant interaction the heat exchange between the melt droplets and the other fluid phases can be neglected due to insignificant heat transfer contribution compared to the heat transfer from the fragments (debris) yielded by the fine fragmentation of melt droplets. For the same reason, the droplet temperature is assumed to be constant:

$$T_m = T_d = T_{m,0} = const \tag{5-8}$$

Energy equation for debris, cold and hot coolant gives:

$$\frac{\partial}{\partial t}\left(\alpha_d \rho_d E_d\right) + \nabla \cdot \left(\alpha_d \rho_d H_d \vec{v}_f\right) = -p \frac{\partial \alpha_d}{\partial t} + \Gamma_{fr} H_m - Q_{dh} \tag{5-9}$$

$$\frac{\partial}{\partial t}\left(\alpha_c \rho_c E_c\right) + \nabla \cdot \left(\alpha_c \rho_c H_c \vec{v}_f\right) = -p \frac{\partial \alpha_c}{\partial t} - \Gamma_E H_c \tag{5-10}$$

$$\frac{\partial}{\partial t}\left(\alpha_h \rho_h E_h\right) + \nabla \cdot \left(\alpha_h \rho_h H_h \vec{v}_f\right) = -p \frac{\partial \alpha_h}{\partial t} - \Gamma_E H_c + Q_{dh} + \vec{F}_{d,m} \cdot \left(\vec{v}_f - \vec{v}_m\right) \tag{5-11}$$

In the energy conservation equations the stagnation or total energies and enthalpies are used:

$$E_K = e_K + \frac{1}{2}\vec{v}_f, \qquad H_K = h_K + \frac{1}{2}\vec{v}_f, \tag{5-12}$$

with $k = d, c, h$ for debris, cold and hot coolant. This expression guarantees that total energy is conserved.

Changes in diameter of melt droplets are assumed to be only due to fine fragmentation. Thus, transport equation for the length scale of spherical droplets can be expressed by:

$$\frac{\partial}{\partial t}\left(\alpha_m \rho_m D_m\right) + \nabla\left(\alpha_m \rho_m D_m \vec{v}_m\right) = -\frac{4}{3}\Gamma_{fr} D_m, \tag{5-13}$$

where D_m is the diameter of a spherical melt droplet.

5.2 Constitutive laws

As previously noted, fine fragmentation of melt and heat-up of part of water ("micro-interactions") are central processes determining pressure build-up. The "micro-interactions" concept addresses non-homogeneous heat-up of coolant in addition to fragmentation denoting the probably non-conservative character of homogeneous coolant heating. The non-equilibrium heat transfer model is based on the conceptual assumption, that the heat from fragmented debris is transferred only to a part of the coolant in a "micro-interactions" zone surrounding the fuel drops, to the "hot" phase. It is postulated that the "cold" phase is too far outside and is not heated. The micro-interactions zone grows with time as cold coolant is entrained into the micro-interactions zone due to mixing.

Thermal and hydrodynamic fragmentation processes are usually distinguished in the theory. Thermally driven fragmentation processes must dominate in spontaneously triggered melt-water interactions due to the lack of sufficiently high relative velocities as well as in the initial phase. The hydrodynamic fragmentation denotes processes due to relative velocities between melt drops and coolant in strong pressure waves, especially shock waves with relatively sharp leading edges. They are considered to dominate under such conditions, in contrast to initiation and first escalation stages of a steam explosion. For reactor safety analyses, it is essential to consider a trigger in a conservative manner being sufficiently strong to create an initial fluid movement and "launch" the fine fragmentation process. Thus, hydrodynamic fragmentation is of special interest here.

In order to obtain the inherent restrictions to the hydrodynamic fragmentation process and thus also to thermal detonations, it is necessary to take into account the effects of the development of relative velocities, which are depending itself on the fragmentation process. Thus, local and instantaneous descriptions of the fragmentation are required instead of laws depending only on initial conditions. It is difficult to derive such laws from experiments alone. Understanding and to some extent modeling is required to get adequate descriptions even if formulated as correlations. Based on different assumptions on mechanisms, different laws have been constructed in more or less heuristic ways. Hydrodynamic fragmentation of melt drops in liquids by sheet stripping can be correlated as follows.

Pilch [78] correlated the experimental data for the total breakup period for droplets in gas inside the shockwave [79], see Fig. 5-1.

$$t_{fr}^{*} = c_{fr} \cdot (We_d)^m, \tag{5-14}$$

where c_{fr} is a fitting parameter, We_d is the Weber number for the drop. The constant c and the Weber number are expressed considering the respective breakup mode in Table 5-1. For the sheet stripping, it can be expressed

$$t_{fr}^{*} = c_{fr} \cdot \left(We_d\right)^{0.25} \tag{5-15}$$

Further, the dimensionless fragmentation time t_{fr}^{*} was defined by Pilch [78] as

$$t_{fr}^{*} = \frac{t_{fr}}{D \Big/ v_{rel}\left(\frac{\rho_f}{\rho_m}\right)^{0.5}} \tag{5-16}$$

where t_{fr} is the fragmentation time, D is the drop diameter, v_{rel} is the relative velocity, ρ_f is the density of the surrounding fluid and ρ_m is the melt density.

The mass of the melt drop is

$$m_d = \rho_m \frac{\pi}{6} D^3 \tag{5-17}$$

Assuming that the primary breakup of the melt drop is complete (full breakup inside the shockwave without secondary breakup), the fragmentation rate can be expressed using Eqs. 5-16 and 5-17 as

$$\frac{\mathrm{d}\, m_{Fr}}{\mathrm{d}\, t} = \frac{m_d}{t_{fr}} = \rho_m \frac{\pi}{6} D^3 \cdot \frac{v_{rel}\left(\frac{\rho_f}{\rho_m}\right)^{0.5}}{D t_{fr}^{*}} = \frac{\pi \cdot D_m^2 \cdot v_{\mathrm{rel}}}{6 \cdot t_{Fr}^{*}} \cdot \left(\rho_f \cdot \rho_m\right)^{0.5} \tag{5-18}$$

with relative velocity as the difference of the melt fragment velocity and the velocity of the fluid (cold and hot fluid):

$$v_{\mathrm{rel}} = \left| v_f - v_m \right| \tag{5-19}$$

with average density of the representative fluid

$$\rho_{\mathrm{f}} = \frac{\alpha_{\mathrm{h}} \rho_{\mathrm{h}} + \alpha_{\mathrm{c}} \rho_{\mathrm{c}} + \alpha_{\mathrm{d}} \rho_{\mathrm{d}}}{\alpha_{\mathrm{h}} + \alpha_{\mathrm{c}} + \alpha_{\mathrm{d}}} \tag{5-20}$$

The fragmentation rate does not depend on the history but only on instantaneous values. Thus, the dependence on the development of conditions is strongly accentuated.

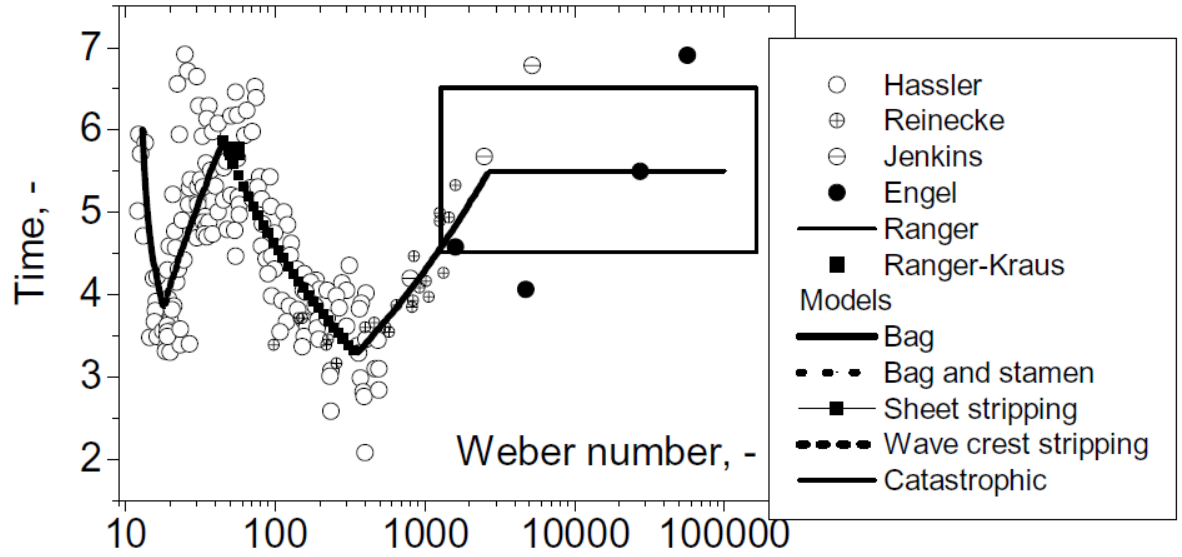

Fig. 5-1: **Total breakup time as a function of Weber number for gas-liquid systems. The summary was prepared by Pilch [78]. Extracted from Kolev [80].**

Table 5-1: **Constants for breakup modes, according to Kolev [80].**

c	m	We_d	Mode
7	0	1 – 12	Vibration mode
6	-0.25	12 – 18	Bag breakup
2.45	+0.25	18 – 45	Bag – and stamen breakup
14.1	-0.25	45 - 351	Sheet stripping
0.77	+0.25	351 - 2670	Wave crest stripping followed by catastrophic breakup
5.5	0	2670 - ∞	

The correlation Eq. 5-18 is also used in MC3D [34,35], CULDESAC [81], ESPROSE.m [32,33] , IFCI [27,28], TEXAS [29,30] and IDEMO [42].

Considering the amount of melt prone to fine fragmentation indicated in Section 5.3, the total mass transfer rate per volume Γ_{Fr} is expressed using Eq. 5-18 by

$$\Gamma_{Fr} = N_{fr} \cdot \xi_{Fr} \cdot \frac{\mathrm{d}\, m_{Fr}}{\mathrm{d}\, t} = \frac{6 \cdot \alpha_m}{\pi \cdot D_m^3} \cdot \xi_{Fr} \cdot \frac{\mathrm{d}\, m_{Fr}}{\mathrm{d}\, t} = \xi_{Fr} \cdot \frac{\alpha_m \cdot v_{\mathrm{rel}}}{t_{Fr}^* \cdot D_m} \cdot \sqrt{\rho_f \cdot \rho_m} \tag{5-21}$$

with N_{fr} for the total number of melt drops able to fine fragmentation, α_m for volume fraction of melt, D_m for drop diameter, ρ_m for melt density, v_{rel} for relative velocity of melt drops, t_{fr}^* dimensionless fragmentation time and ξ_{fr} for fraction of melt able to fine fragmentation.

The entrainment rate Γ_E is taken proportional to the fragmentation rate Γ_{Fr} on a volume basis:

$$\Gamma_E = f_E \cdot \Gamma_{Fr} \cdot \frac{\rho_c}{\rho_m} \tag{5-22}$$

where f_E is a parametrical entrainment factor. To fix this parameter, the cloud volume rate is calculated assuming a certain fragmentation volume. Based on experimental observations the entrainment factor is considered in IDEMO-3D calculations as $f_E = 7$.

Based on the micro-interactions concept, the heat from hot debris during the fine fragmentation is transferred only to the hot coolant phase. The heat transfer rate in Eqs. 5-9 and 5-11 is given by

$$Q_{dh} = h_{dh} \cdot \left(T_d - T_h\right) \cdot \frac{6\alpha_d}{D_d} \tag{5-23}$$

where D_d is the diameter of the debris fragment, T_d and T_h are the temperatures of the debris and hot coolant, respectively. α_d is the volume fraction of debris. The fragment diameter D_d and heat transfer coefficient h_{dh} are chosen parametrically. The fragment size and heat transfer coefficient are chosen as $D_d = 50 \mu m$ and $h_{dh} = 10^4$ to $10^6\, W/\left(m^2 K\right)$, respectively.

The interfacial momentum exchange between the melt droplets and the fluid is given by

$$\vec{F}_{m,f}^{\,D} = \frac{3 \cdot \alpha_m \cdot \rho_f \cdot c_{f,m}^D}{4 D_m} \cdot \left|\vec{v}_f - \vec{v}_m\right| \left(\vec{v}_f - \vec{v}_m\right) \tag{5-24}$$

with a fixed drag coefficient $c_{f,m}^D = 2.5$.

5.3 Discretization into crust thickness

The crust thickness at the surface of melt droplets is considered to be the main limiting criterion to fine fragmentation, see also Chapter 4. During the premixing, melt drops coming from the jet fragmentation and moving the coolant have various age, history and crust thickness. The ability of a melt drop to breakup depends on the relative velocity, fluid density and actual crust thickness. Crusts on melt drops can strongly limit or even prevent rapid fine fragmentation affecting pressure escalations in fuel coolant interactions lowering the strength of steam explosions. In order to treat different fragmentation behavior of differently crusted melt droplets, the MUSIG (Multiple Size Group) approach is used in the IDEMO-3D for partition of melt droplets into crust thickness groups, or bins. Thus, the population equation including all groups is given by

$$\frac{\partial}{\partial t} n\left(\delta^*, \vec{x}, t\right) + \nabla \cdot \left(n\left(\delta^*, \vec{x}, t\right) \cdot \vec{v}_m\right) = G\left(\delta^*, \vec{x}, t\right), \tag{5-25}$$

with n as number density of drops with relative crust thickness δ^*, spatial location in the coordinate system $\vec{x}$ and melt drop velocity $\vec{v}_m$. The number density of size group j can be expressed by:

$$N_j = \int_{\delta^*_{j-1/2}}^{\delta^*_{j+1/2}} n(\delta^*, \vec{x}, t)\, d\delta^* . \tag{5-26}$$

In order to guarantee the compatibility of the applied MUSIG approach with Eulerian description for melt phase used in IDEMO-3D, additional conservation equations must be defined:

$$\frac{\partial}{\partial t} N_j + \nabla \cdot \left(N_j \cdot \vec{v}_m\right) = G_j, \quad \textit{with } j = 0 \ldots M_\delta - 1, \tag{5-27}$$

$$\frac{\partial}{\partial t} \xi_{Fr} \cdot \alpha_m \cdot \rho_m + \nabla \cdot \left(\xi_{Fr} \cdot \alpha_m \cdot \vec{v}_m\right) = -\Gamma_{Fr} + G_0 \rho_m \frac{\pi D_m^3}{6}, \tag{5-28}$$

with N_j for the number density of size group *j*, α_m for volume fraction of melt, ρ_m for melt density and ξ_{fr} for fraction of melt able to fine fragmentation. Initial values are taken from Lagrangian description for drops in JEMI (premixing stage). Fig. 5-2 shows exemplary an initial cumulative crust distribution partitioned into groups with different crust thickness.

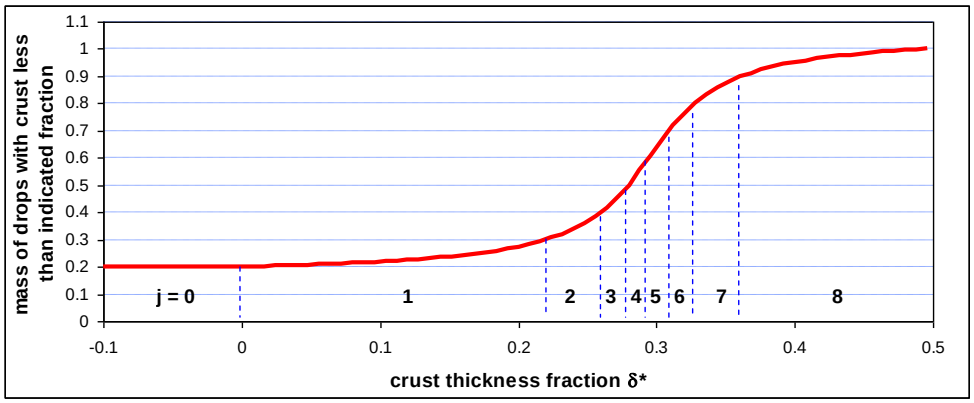

Fig. 5-2: **Initial cumulative crust distribution imported from JEMI and partitioned into crust thickness groups**

Connecting the number density of each crust thickness group Eq. 5-26 and the criterion for fine fragmentation of crusted melt drops Eq. 5-39, the instantaneous number of fragmenting drops (i.e. sum of drops with relative crust thickness below critical value) can be expressed by

$$N_{Fr} = \sum_{j=0}^{k} N_j + N_{k+1} \cdot \frac{\delta^*_{cr} - \delta^*_{k+1/2}}{\delta^*_{k+3/2} - \delta^*_{k+1/2}}, \quad k = \max_i \left(\delta^*_{i+1/2} < \delta^*_{cr}\right) \tag{5-29}$$

Once the relative crust thickness is below critical value and the drop has started fragmenting, it is assumed that the crust is removed and the drop is moved to group $j = 0$:

$$G_j = -\frac{N_j}{\Delta t}, \quad j = 1 \ldots k, \quad k = \max_i \left(\delta^*_{i+1/2} < \delta^*_{cr}\right)$$
$$G_0 = -\sum_{j=1}^{k} G_j \tag{5-30}$$

The sufficiently solidified melt drops, i.e. with sufficiently thick crust, are not considered in the thermal interaction between melt and coolant, but only in the momentum equation.

5.4 Fine fragmentation criterion

As already discussed, a significant growth of crusts on the melt drops during the premixing stage can strongly inhibit or even prevent rapid fine fragmentation of melt drops and thus pressure escalations in fuel coolant interactions. This effect of solid crusts has been investigated by several authors. Bürger et al. [11] investigated the crust stability criterion in experiments with the Wood's metal in water streams by varying the water sub-cooling, the drop diameter and the shear flow velocity as trigger for fine fragmentation. In this investigation, a strong limitation in breakup of

crusts has been observed above crust thicknesses of 130 µm. In other experiments to drop fragmentation performed by Nelson et al. [12] with iron oxide in water, an explosion could be induced in a partially solidified 2.9 mm-diameter drop with crust thickness up to 200 µm, even after it had frozen inward to about 10 percent of its radius. For corium, such experimental studies are not available.

Various models are proposed for breakup analyses of a crusted melt drop in relative flows based on different breakup mechanisms. These are deformation [47,79], Taylor instabilities [83] and shear flow instabilities, which are theoretically investigated with FRADEMO by Bürger et al. [84]. Concluding the made observations in [11], the breakup mechanism due to shear flow instabilities is assumed to be the most effective, since it yields much smaller relative velocities required for the breakup.

Deriving from the Kelvin-Helmholtz model presented by Bürger et al. [51] for jet breakup, the wave growth by shear flow instabilities is expressed by

$$\eta = \eta_0 \cdot e^{kC_i t} \tag{5-31}$$

with k as wave number and C_i as imaginary part of the phase velocity expressed by

$$C_i = \frac{1}{\sqrt{3}} \sqrt{\frac{\rho_f}{\rho_m}} \cdot u_a \tag{5-32}$$

The ambient velocity u_a is considered as

$$u_a = f_{fl} \cdot v_f \tag{5-33}$$

The parameter f_{fl} (similar to discussion of jet breakup in Chapter 4.4) implicates the velocity profile of surrounding flow (with a velocity v_f) at the drop. The factor f_{fl} reduces the impact of the relative velocity on the drop and thus must be smaller than one. In a simplified approach, the wavelength for the stripping amplitude can be expressed by

$$\lambda = \frac{3\pi\sigma}{\rho_f u_a^2} = \frac{3\pi\sigma}{\rho_f \left(f_{fl} v_f\right)^2} \tag{5-32}$$

Once the solid crust develops at the surface of a melt drop, the crust elasticity replaces the surface tension as stabilizing force. To cover the effect of a thin solid layer at the drop surface on its ability to fine fragmentation, the mechanical properties of the solid layer are considered to be the stability criterion, in addition to the relative flow. The crust properties determine whether the crust can stand the hydrodynamic forces induced by the relative flow of surrounding fluid. Since the crust thickness is significantly lower than the drop size, the elasticity approximation for a thin plate can be used to assess the stability of the crust under mechanical loads. According to the elasticity theory, the stiffness of a thin plate representing the crust at the drop surface is given by

$$N = \frac{E \cdot \delta^3}{12\left(1-\varepsilon^2\right)} \tag{5-35}$$

where E is the Young elastic modulus and ε is the Poisson's ratio for the frozen layer with a thickness of δ. The surface tension in Eq. 5-34 can be replaced using the crust stiffness *N* and the effective surface *A*:

$$\sigma = \frac{N}{A} \tag{5-36}$$

Considering the assumption of a thin plate under mechanical loads (caused by the relative fluid flow), the effective surface area is given by $A = \pi d_p / 4$.

According to [82], the smaller the wavelength the smaller the crust thickness required to suppress the fine fragmentation. The maximum possible crust thickness δ required for drop stability is obtained by setting the wavelength to drop diameter $\lambda = d_p$.

In order to consider the density effect of the melt, the effective fluid density is set to

$$\rho_f^* = \frac{\rho_f}{1+\frac{\rho_f}{\rho_m}} \tag{5-37}$$

Substituting Eqs. 5-35, 5-36 and 5-37 into Eq. 5-34 with the assumption $\lambda = d_p$, we get for the critical crust thickness:

$$\delta < \delta_{cr} = \left(\frac{\rho_f \rho_m}{\rho_m + \rho_f} \cdot \frac{f_{\mathrm{fl}}^2 v_{\mathrm{rel}}^2 \cdot d_p^3 (1-\varepsilon^2)}{E} \right)^{\frac{1}{3}} \tag{5-38}$$

where ρ_f and ρ_m is the fluid and melt densities, v_{rel} is the relative velocity between fluid and melt drop, f_{fl} is the velocity profile factor, d_p is the drop diameter, E is the Young modulus and δ_{cr} is the absolute value of the critical crust thickness. The latter embodies the thickest crust that can be broken up. The relative crust thickness can be then expressed by:

$$\delta^* < \frac{\delta_{cr}}{d_p} = \left(\frac{\rho_f \rho_m}{\rho_m + \rho_f} \cdot \frac{f_{\mathrm{fl}}^2 v_{\mathrm{rel}}^2 \cdot (1-\varepsilon^2)}{E} \right)^{\frac{1}{3}} \tag{5-37}$$

If the actual crust thickness is lower than the critical value in Eq. 5-38, the crust breaks up under mechanical loads and the melt drop fragments finer. Crusts above the critical value are assumed to be stable preventing the fine fragmentation. Based on experimental results, the profile factor on relative velocity has an empirical value $f_{fl} = 0.5$. This value corresponds to the profile factor in jet breakup modeling. The chosen value of *0.5* also correlates with the approach based on the modified Weber number presented by Ursic et al. [87].

The consideration of the crust effect on fine fragmentation and thus on the strength of steam explosion is an essential step done in the coupling JEMI – IDEMO-3D in contrast to IKEJET/IKEMIX – IDEMO, where crust formation is not considered and only the energetic criterion is taken into account.

5.5 Numerical procedure

In IDEMO-3D, similar to IDEMO, the explicit Euler method is used for the temporal discretization of the conservation equations. A fully explicit method was found to be advantageous for propagation calculations, since the adequate resolution of shock front propagation would require time steps in the order of the stability limit for explicit methods even with semi-implicit methods. For the discretization of the spatial derivatives a finite-volume scheme is used. It is based on the robust Lax-Friedrichs – scheme, which has been augmented with spatially second order corrections to reduce numerical diffusion while maintaining Total Variation Diminishing (TVD) properties.

6 Verification of JEMI and IDEMO-3D

This chapter addresses the verification and validation of the extended program codes JEMI for premixing and IDEMO-3D for detonation to important experiments. The aim of the verification is to show the ability of the 3D codes to correctly describe the key mechanisms determining the explosiveness of a particular configuration. These are:

- Melt jet fragmentation and yielded fragment size,
- Vaporization, buildup of void and pressurization,
- Reduction of melt mass available for fine fragmentation due to solidification during the premixing,
- Pressure escalations during the detonation.

The validation of the premixing model JEMI is based on FARO experiments [44]. The main purpose of this investigation is to check the ability to describe the key features affecting the explosiveness of the given pre-mixture. The experimental initial data (i.e. the initial melt temperature, melt jet diameter, water sub-cooling temperature and water pool height) is used as input for the calculation with the premixing code JEMI.

The validation of the explosion model IDEMO-3D is based on KROTOS experiments performed in ISPRA [21]. The aim was to obtain accurate results for the detonation phase. The input data is based on the premixing calculation made with JEMI. The use of the JEMI data as input provides a good basis for checking the applicability of both codes to perform reliable results in a chain. This is required particularly for using the codes in real reactor applications, for which no experiments are possible on that large scale.

It should be remarked, that FARO and KROTOS experiments have been performed in facilities with a cylindrical vessel and central melt outflow from the furnace into water. Thus, these experiments have a pronouncedly two-dimensional character. Since there are no three-dimensional FCI experiments existing, the FARO and KROTOS experiments should be applied to verify and validate the program codes. The focus should rather lay on covering the key mechanisms of the fuel-coolant interactions. The three-dimensional capability of the 3D premixing and detonation codes is discussed in Chapter 7 based on investigations to reactor scenarios.

6.1 Verification of the premixing model JEMI

The verification of the premixing model JEMI is based on the experimental results performed in the FARO experimental facility at the Joint Research Centre (JRC) in Ispra, Italy [44]. The FARO experiments present a relocation of prototypic melt compositions by gravity from a furnace into a vessel filled with water. The focus was on fragmentation of melt jets during the contact with water, the interaction of melt fragments with water by strong steam production and pressurization of the vessel as well as the quenching of the fragmented melt. The FARO experiments have been selected for the calculations on JEMI validation, since they are purely premixing tests without triggering. Here, relatively detailed results exist from the experiments: the length of coherent jet, the yielded fragment size and the amount of steam produced during the interaction of melt and water. This allows a critical check of the main aspects of the modeling and an assessment of general applicability to reactor configurations. Compared to other experiments with prototypic melts without triggering, e.g. KROTOS tests without triggering, FARO shows several advantages.

- Firstly, FARO facility has a large pressure vessel (vessel size of 0.7 m in diameter). This allows covering the radial mixture extent without strong constraining effects, which have an impact on the void buildup and drop solidification.
- Secondly, FARO tests provide a large mass of melt and a long melt outflow with fully developed melt jets excluding the influence of initial disturbances at the furnace outlet (between 100 and 175 kg total mass of melt in the furnace).
- Lastly, several FARO tests show strong steam production and pressurization of the test vessel. This allows a good assessment of the amount of steam produced during the premixing (e.g. L-28 with saturated conditions and melt pouring during ~5 s with pressure rise from 0.5 MPa to 1.6 MPa).

The FARO experiments have been performed over a significant band width of relevant conditions, system pressures from 0.2 MPa to 5 MPa, thickness of melt jets of 5 cm and 10 cm, water depths of 1 - 2 m, saturated and highly sub-cooled water. Table 6-1 from Magallon [45] gives an overview to the experimental conditions and results. Significant breakup has been obtained in all tests. The mass-mean particle size from the loose debris parts are also given in the table. In view of the large variation of conditions, the band width of particle size distributions shown in Fig. 6-1 is rather narrow. The L-33 must be excluded from the analysis of the premixing since a steam explosion was triggered producing a part of smaller particles.

Table 6-1: FARO LWR Test Series: Main experimental conditions and debris data

Test	L-06	L-08	L-11	L-14	L-19	L-20	L-24	L-27	L-28	L-29	L-31	L-33
Experimental conditions												
Corium composition[1]	A	A	B	A	A	A	A	A	A	A	A	A
Melt mass[2] (kg)	18	44	151	125	157	96	177	117	175	39	92	100[3]
Melt temperature (K)	2923	3023	2823	3123	3073	3173	3023	3023	3052	3070	2990	3070
Melt release diameter (mm)[4]	100	100	100	100	100	100	100	100	50	50	50	50
Melt fall height in gas (m)	1.83	1.53	1.09	1.04	1.99	1.12	1.07	0.73	0.89	0.74	0.77	0.77
System pressure (MPa)	5	5.8	5	5	5	2	0.5	0.5	0.5	0.2	0.2	0.4
Gas phase	Steam/Ar	Steam/Ar	Steam/Ar	Steam/Ar	Steam[5]	Steam[5]	Steam[5]	Steam[5]	Steam[5]	Argon	Argon	Argon
Water depth (m)	0.87	1.00	2.00	2.05	1.10	1.97	2.02	1.47	1.44	1.48	1.45	1.60
Water temperature (K)	539	536	535	537	536	486	425	424	424	297	291	293
Water subcooling (K)	0	12	2	0	1	0	0	1	1	97	104	124
Water Mass (kg)	120	255	608	623	330	660	719	536	517	492	481	625
Debris bed data[6]												
Hard debris, cake (kg, %)	6, 33	14, 32	0, 0	20, 16	77, 49	21, 22	27, 16	26, 23	77, 48	39, 100	0, 0	8, 8
Loose debris (kg, %)	12, 67	30, 68	146, 100	105, 84	80, 51	73, 78	141, 84	70, 77	84, 52	0, 0	83, 100	89, 92
Mean loose debris size (mm)	4.5	3.8	3.5	4.8	3.7	4.4	2.6	Na[7]	3.0	-	3.4	2.6[8]

[1] A: 80w%UO_2 – 20w%ZrO_2, B: 77w%UO_2 – 19w%ZrO_2 – 4w%Zr
[2] Total mass which interacted with water
[3] ~25 kg in ^{water} at time of trigger
[4] Diameter of the orifice. In general a crust ~3 mm thick forms during melt release
[5] >95w%steam; <5w%argon
[6] Refers to debris found in the debris catcher
[7] Not available
[8] Steam explosion after ~25 kg of melt had penetrated in water

6.1.1 Verification of jet breakup model based on FARO tests

At first, verification and validation evaluations of the breakup model in JEMI have been done in a separate treatment. The aim of this was to check the ability to predict the length of the coherent jet and the resulting particle size from the premixing. The feedback with surrounding mixture states is not included in this separate consideration. However, no large effect of surroundings on the jet breakup is expected since the jet fragmentation modeling is considered due to an upward vapor flow along the jet driven by hydrostatic head of sideways water. It is assumed, that sufficient water is always available away from the jet. Thus, the impact of possible high vapor content within the mixture remains small due to very large difference in density of water and vapor. Table 6-2 gives the summary of evaluations on the breakup length and the fragment sizes for the experiments shown in Table 6-1, considered as most relevant. According the formulation for the stripping process in Chapter 4.3 (Eqs. 4-46 and 4-50), the model parameters has been chosen as follows: $f_{fl} = 0.5$, $f_d = 0.2$, $f_F = 0.25$ and $f_B = 0.7$.

The FARO tests L-06 and L-08 have been omitted as first tests with smaller melt masses. For FARO L-27, no debris size evaluation is available. The L-29 test was probably a failure. FARO L-33 was performed with triggering and cannot be taken into account for premixing analyses. In Table 6-2, the melt inflow velocities $\vec{v}_w$ and jet diameters D_w are given at the water surface as the start of penetration into water. The inflow velocities and the jet thickness are estimated using the experimental data at the outlet nozzle and the known height for falling in gas (distance from the nozzle to the water surface). The investigation shows a trend to slightly smaller particle sizes in the calculations at higher system pressures. The experimental mean values are between 2.6 and 4.8 mm, the calculated ones between 2.0 and 2.4 mm. Smaller drop sizes in the calculations (compared to the experiments) can be explained due to higher densities of vapor at higher pressures. In the modeling, the resulting fragment size is inversely proportional to vapor density, see Eq. 4-43 in Chapter 4.4. The vapor density is taken according to the system pressure. In contrast, at lower pressures of 0.2 - 0.5 MPa, a good agreement could be achieved. The drop size range is experimentally between 2.6 and 3.4 mm, theoretically between 2.3 and 3.6 mm. Further, the resulted large deviations in fragment size from FARO tests L-14 and L-24 (5 MPa and 0.2 MPa), here D=4.8 mm from L-14 and D=2.6 mm from L-24, can be hardly explained. Possible explanation for such deviations might be specific, but not detected, effects due to high system pressure in the experiment.

Considering the resulted discrepancies between the experimental and theoretical results, the present status of modeling of the jet breakup used in JEMI is considered despite deviations at high pressures as satisfying for prediction of the fragment size from the jet breakup and can be used in JEMI.

Very high pressures (p > 5 bar) are not expected in reactor scenarios with steam explosions, since a depressurization of the RPV and primary cooling system are to be either actuated automatically by reactor protection or resulted from the initiating event which causes the core meltdown. For low pressure (p < 5 bar), the breakup model shows a good agreement with the experiments. Due to the coupling of the present breakup model with the mixing model, slight mixture effects are expected in the full JEMI description, e.g. decrease of water-steam-mixture density and the water level rise leading to weaker fragmentation. However, such effects are considered as limited due to strong feedback between fragmentation and steam production/evaporation, see discussion above. This means that a decrease of the density and the hydrostatic head of the mixture weaken the fragmentation. The consequence of the weaker fragmentation is larger melt fragments and smaller volume fraction of fragmented melt inside the mixing zone. This leads to less steam production and more water in mixture increasing the mixture density. The increase of the density intensifies the fragmentation; stronger fragmentation results in more steam production and in a decrease of the mixture density, again.

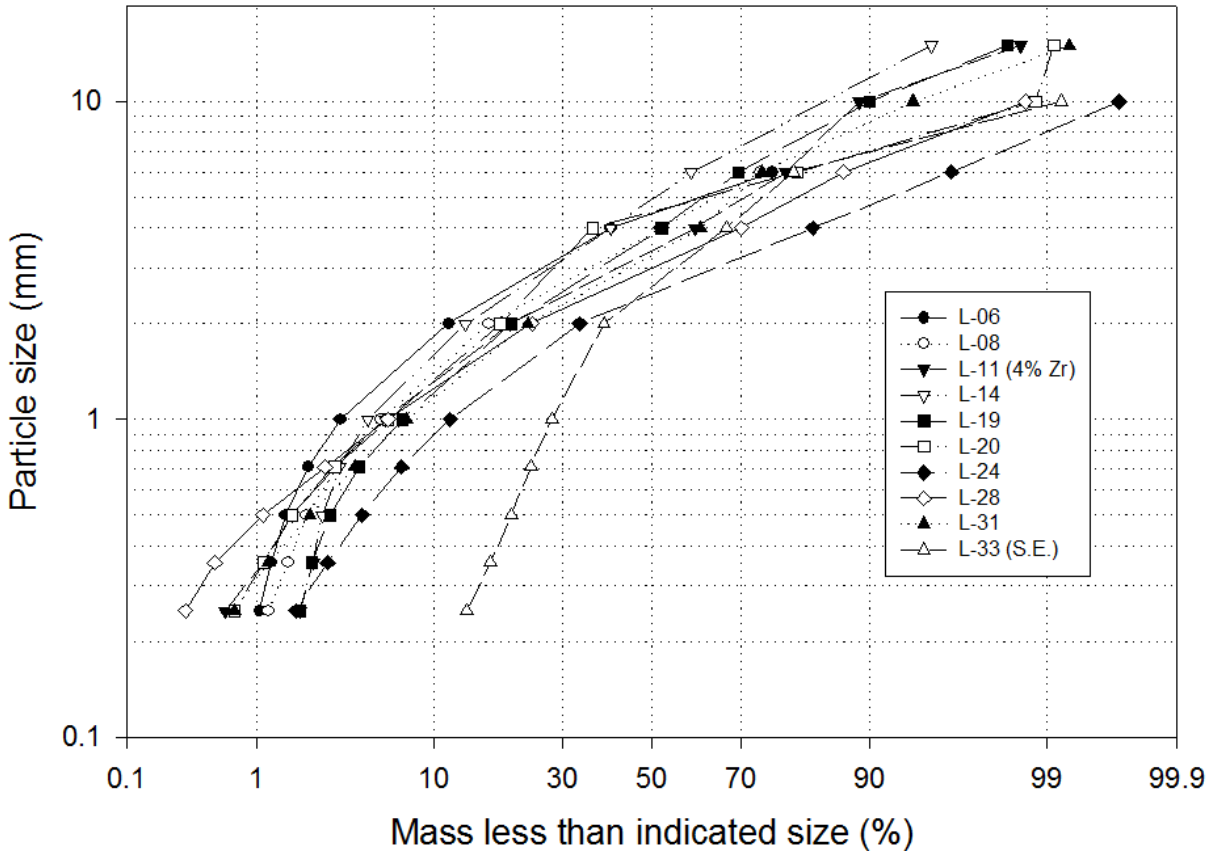

Fig. 6-1: Particle size distributions in FARO tests.

Table 6-2: Summary of jet breakup results from FARO tests and theoretical results performed by separate jet breakup model implemented in JEMI.

	P_{sys} bar	v_w m/s	D_w cm	L_w cm	L_{exp} cm	D_{exp} mm	L_{model} *cm*	D_{model} *mm*	$cake_{exp}$ %
FARO									
L-11	50	5.5	7.4	200	110	3.5	*178*	*2.0*	0
L-14	50	5.4	7.4	205	110	4.8	*176*	*2.0*	16
L-19	50	6.9	6.6	110	110	3.7	*200*	*2.0*	49
L-20	20	5.6	7.3	197	110	4.4	*167*	*2.7*	22
L-24	5	5.5	7.4	202	110	2.6	*140*	*3.5*	16
L-27	-	-	-	-	-	-	-	-	-
L-28	5	5.2	3.8	144	70	3.0	*90*	*3.6*	48
L-31	2	4.9	3.9	145	70	3.4	*80*	*3.8*	0

P_{sys}	system pressure in experiment	d_{exp}	mean particle diameter from experiment
v_w	jet velocity at water entrance	L_{model}	coherent jet length calculated by the model
D_w	jet diameter at water entrance	D_{model}	mean particle diameter calculated by the model
L_w	water pool depth	$cake_{exp}$	fraction of agglomerated cake in experiment
L_{exp}	coherent jet length estimated from exp.		

A further result concerns the length of coherent jet as breakup length from the calculations. This is important for the evaluations on particle bed formation. An incomplete jet breakup (the jet length in water is longer than the depth of the water pool) leads to a formation of a liquid melt layer on the vessel floor causing a re-melting of the fragmented melt part falling into this liquid pool and during its solidification a build of a solid cake. Also, an insufficient crust thickness at melt fragments coming from the jet breakup can cause a sticking-together, re-melting, and cake formation. Formation of hard cake is expected by

- Large particles with short falling times in water,
- Particles falling in vapor due to reduced heat exchange with the surrounding fluid (no film boiling is possible in vapor continuous flow regime; only heat radiation),
- Particles falling into a molten pool and
- Occurrence of irregularities in jet breakup leading to formation of large melt lumps.

The latter two aspects are not covered by modeling (as well as by experiments) due to high complexity and irregularity of interaction of all fluid phases and structures. In addition to this, the cooling process inside the debris bed is also not considered in the model. This can have a large impact particularly in tests with high water sub-cooling due to sufficient cooling inside debris bed inhibiting the re-melting of

fragments, which total enthalpy is above the “liquidus” point being the main indicator for the re-melting ability. The “liquidus” point corresponds to the total melt drop enthalpy at the melting temperature (“solidus”) including the heat of fusion. The debris coolability is not a part of JEMI modeling and cannot be considered in the present work.

In general, it can be concluded from Fig. 6-1 that the fragmentation process is similar in all FARO tests due to similarities in the particle size distribution found in the loose debris. Larger cake part was found in L-28, namely ~48% of the total melt mass. In contrast, L-31 yielded no cake for identical initial conditions (system pressure, water pool depth, falling height in the air), the similar jet breakup, and the equal range of particle size distribution. Only the water temperature was different: L-28 – saturated, L-31 – subcooled to 104 K. Fig. 6-2 shows the history of melt front penetration in water in relation to the time of the melt-water-contact. In Fig. 6-2, a kink appears to occur for both experiments at the same location, yielding a coherent jet length of ~70 cm. Further quicker melt penetration and earlier melt-bottom-contact in FARO L-28 (~48 s) in contrast to L-31 (~75 s) can only be explained by existence of large melt lumps coming from the jet leading edge and falling much faster in water than the smaller ones due to reduced hydrodynamic drag (larger mass by smaller effective surface). Such large melt pieces indicate irregularities in jet breakup, especially during the initial phase of the experiments, which do not reflect the jet breakup and cannot be considered by modeling. In general, the particle size distribution from loose debris is similar in L-28 and L-31; thus, the fragmentation behavior is concluded to be identical.

Furthermore, no cake is also obtained in L-11. The breakup process can be assumed to be similar in spite of the different material composition with Zirconium oxidizing under exothermic conditions. Here, the significantly lower initial melt temperatures of 2823 K may be responsible for sufficient quenching in 2 m deep water pool (further considerations are required on liquidus/solidus temperatures for the different compositions). The calculated jet length with the 10 cm diameter jet (in contrast to 5 cm with L-28 and L-31) is rather long (178 cm). The L-14, under nearly the same conditions, yields a cake of 16%, possibly due to the higher melt temperature of 3123 K. The same argument may be valid for the tests L-20 and L-24. Thus, the main conclusion is here, that complete breakup occurs in all these cases in the available water depth. However, the solidification may not always be sufficient to avoid cake parts. Analyses with this respect can only be performed with the full JEMI code including crust formation at falling drops of melt.

In view of the above considerations, it is concluded that a breakup length of about 120 cm may be assumed in the experiments with an initial jet diameter of 10 cm. And 5 cm initial diameter implies a length of about 70 cm. This corresponds to the L/D ratio of 12 and 14, respectively. These values are indicated in Table 6-2 as tentative experimental values. It can be concluded that the jet breakup model in JEMI offers an adequate description of the jet breakup.

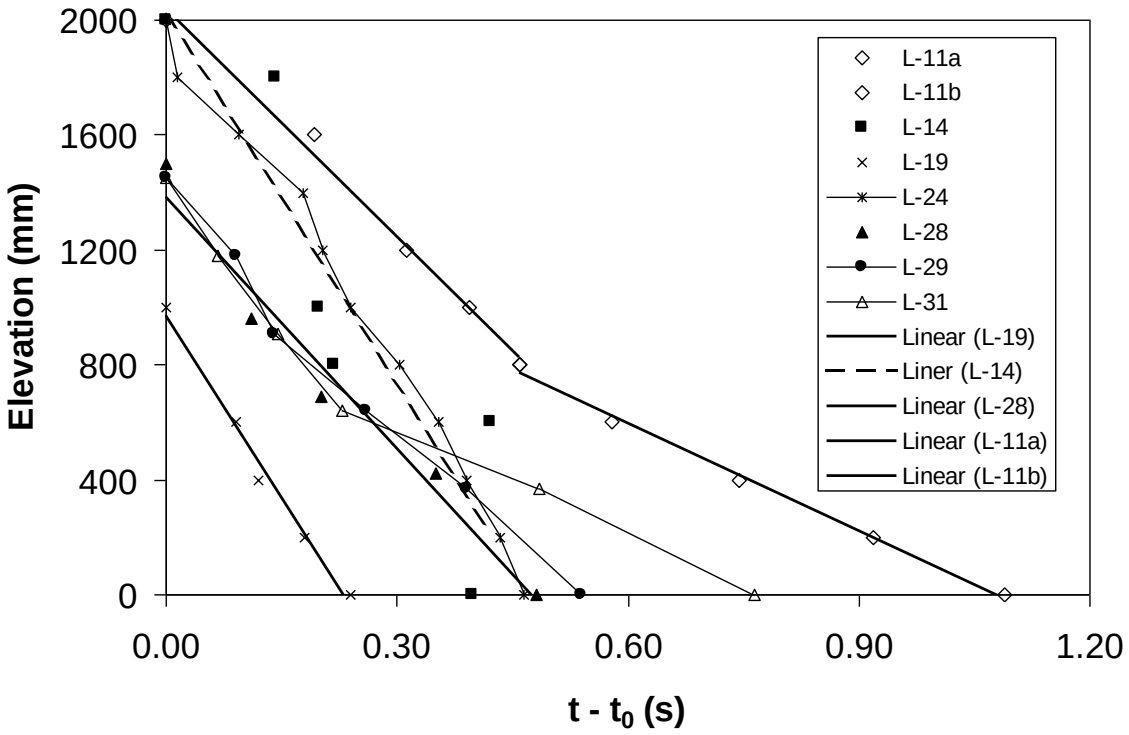

Fig. 6-2: **History of melt front penetration in water in FARO tests (t_0: time of melt front contact with water free surface)**

6.1.2 Solidification of melt drops during the premixing

Fuel coolant interaction codes generally did not consider the solidification of melt fragments during the premixing stage. The explosion experiments performed in the KROTOS facility have indicated fundamental differences in explosion behavior between stimulant alumina and oxidic corium melts, proposed in [21]. It was concluded that the energy efficiency for oxidic corium melts is significantly lower than that for the stimulant aluminum oxide (0.02 – 0.2% versus 0.87 – 2.5%). Different material properties of both melts are obviously the main reason for this contrast, as discussed by Leskovar et al. in [51]. Material properties – such as melt density, thermal conductivity, heat capacity, and liquidus/solidus temperature – play an important role for the jet fragmentation, the melt-coolant mixing, the solidification of melt, and the void buildup. The solidification, i.e. the formation of solid layer (crust) at the surface of a melt droplet falling in water-steam mixture, is believed to have a large impact on the fine fragmentation and thus on the mixture explosiveness. The existing crust inhibits or even prevents the fine fragmentation of the drop within a shock wave, so that it cannot participate on pressure escalations and would not yield on explosion strength.

Table 6-3: Material properties of corium

Material properties		*Corium (80/20)*
Liquidus specific heat capacity	*J/kg/K*	*520*
Solidus specific heat capacity	*J/kg/K*	*380*
Latent heat	*kJ/kg*	*360*
Density	*kg/m³*	*8000*
Thermal conductivity	*W/m/K*	*2.8*
Emissivity	*-*	*0.7*
Initial temperature	*K*	*3000*
Melting temperature	*K*	*2800*

While alumina melt drops from KROTOS experiments are of a large diameter ~10 mm, the resulting drops in most corium experiments are generally smaller: between 1 and 3 mm. Compared with aluminum oxide, the lower thermal conductivity of corium and the higher density yield a slower temperature compensation inside the drop (between the surface and the inner zone) leading to a steep temperature profile by corium drops, in comparison to almost flat temperature profile by aluminum oxide. This is due to higher thermal conductivity of aluminum oxide than that of corium. The lower solidification enthalpy (heat of fusion) of corium further weakens the temperature compensation within the drop. The debris size distribution from KROTOS experiments indicates a complete fine fragmentation by aluminum oxide and a partial fine fragmentation by corium [22,86]. Complete and partial solidification of melt drops during the premixing is an explanation for their explosiveness (ability to fine fragmentation and to participation in pressure escalations). Therefore, the consideration of the drop solidification is necessary for an adequate prediction of the explosion development and the resulting loads.

The validation of the solidification model (presented in Chapter 4) is based on comparison with a numerical solution of the heat equation. Following assumptions and simplifications have been met. Firstly, the solidifying droplet is assumed as a sphere. Secondly, the heat transfer inside the drop occurs only in one direction – from the inner zone to the surface. Thirdly, the drop cooling is considered steady and homogenous, i.e. one-dimensional. Lastly, the heat transfer is assumed for the water continuous regime. The latter means that the effect of steam content in the coolant is not considered in the validation: both the heat radiation and the film boiling are regarded. Two particle sizes are taken in accordance with FARO premixing results performed with corium melts: 3 mm and 5 mm. The melt is corium. The material properties and the initial conditions are listed in the Table 6-3. The initial drop temperature is 3000 K with a melting temperature of 2800 K. It yields 200 K melt superheating. The heat transfer from the melt drop to the coolant is obtained according Chapter 4.6, see Eqs. 4-60, 4-61, 4-68, and 4-70.

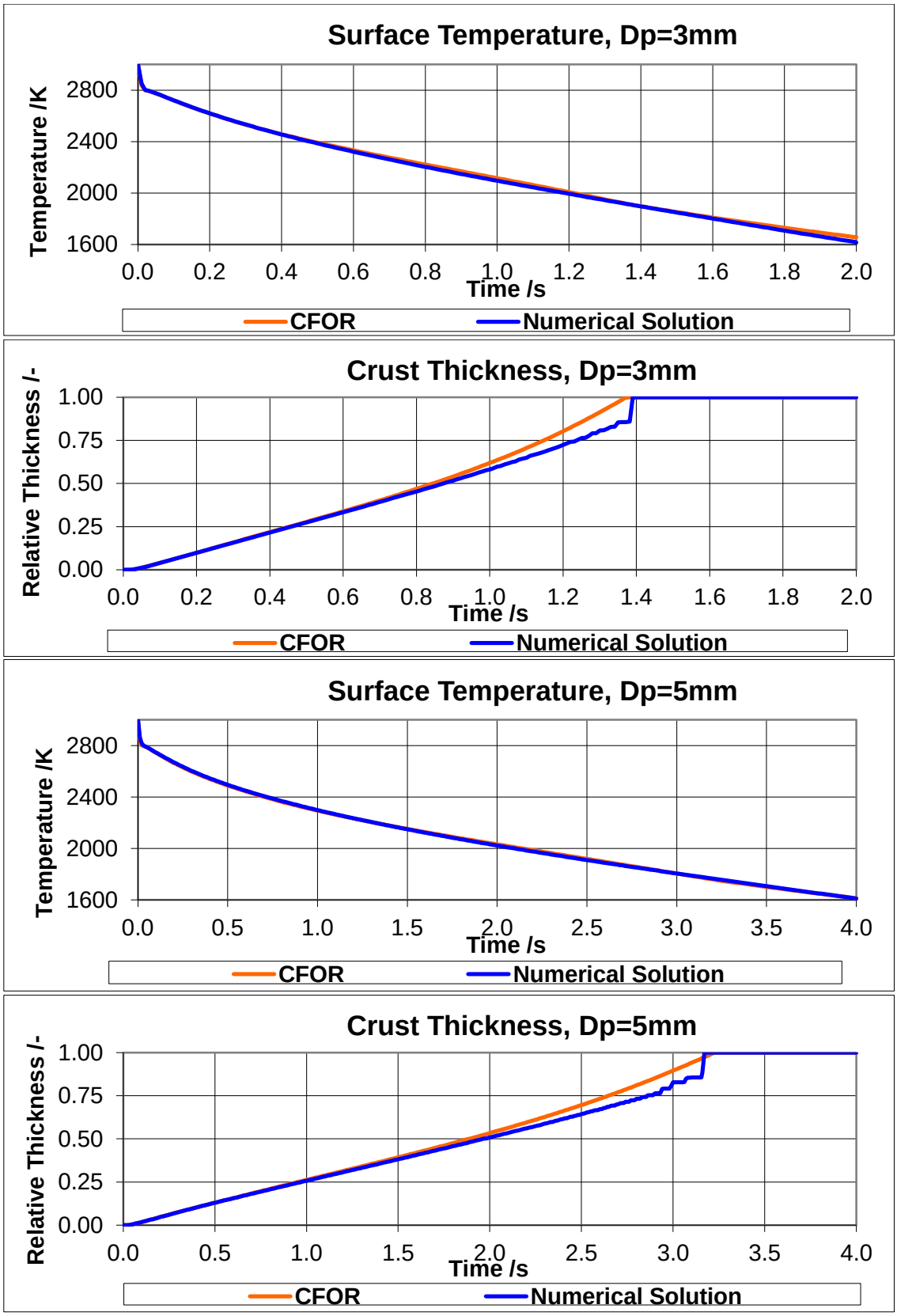

Fig. 6-3: **Comparison calculation of CFOR solidification model with the numerical solution of heat conduction equation, development of surface temperature and relative crust thickness, corium with drop size of 3 mm and 5 mm.**

Fig. 6-3 shows the development of the surface temperature and crust thickness over the time for calculations with 3 mm and 5 mm of drop diameter. The results show a good agreement between the analytical and numerical solution for both particle sizes which are considered mostly relevant (based on FARO). Deviations are not observed until ~78% of the entire drop (corresponding to 40% of radius) is already solidified.

Also, further comparison calculations have been made with another analytical solidification model HTMOD implemented in the explosion code MC3D, performed by Ursic [85,87]. Both models were compared with the numerical solution. The major difference in the modeling concerns the implementation, the numerical procedures, and the description of interfacial heat transfer from melt to coolant within the premixing codes MC3D and JEMI. The MC3D treats the droplets using the Eulerian approach, while JEMI uses the Lagrangian method (as discussed in Chapter 4.5). The comparison investigation has shown that both models adequately predict the development of the crust thickness and the surface temperature for a spherical droplet cooling down in water. It can be concluded that CFOR can be used in JEMI in order to calculate the development of the surface temperature and crust thickness for the melt fragments.

6.1.3 JEMI verification on FARO L-24, L-28 and L-31

The experiments FARO L-28 and L-31 give relatively detailed data which allows a critical check of the calculation results in a comparison. Especially, due to a long melt pouring of ~ 5 s in FARO L-28 with an initial (outlet) jet diameter of 5 cm, the establishment of clear conditions is enabled. Generally, long melt pouring of several seconds and thick melt jets (10 cm to 40 cm of jet diameter) is considered as relevant for reactor applications.

In FARO L-28, a perfectly constant increase of pressure over 5 s was obtained (after the initial phase with a stronger increase). This indicates a steady-state behavior of the mixture. This essentially means a constant rate of jet fragmentation, constant steam production, and steam release from the mixture. Thus, this experiment is especially qualified for the code validation. It provides the understanding of the key features which play a significant role for building critical mixings during the premixing phase. They are the melt breakup, the melt distribution, the mixing with water and the void in mixture. The calculations have been carried out using the full breakup model; the feedback between the jet breakup and the ambient fluid has been taken into account.

An idealized geometrical configuration has been chosen for the calculations on the FARO experiments. The calculations were performed in cylindrical coordinates. The computational domain (R = 0.35 m, H = 3 m) was discretized by 20 radial and 80 axial cells. The heights are chosen according to the experiment, while the outer annular gas space is not modeled directly. The corresponding gas volume is taken

into account by a point model linked to the overflow opening. No vapor re-condensation released from the mixing zone is considered in this point model. The initial conditions are given in Table 6-1.

The results of the jet breakup calculated by JEMI (considering the surrounding fluid) for three tests L-24, L-28 and L-31 are summarized in Table 6-4. Coherent jet length L, jet diameter at the water surface D_w, the length-diameter ratio L/D_w and the resulting drop size (sauter mean) $d_{p,SM}$ are obtained. The results have a good agreement with those in Table 6-2. Complete breakup is obtained in all cases; the calculated length of the coherent jet is 125 cm for L-24 and 75 cm for L-28 and L-31. The larger jet length in L-24 is a direct consequence of the larger initial diameter and outflow rate.

The time development of melt fraction in different void regions for L-28 is given in Fig. 6-4. The average void fraction over the total pouring duration is 45%. This corresponds to the experimentally observed steam content. Fig. 6-5 shows the calculated system pressure development in comparison with the experimental measurement. It can be seen that the pressure increases with a practically constant rate for a period of about 5 s. The major result of the evaluations performed by Bürger [64] is that the quasi-steady behavior, expressed by practically constant pressure increase for 5 s, is only consistent with a moderate void fraction. Accordingly, the experimental estimation of average void was ~40%. Fig. 6-4 shows that the major part of the melt droplets is in a relatively low void range below 50%, which is consistent with the explanation of the quasi-steady behavior. Pohlner et al. [40] had investigated the void buildup in L-28 and reproduced it by improving the formulation of the interfacial friction between steam and water in different flow regimes (see Chapter 4.2). The improved formulation is also implemented in JEMI.

The discretization for FARO L-31 is the same to FARO L-28. According Table 6-1, the total melt mass in FARO L-31 with 92 kg is lower than 172 kg in L-28. Due to the lower melt mass, the melt pouring duration is approximately 3 s, i.e. shorter than that in FARO L-28. The water sub-cooling of 103 K is associated with the initial water temperature of 294 K and the saturation temperature of 397 K for system pressure of 0.22 MPa. The calculated particle size is 3.65 mm. It shows a good agreement with the experiment; see Table 6-4 and Fig. 6-1. Also, the calculated coherent jet length of 0.8 m is very close to the value obtained in the test, Fig. 6-2. The averaged void in mixture is calculated ~30%, see Fig. 6-6. A lower void in K-31 than that in L-28 was expected due to high water sub-cooling. The calculated pressure rise of Δp=0.075 MPa is higher than that in the test, Fig. 6-7. However, the experimental pressure rise of 0.03 MPa is quite low compared to ~1.2 MPa in L-28. The difference between the experiment and calculation can be traced back to the fact that no steam re-condensation in the free volume outside the mixture is regarded by the point model. Due to high water sub-cooling, a relatively cold atmosphere, and cold walls in the test facility, the re-condensation of the produced steam could take place in some manner reducing the system pressure.

The experimental conditions for FARO L-24 can be found in Table 6-1. The L-24 test has a larger jet diameter of 10 cm. Results of the calculations for FARO L-24 are given in Fig. 6-8 for the fractional distribution of fragmented melt in different void regions and in Fig. 6-9 for the time development of the system pressure. Concerning the pressure buildup, the experimental development is approximately reproduced. A relatively strong void buildup, higher than that in L-28, is obtained with averaged void in mixture of ~62%, which is explained by locally higher concentrations of fragmented melt over long distance (i.e. longer coherent jet length of 1.25 m) due to initially thicker jet. The system pressure, as main indicator, has finally achieved in the test ~1.9 MPa with effective pressure rise of Δp=1.4 MPa. This could also be reflected in the calculations. Merely, the initial pressure peak could not be reproduced.

Table 6-4: Breakup results calculated by JEMI for the FARO experiments L-24, L-28 and L-31

	L-24	***L-28***	***L-31***
L	*1.25 m*	*0.75 m*	*0.8 m*
D_w	*0.074 m*	*0.038 m*	*0.039 m*
L/D_w	*16.9*	*19.7*	*19.2*
$d_{p,\,SM}$	*3.4 mm*	*3.4 mm*	*3.65 mm*

A comparison of the obtained particle size distributions with experimental data from FARO showed a satisfied agreement. As mentioned early, specific dependencies on experimental conditions could not yet be fully reproduced by the present modeling. Nevertheless, it can be concluded that the calculated particle sizes fall well in the experimental band width. It must be remarked that the calculated size distribution for drops lacks a resolution for very small particles, i.e. usually no particles with sizes smaller than 3 mm are calculated. With this respect, the major purpose of jet breakup modeling is firstly to yield general information of amounts of fragmented versus unfragmented melt. Secondly, it is to give indications on the dominant particle sizes. The determination of the full size range is not possible in the present modeling.

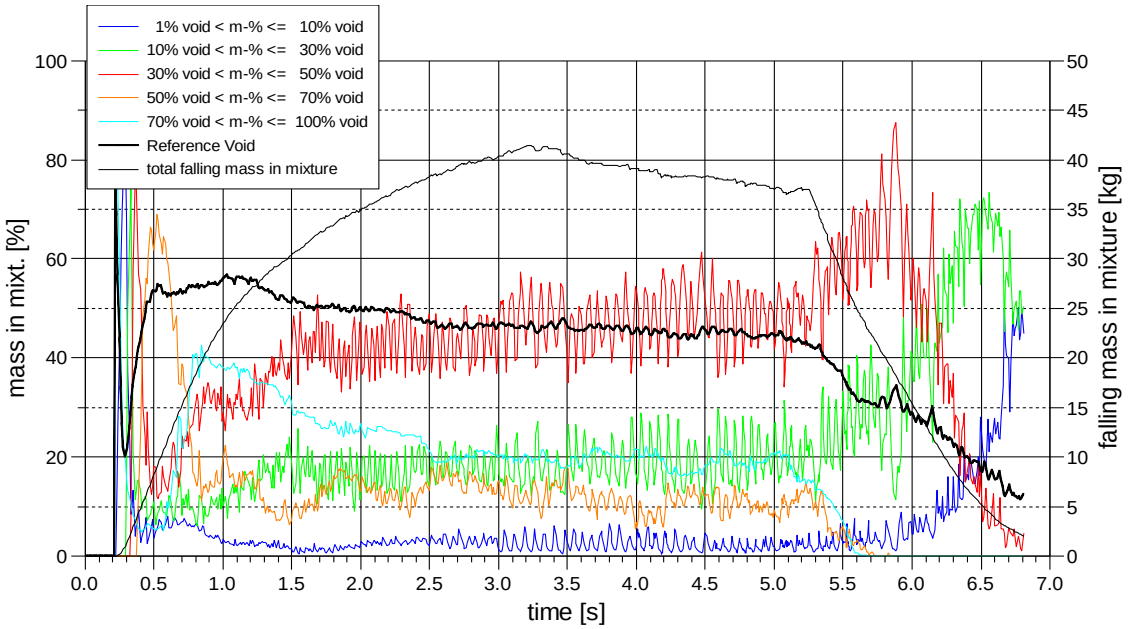

Fig. 6-4: **Distribution of fragment melt mass in mixture in different void regions calculated for the experiment FARO L-28.**

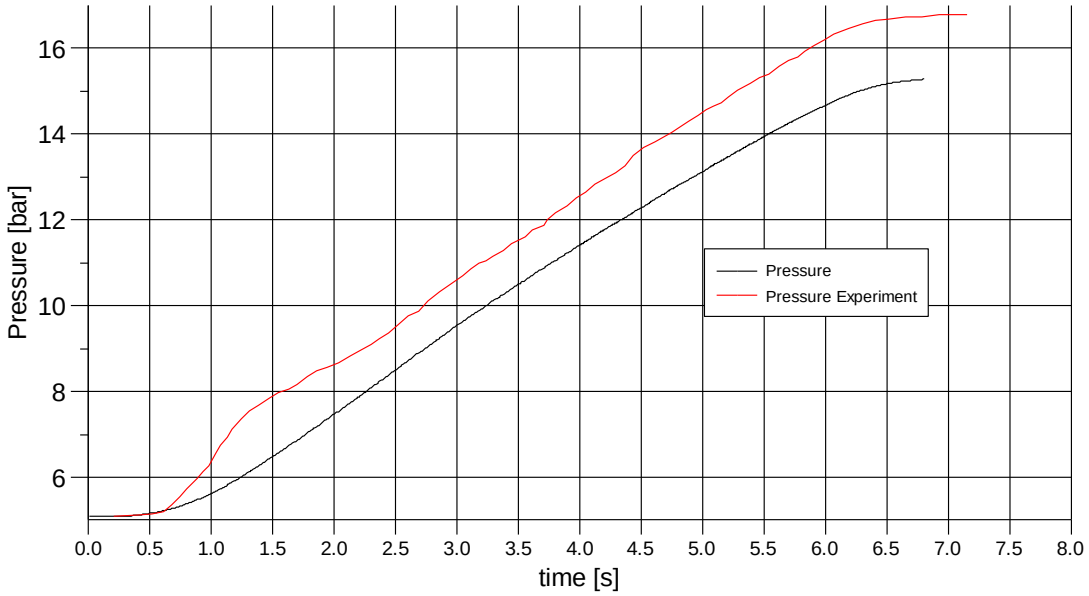

Fig. 6-5. **Calculated and measured system pressure development in the experiment FARO L-28.**

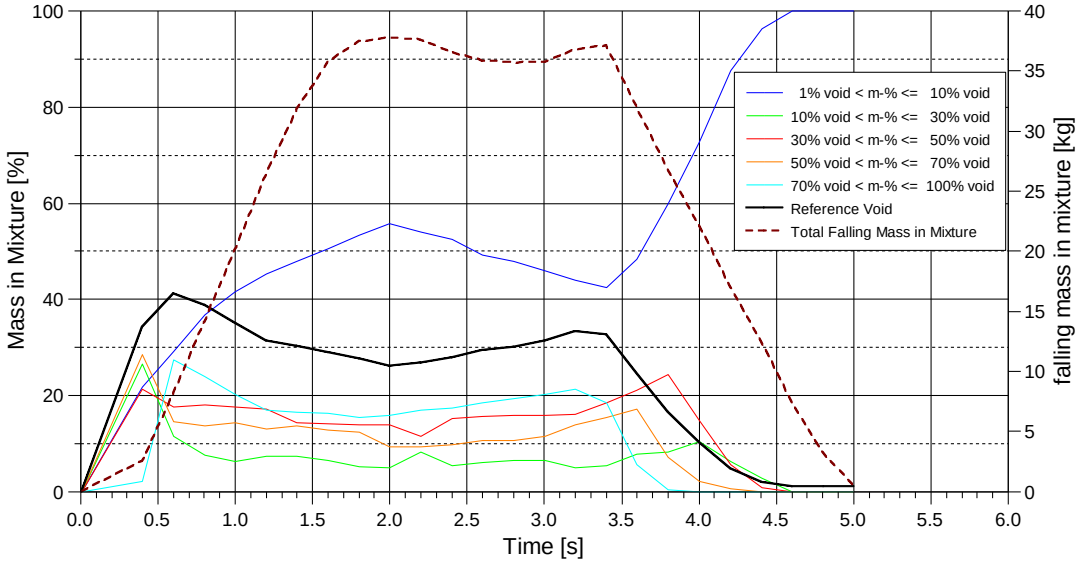

Fig. 6-6: **Distribution of fragment melt mass in mixture in different void regions calculated for the experiment FARO L-31.**

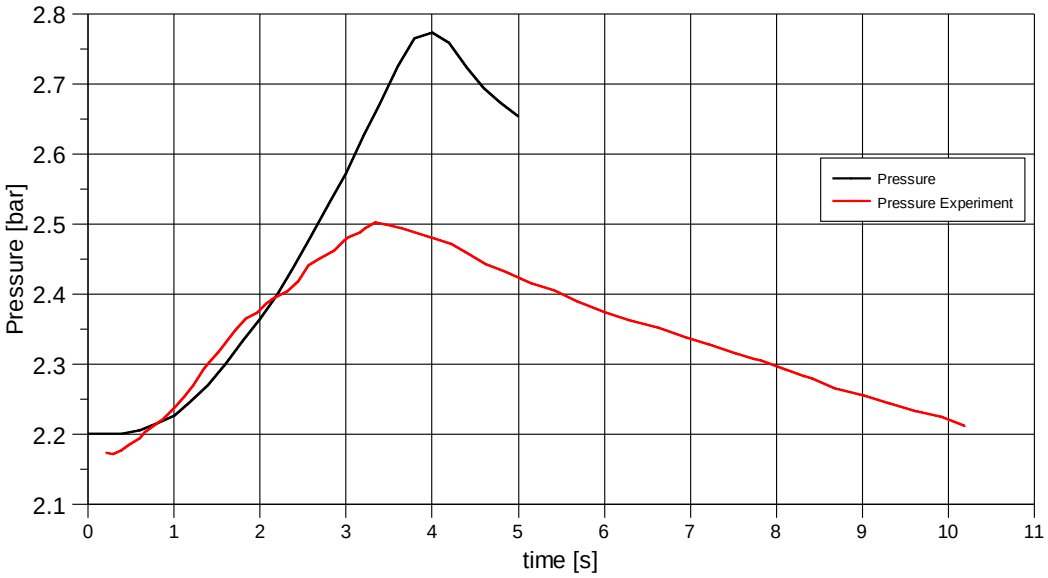

Fig. 6-7: **Calculated and measured system pressure development in the experiment FARO L-31.**

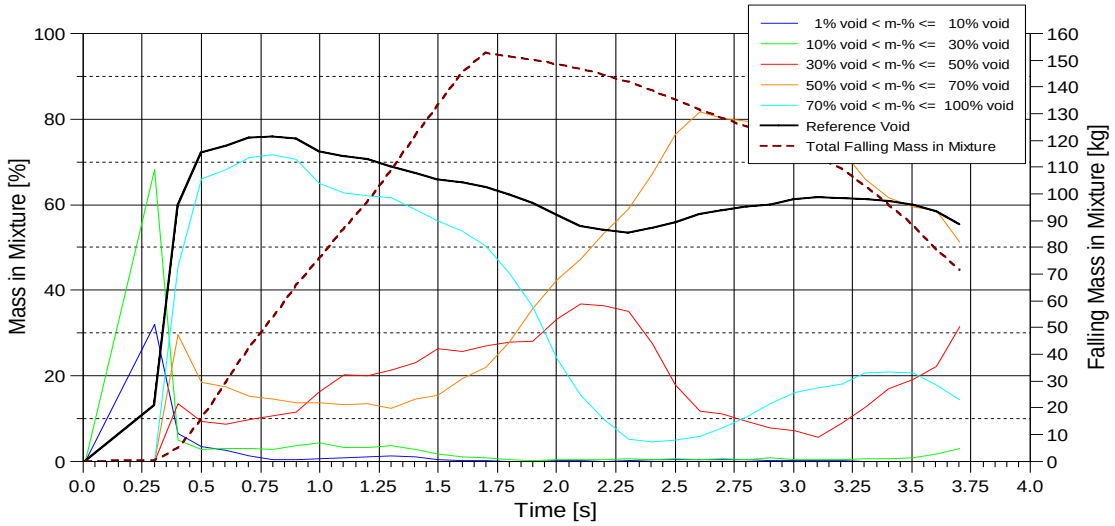

Fig. 6-8: **Distribution of fragment melt mass in mixture in different void regions calculated for the experiment FARO L-24.**

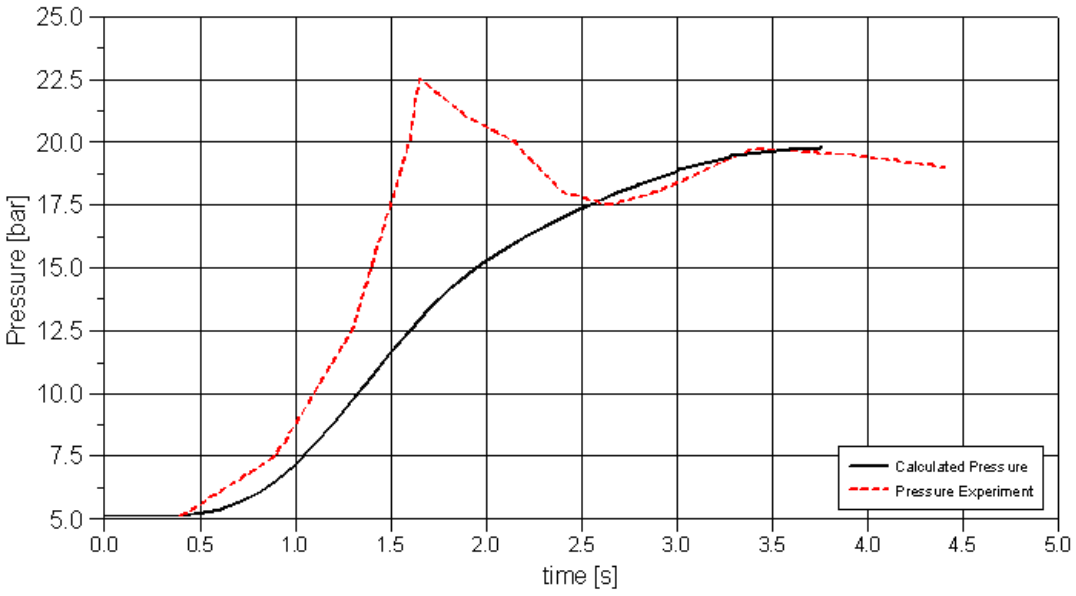

Fig. 6-9: **Calculated and measured system pressure development in the experiment FARO L-24.**

6.2 Verification of the IDEMO-3D code with explosion experiments

Another experimental program KROTOS has been implemented in order to investigate the premixing of melt and coolant, as well as progression and energetics of spontaneous and triggered fuel-coolant interactions, see for details [21,86,88]. The KROTOS facility was constructed by JRC-Ispra in 1987 with the aim to support the modeling efforts done by several research organizations addressing the steam explosion phenomena. The KROTOS tests have been performed with various simulant materials such as tin, Al_2O_3 and prototypical corium composition (80 w% UO2 + 20 w% ZrO2). These tests provide unique experimental data on steam explosions considered as essential for the model development. The KROTOS experiments are used in FCI studies as a link to the large scale FARO experiments [19]. The test section is represented in Fig. 6-10. The geometry of the facility has a distinctive 1-D character and produces an experimental data for the validations of premixing and explosion computer codes. Here, the axial jet penetration in water and breakup process should be the most important phenomenon. The radial extension of the fragmented melt plays a circumstantial role in the explosions triggered in the KROTOS facility due to very small vessel radius in relation to the height. The secondary objective of the KROTOS tests is to provide a comparison between preliminary data of aluminum oxide and corium used for melt-water interactions. The expectation was to indicate significant differences in mixing behavior and explosiveness of prototypical corium and Al_2O_3.

The alumina melts produce a coarse mixture with large fragments independently of water sub-cooling, which always results in a vapor explosion either triggered or spontaneously. Corium melts produce a mixture with relatively fine fragments. No evidence of spontaneous steam explosions were detected in the tests when corium is used. This is primarily caused by differences in jet breakup behavior between corium and alumina melts, yielding significantly smaller drops if using corium. Moreover, higher pressures have been measured with alumina melts up to 100 MPa, while the corium melts yielded rather moderate pressure escalations up to 20 MPa, see [21,86]. The experimental conclusions consider the material properties of alumina and corium melts as the reason for that discrepancy in the explosion strength. The examination of this difference is the major focus of KROTOS tests and the validation calculations in the scope of this verification part.

Three KROTOS tests are considered as suitable basis for the verification of IDEMO-3D: KROTOS K-44, K-52 and K-58. It should be remarked that IDEMO-3D presents the same modeling as its predecessor 2D code version IDEMO. In the present work, it is extended with regard to the three-dimensionality and the consideration of drop solidification during the premixing (see Chapters 4.7, 5.3 and 5.4). The chosen tests provide a detailed experimental data to explosion propagation forming a good basis for validation of the models. Here, detailed information for

important results exists, e.g. the debris size distribution and no evidence of irregularities. It is proposed to indicate main limiting factors affecting and limiting the explosion strength. The differences in the resulting loads between alumina and corium melts are to be critically discussed.

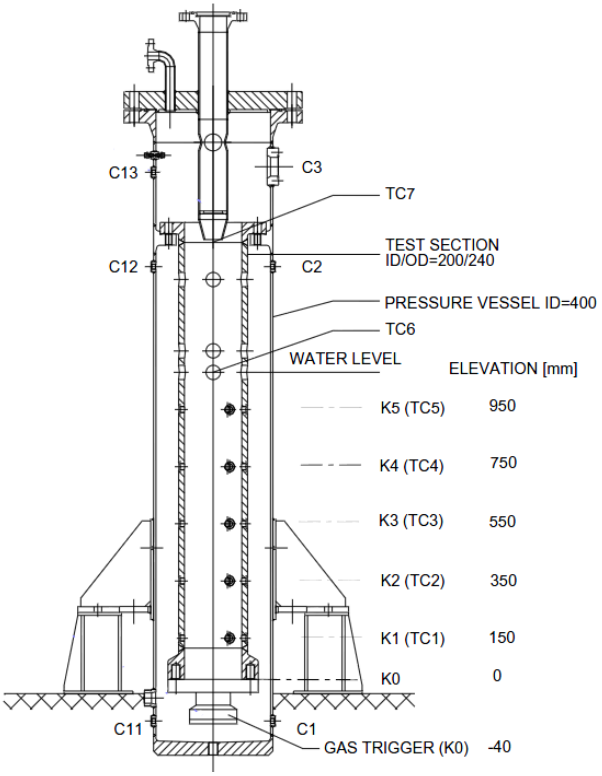

Fig. 6-10: KROTOS test facility

The initial conditions for the chosen tests are summarized in Table 6-5. While the aluminum oxide Al_2O_3 is used in K-44, the corium is used K-52 and K-58 tests. The tests with corium differ in the melt superheating 173 K and 227 K and the system pressure 0.2 MPa and 0.37 MPa. Also more melt mass is used in K-58. The experimental results are also discussed in [21,86].

Table 6-5: Initial experimental conditions

		K44	K52	K58
Melt composition		Al2O3	Corium 80-20	Corium 80-20
Melt mass	kg	1.5	2.6	3.6
Melt temperature	K	2673	3023	3077
Melt superheat	K	374	173	227
Melt jet diameter	mm	30	30	30
Fall height in gas	m	0.42	0.3	0.42
Water depth	m	0.975	1.105	0.975
Water subcooling	K	10	102	125
Initial pressure	MPa	0.1	0.2	0.37
Gas trigger pressure	MPa	15	15	15

The initial conditions for IDEMO-3D are calculated by the premixing code JEMI, presented in Chapter 4. The premixing results from JEMI are then converted into input data for IDEMO-3D. The premixing calculations can be considered as an additional examination for the premixing model in particular, since the intermediary results from the premixing phase in the KROTOS tests are not available due to triggering.

In IDEMO-3D calculations, the heat transfer coefficient has been chosen differently for Al_2O_3 and corium. The values are taken according previous investigations to KROTOS, FARO experiments performed with 2D model IDEMO; see [75-77]. Since no modification in the modeling on the physical description of the heat transfer between melt and coolant has been made in the extended model, the existing parameterization of the heat transfer ratio with respect to different materials remain unchanged. This then yields $C^{HTC}_{Al_2O_3} = 5 \cdot 10^5$ and $C^{HTC}_{\text{Corium}} = 5 \cdot 10^4$. The fuel debris size is set as $50 \mu m$ taken from debris size distribution of the explosion experiments.

KROTOS K-44

The KROTOS K-44 test has been performed using the aluminum oxide as simulant melt. The melting temperature of Al_2O_3 allows one to assess the void buildup and the solidification of melt if occurs as close to reactor conditions as possible. Detailed experimental data can be taken from technical report [88].

The K-44 test has been performed in near saturation conditions. The water sub-cooling is 10 K. The total melt mass was 1.5 kg. The initial velocity at the nozzle outlet of the furnace was observed as ~5 m/s. The time of melt-water-contact (start of melt penetration into water) was about 0.05 s. The external trigger was activated at 0.1702 s sending a pressure wave from the bottom upwards producing an escalation explosion. Thus, the total quenching time of fragmented melt was ~0.12 s.

The premixing phase is investigated using the premixing model JEMI. The melt outflow velocity is set to 5 m/s. This corresponds to ~10 kg/s by melt density of $\rho_{Al_2O_3} = 2600 kg/m^3$. The average void fraction in mixture is obtained ~45%. The global void is calculated ~15% with the calculated water swell of 0.2 m in average. Compared to the test, the experimental water swell have oscillated between 0.1 and 0.4 m during the premixing, [88]. The Sauter mean diameter of melt drops in mixture is calculated 9 mm. For this, the jet breakup model parameters has been chosen as for FARO calculations: $f_{fl} = 0.5$, $f_d = 0.2$, $f_F = 0.25$ and $f_B = 0.7$. The trigger time is set to 0.26 s when the pouring of 1.5 kg melt into water is finished and the total mass entered the water.

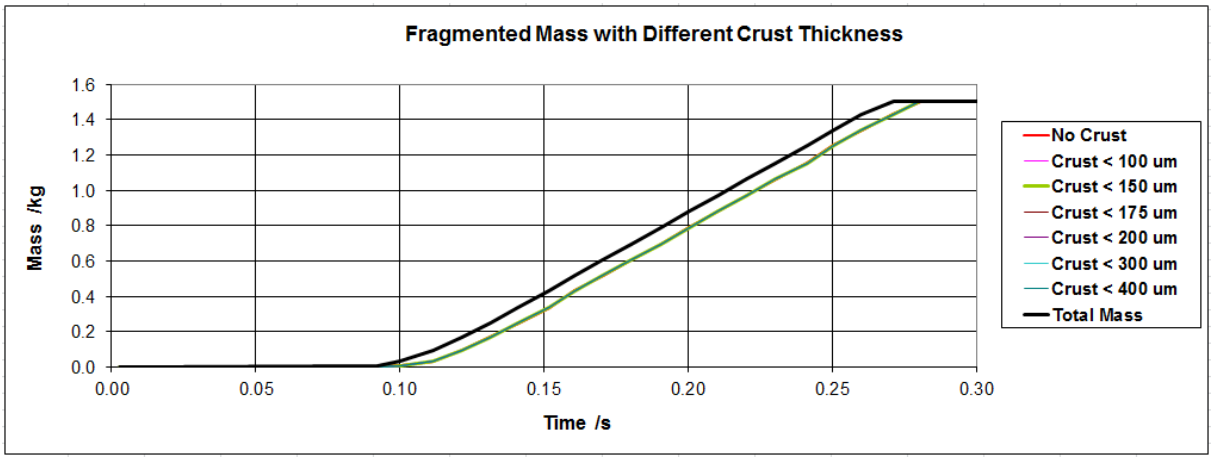

Fig. 6-11: Mass distribution of melt drops with respect to the crust thickness in the premixing phase, KROTOS K-44 experiment, JEMI calculation.

Fig. 6–11 shows the time development of the melt fraction in mixture with different crust thickness. The diagram indicates that the total mass of melt is still staying liquid and thus available for fine fragmentation. This could be explained by a large diameter of the melt drops approx. 9 mm and the high superheating of the melt of 374 K. Also, the material properties of aluminum oxide as high heat conductivity and heat capacity accounted to that slow solidification of the melt drops.

Fig. 6-12 shows the calculated pressure development at different locations, which correspond to the installed pressure transducers in the experiment. The calculation results have a good agreement with the experiment. Merely, a slight overtaking of pressure peaks is obtained at the last two transducers. No melt solidification is obtained in the calculation.

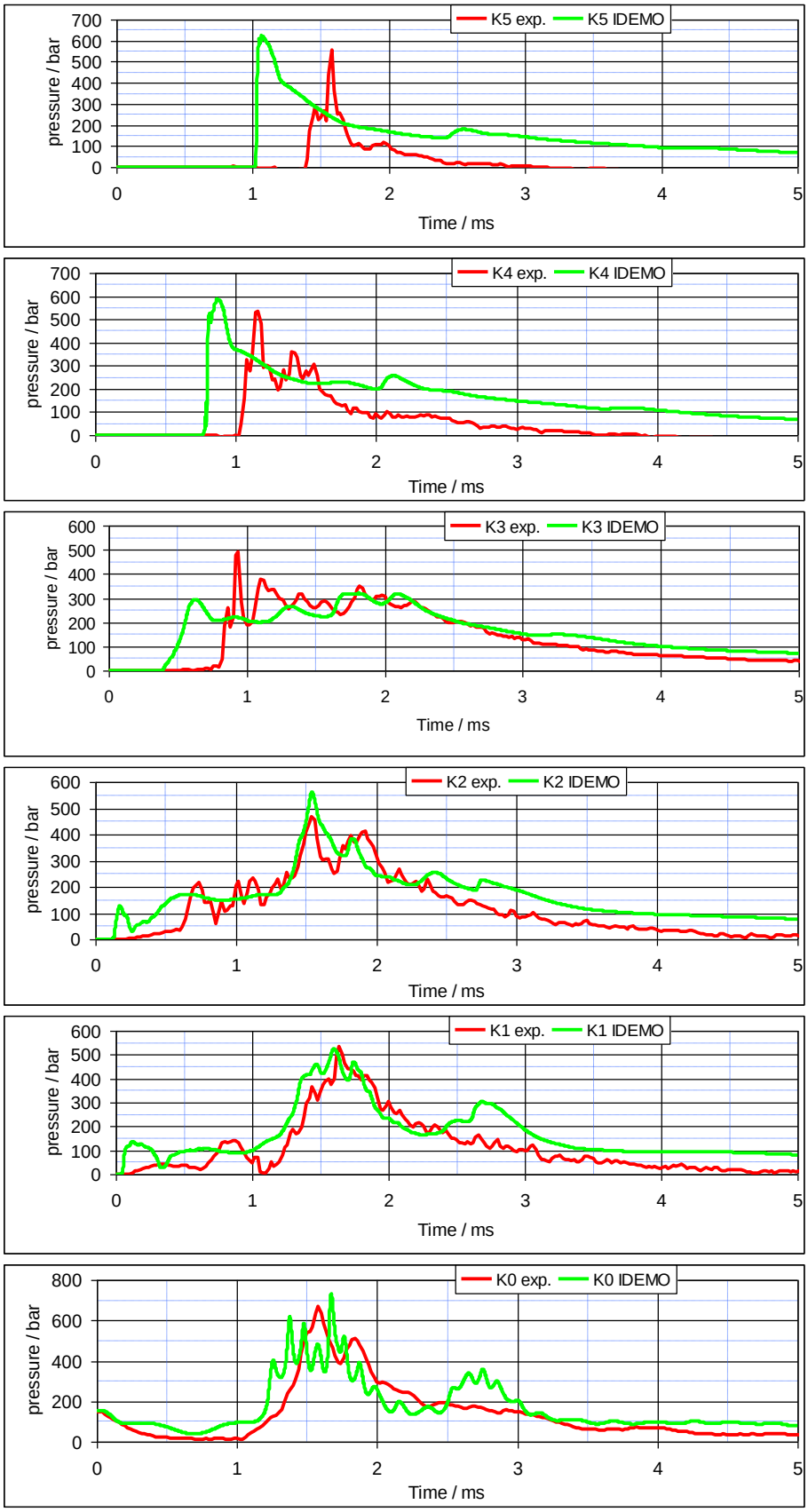

Fig. 6-12: Pressure development, comparison of IDEMO-3D calculation with the experimental results for KROTOS K-44, Al_2O_3.

KROTOS K-52

The KROTOS K-52 test has been performed using the corium melt. Detailed experimental results can be found in [21]. The water sub-cooling was 102 K. The observed void fraction during the premixing was relatively low, about 13%. The external trigger was activated at 0.7 s. The time of melt-water-contact (start of melt penetration into water) was about 0.3 s. Thus, the total quenching time of fragmented melt was ~0.4 s.

The premixing phase is calculated using the premixing model JEMI. The melt flow rate from the furnace outlet is assumed to be ~10 kg/s, which corresponds to a melt outflow velocity of ~2 m/s. The first melt-water-contact is calculated at 0.13 s. The trigger time set to 0.4 s. This is the time with maximum fragmented melt mass in mixture staying liquid. The Sauter mean diameter of melt drops is calculated as 3.3 mm. For this, the jet breakup model parameters has been chosen as for FARO calcualtions: $f_{fl} = 0.5$, $f_d = 0.2$, $f_F = 0.25$ and $f_B = 0.7$. The average void fraction in mixture at the trigger time is estimated ~22%.

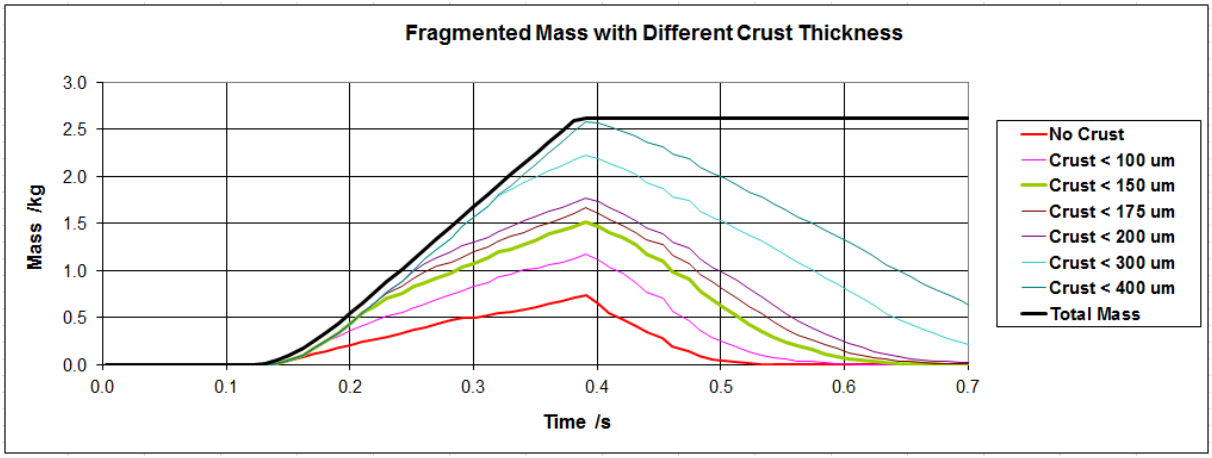

Fig. 6-13: **Mass distribution of melt drops with respect to the crust thickness in the premixing phase, KROTOS K-52 experiment, JEMI calculation.**

Fig. 6-13 shows the mass distribution of fragmented melt in mixture with respect to crust thickness. This indicates the mass fraction in mixture available for fine fragmentation in the explosion stage. At triggering, only 0.6 kg (23%) of the melt has no crust and ~1.5 kg (~58%) have the crust thickness of ~0.15 mm (10% of the drop radius). The relative crust thickness of ~10% is experimentally observed to be a physical limitation for fine fragmentation, see [10,12,15]. Above it, a strong decrease of fine fragmentation ability of melt drops in a shear flow is observed. Thick crust on drops inhibits the fine fragmentation and reduces the explosiveness of the mixture.

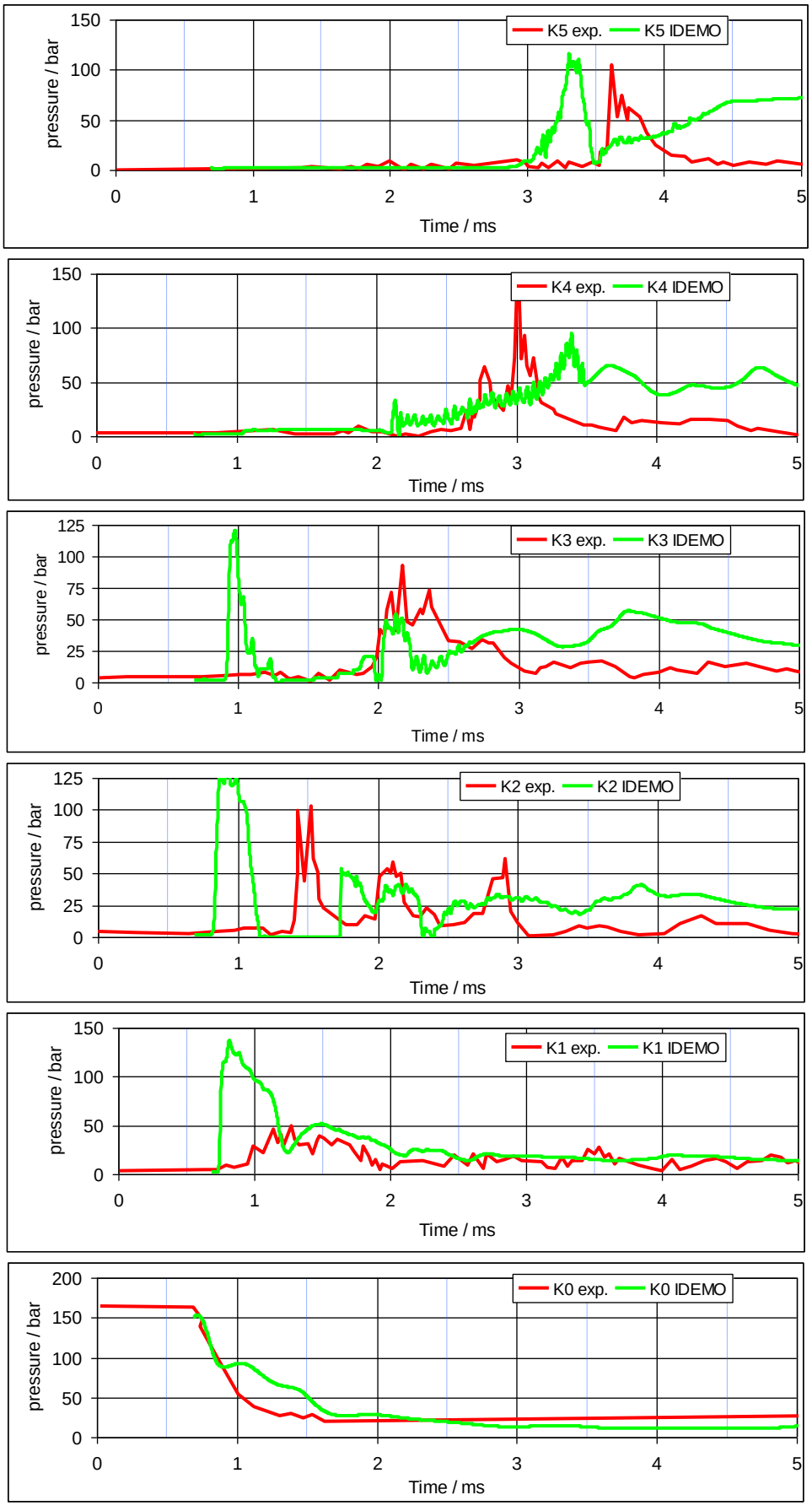

Fig. 6-14: **Pressure development, comparison of IDEMO-3D calculation with the experimental results for KROTOS K-52, Corium 80-20.**

Fig. 6-14 shows the time development of the pressure loads at different locations, which correspond to the installed pressure transducers in the test. In general, the calculation results have a satisfying agreement with the experiment. At K2 and K3 locations, pressure peaks are obtained overtaking the experimental pressure development. The differences cannot be explained since no data from the premixing stage exists due to triggering. However, it can be concluded that the pressure rise fall well in the experimental result range. No large difference between experiment and calculation exist concerning the development of maximum pressure loads.

KROTOS K-58

The KROTOS K-58 test has been performed similar to KROTOS K-52 using corium melt. A detailed experimental information data can be found in [86]. The differences between K-58 to K-52 are a higher subcooling of water of 125 K, higher melt superheating of 227 K and larger melt mass 3.6 kg in the test.

In the experiment, the impact of melt jet on the water surface was detected at time ~0.3 s. The duration of injection in test K-58 was limited by the operation of the gas trigger device, which was initiated at time 0.77 s. The real time of pouring of melt into water was limited to 0.47 s after melt water contact.

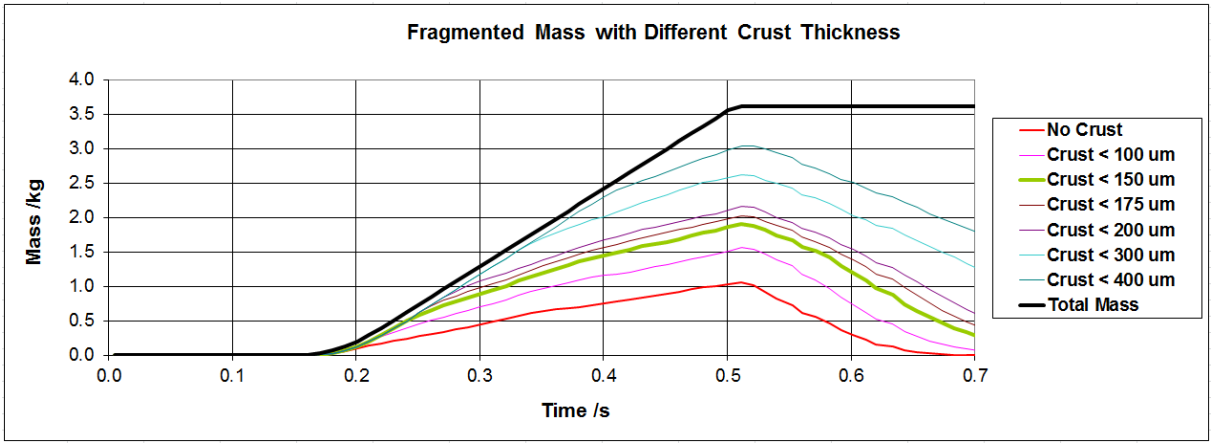

Fig. 6-15: Mass distribution of melt drops with respect to the crust thickness in the premixing phase, KROTOS K-58 experiment, JEMI calculation.

The premixing phase is calculated using the premixing code JEMI. The melt flow rate from the furnace outlet is assumed ~10 kg/s, which corresponds to the melt outflow velocity of ~2 m/s. The first melt-bottom-contact is determined at ~0.17 s. The later melt-water-contact in comparison to K-52 is due to a lower water level in K-58 and greater falling time in gas. The trigger time is set in the calculation to 0.52 s at the time with maximum fragmented melt mass in mixture staying liquid. The Sauter mean diameter of melt drops is calculated 3.3 mm. For this, the jet breakup model

parameters has been chosen: $f_{fl} = 0.5$, $f_d = 0.2$, $f_F = 0.25$ and $f_B = 0.7$. The average void fraction in mixture at the triggering time is estimated ~22%.

Fig. 6-15 shows, similar to K-52, the time development of the mass of fragmented melt with respect to the crust thickness indicating the solidification of the melt. At the triggering time, only 0.9 kg (23%) of the melt have no crust and ~1.5 kg (~58%) have the crust thickness of ~0.15 mm (10% of the drop radius).

Fig. 6-16 shows the calculated pressure development at different locations, which correspond to the experimental pressure transducers. As in K-52, no propagating energetic steam explosion is produced in the calculation. Differences between the experimental and calculation results are obtained in the peak onset. These differences cannot be explained since no data from the premixing phase exists due to triggering. The different behavior of the mixture during the detonation might be led back to some uncertainties or inhomogeneities in melt outflow from the nozzle and thus the jet breakup that is not considered in the theoretical investigation. In general, the calculation results have a good agreement with the experiment with respect to the peak pressure loads. Similar to K-52, the pressure rise fall well in the experimental result range.

In contrast to the previous investigations, the current results did not lead to any overestimation. The explanation is that the solidification during the premixing phase, which is considered in the present modeling, plays a significant role during the explosion. The final conclusion is that the solidification of melt fragments during the premixing phase limits the explosiveness of the entire mixture in the explosion phase. Moreover, the drop solidification accounts for the difference between corium und aluminum oxide concerning the development of pressure loads.

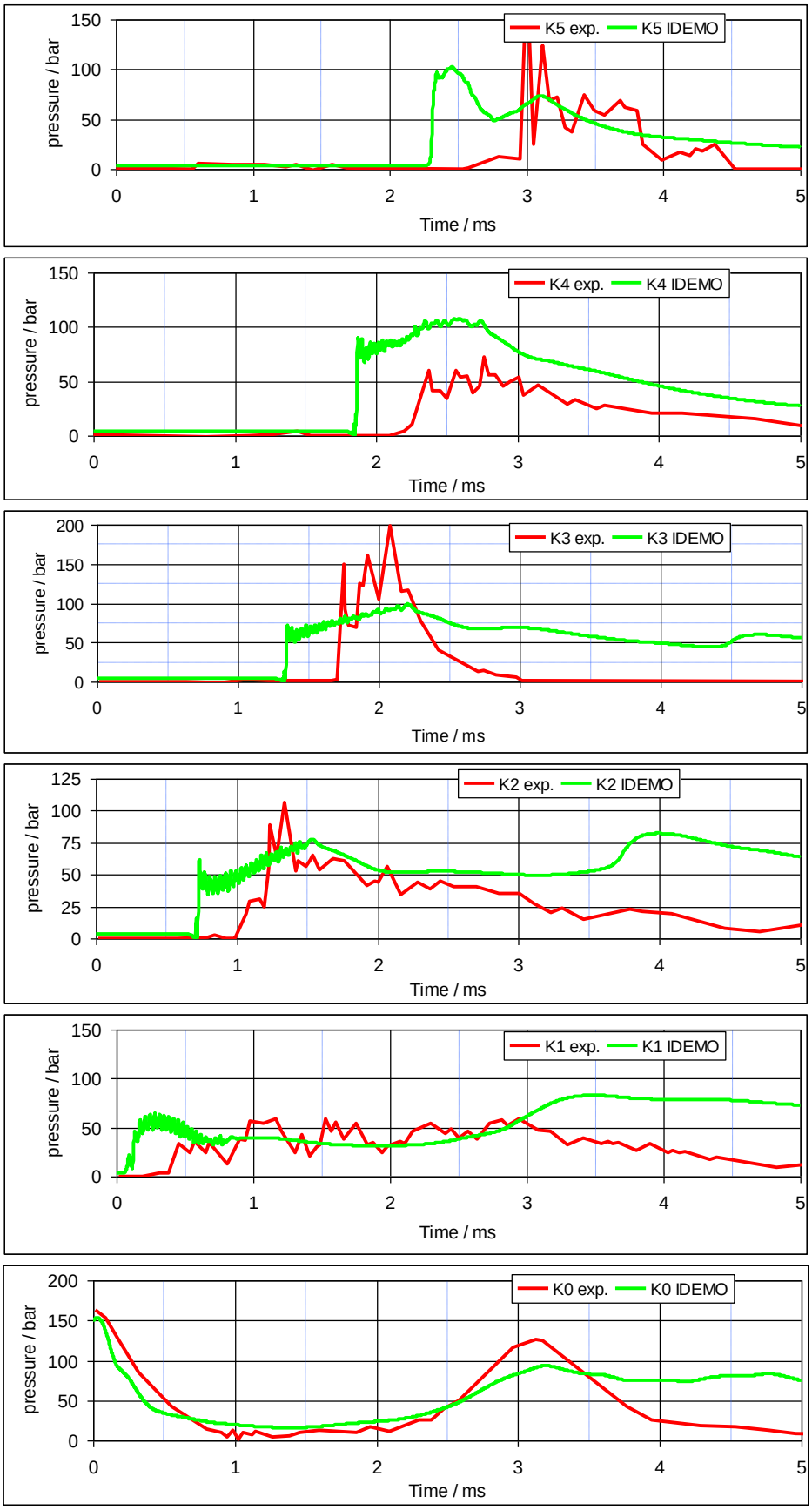

Fig. 6-16: **Pressure development, comparison of IDEMO-3D calculation with the experimental results for KROTOS K-58, Corium 80-20.**

7 Reactor applications

Severe accidents with steam explosions are caused by core melting. Such a scenario postulates the loss of coolant with permanent dry-out of the reactor core. These accidents are the outcome of a failure in the main and emergency cooling systems following, for instance, an earthquake, external or internal flooding, which are usually beyond the plant design due to extremely low occurrence frequency but still probable, as the Japanese accident on March 11th 2011 demonstrated. They have a large impact on the environment and the population. Therefore, they need to be analyzed in terms of the possible consequences. Without cooling, fuel rods start to melt due to the decay heat and build up a melt pool inside the core region of the reactor vessel. Due to the permanent heating up and melting of the surrounding structures, the melt flows downwards into the core support plate or sideways into the core barrel. Through open channels in the support plate or over the down-comer, the melt driven by gravity forms jets and comes into contact with water expected to be in the lower part of the RPV. Once in contact with water, the melt breaks up into small fragments in size ranging from a few millimeters and mixes with water. High heat transfer from the fragmented melt produces a vapor film around the melt fragments. This vapor film then reduces the heat exchange between the melt fragments and the surrounding coolant slowing down the solidification process of the melt. This mixture is then designated quasi-stable. Under film boiling, the fragmented melt evaporates part of the water resulting in a certain amount of void (steam content) in the pre-mixture. Once a destabilization of the vapor film around the melt drops (film collapse) has occurred, a rapid local pressure rise ensues, due to strong heat exchange between the melt and coolant and generation of a shock wave, which travels through the mixture causing further film collapse. The interaction of the steam, water and fragmented melt, as well as the balance of steam production and steam removal determines the explosiveness of the mixture.

Generally, there are three accident management (AM) strategies for a severe accident with core melting. The first calls for flooding the reactor cavity and submerging the reactor vessel. The concept has been implemented in the Westinghouse Advanced Plant (AP1000). It is based on the idea that the lower head will arrest the downward relocation of the degraded core from the RPV, by being cooled externally. The mechanism for heat removal from the molten debris in the lower plenum is the nucleate pool boiling of the cavity water. However, in light of the structural complexity in the lower head of the vessel, a failure in the lower head cannot be excluded for all reactor designs, especially as the BWR's have the control rods channels located there. Esmaili et al. [89] investigated the likelihood of a lower head failure and ex-vessel fuel coolant interaction for the AP1000. The investigation showed that the thermal failure of the lower head due to the focusing effect of the stratified light melt layer may be envisaged in certain circumstances leading to the possibility of ex-vessel FCI's. The second strategy addresses the use of the core catcher below the reactor vessel. The core catcher uses thick concrete and a passive

cooling to prevent the molten core from escaping the containment. The core catcher is used in several reactor designs, e.g. EPR from Areva, ESBWR from GE-Hitachi, US-APWR from Mitsubishi and VVER-1200 from Gidropress/Rosatom. The last strategy consists in flooding the reactor cavity without submerging the RPV used in the reactor designs of Generations II and III. The idea is to allow the disintegration of the RPV by thermal loads from molten debris and thus the relocation of the molten materials from the lower head into the reactor cavity filled with water. The molten debris breaks up in water and settles on the cavity floor forming a coolable debris bed configuration.

During contact of the molten debris with water in the cavity, explosive mixing configurations can form, potentially leading to an ex-vessel vapor explosion. Various outflow configurations are possible: from a central outflow with large distances to the surrounding structures up to lateral outflows in closer proximity to the cavity wall. In case of melt outflows far away from any structures (e.g. central melt outflow), pressure loads generated during fuel-coolant interactions are rapidly dampened by large amounts of water remaining present in the vicinity. The resulting loads on the surrounding structures are significantly lower than those inside the interaction zone. By fuel-coolant interactions close to a structure, significantly higher pressure loads can result on the structure due to a smaller distance from the “epicenter” of the pressure increase. Adjacent structures can also affect the interaction of melt and water: both mitigating and enhancing. For instance, the cavity wall during ex-vessel fuel coolant interactions constrains the lateral extension of the mixture close to the wall.

The main focus is to address the extent and distribution of the melt and void due to geometrical constraints affecting the buildup of explosive mixtures. The extent (i.e. concentration and dilution) of the mixture is a key characteristic of the mixture explosiveness. The dilution of the mixture generally leads to a better spatial distribution of the melt and also to the void fraction decreasing the melt concentration and reducing the steam content in the mixing zone by “stretching” the mixing region. High steam content acts as a limiting factor on the pressure increase, dampening shock waves due to its high compressibility. Void reduction always brings as a consequence an increase in the resulting pressure loads. High melt concentrations possibly occurring in non-central configurations support pressure increases due to high concentrations of thermal energy being able to be released. On the other hand, such melt concentrations also cause a very intense evaporation in those regions counteracting local pressure buildup. However, reducing the melt fraction by extending the mixture (no change in mass) also supports a void reduction. Therefore, the spatial extent of the melt and void is one of the most important aspects in multi-dimensional investigations.

The present work addresses primarily the investigation of non-symmetrical (i.e. three dimensional) effects caused by geometrical asymmetry. Their role has to be investigated considering the main limiting factors for vapor explosions, such as the

melt fragmentation, the void fraction in the mixture, the solidification of the melt, explosion venting etc. 2D and 3D calculations have to be performed for an ex-vessel reactor scenario with a non-symmetric configuration in order to assess three-dimensional effects on the explosion potential and resulting loads, which can challenge the integrity of the primary containment. The calculation results must be compared and the impact of the asymmetry should be derived.

7.1 Investigation to 3D effect in reactor applications

Previously, investigations to asymmetry had been attempted using two-dimensional models IKEJET/IKEMIX and IDEMO by Vujic [77]. Generally, there are two ways to analyze such non-symmetric configurations with a lateral melt outflow in 2D. In the first approach, the reactor cavity is considered in 2D cylindrical coordinate system. In this latter case, a non-symmetrical melt outflow is assumed by considering the real melt delivery. This leads to an azimuthal “smearing” of the melt pour. The result is a strong dilution of melt fraction in the mixture. The diluted melt fraction causes a weak evaporation and a strong underestimation of void buildup. The latter acts (as discussed earlier) as the main limiting factor during the explosion phase. The second method is a configuration with a central jet in cylindrical geometry. The radial extension of the calculation domain is varied in order to assess the ‘averaged’ mixture behavior and the role of the adjacent wall. The extent of the fragmented melt and produced steam are dependent of the domain radius due to the confining effect of the domain boundaries. The question concerning the extension of the mixture due to the wall influence cannot be answered adequately in reality. Vujic [77] considered the second method as more appropriate and applied it to an in-vessel reactor scenario with vapor explosions. Vujic used the 2D code versions for premixing and explosion (IKEJET/IKEMIX, IDEMO) to investigate the main limiting effects on a steam explosion with a geometrical constraint.

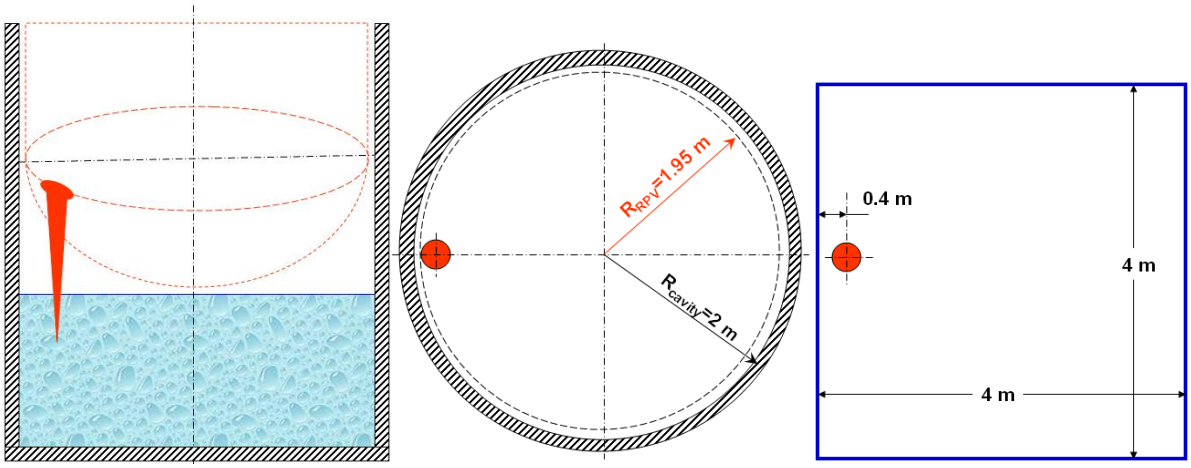

Fig. 7-1: **Schematic illustration of ex-vessel case with an asymmetric melt jet outflow from the RPV into the reactor cavity filled with water; front, top and simplified views.**

With the presently developed code versions JEMI and IDEMO-3D, the asymmetry (three-dimensional) effects can now be checked with the real geometry. A qualitative comparison with the prediction for the explosion strength performed by Vujic [77] is then feasible. In order to achieve this, calculations are necessary in full 3D Cartesian

geometry and in 2D cylindrical geometry with a lateral melt pouring from the RPV into the reactor cavity filled with saturated water, see Fig. 7-1.

Table 7-1: Scenario initial conditions

System pressure	MPa	0.2
Initial water temperature	K	408
Water level	m	1.0 / 2.0
Melt composition	-	corium 80/20
Initial melt temperature	K	3050
Jet release	m	2.33
Jet diameter	cm	10 / 20 / 40
Mass flow rate	kg/s	188 / 754 / 3016
Calculation domain: LxBxH	m^3	4x4x4
Distance jet-wall	m	0.4

The initial conditions for 2D and 3D calculations are presented in Table 7-1. The melt is corium 80/20 with an initial temperature of 3050 K (melt superheat of 150 K). It comes in contact with saturated water in the reactor cavity with a system pressure of 0.2 MPa. A pressure of 0.2 MPa is considered realistic during an accident with core melting, since a moderate over-pressurization of the primary containment is expected. The following variations of mass flow rate are considered: 188, 754 and 3016 kg/s. The water level is assumed to be 1 and 2 m. The distance between the melt jet axis the cavity wall is 0.4 m. The jet release is set in all variations at the height of 2.33 m. The 2D calculations are performed in a cylindrical geometry with a height of 4 m and the radius of 1 m for premixing. The author [65] investigated the effect of close walls on the mixture extension by varying the calculation domain radius. The variations showed different behavior in the mixture with different radial extensions. With the smallest radial extension, a strong concentration of the melt can be produced leading to high voiding of the mixing zone. With larger radial domain extensions, the effect of the RPV wall cannot be adequately covered. The largest melt mass in the region with limited void was obtained with intermediate distances. It was explained by flows in radial and azimuthal direction of void and melt from the regions close to the wall due to high vaporization and pressure buildup. The variation of the calculation domain radius was also considered by Vujic [77] in calculations for a single melt jet in direct proximity to a wall for similar initial conditions. The radius of 1 m was found as a fair estimate for the “averaged” mixture behavior during the premixing, i.e. the melt extent and vaporization of the mixing zone.

The domain radius for the explosion calculations is set at 0.4 m – the minimal distance between the jet axis and the cavity wall. It leads to obtaining the maximum loads at the wall and excluding the dampening effect of surrounding water. The 3D calculations are performed using a Cartesian geometry. The domain size is chosen as 4.0 x 4.0 x 4.0 m^3 for the length, width and height, respectively. The cylindrical

geometry of the cavity plays a minor role during the premixing and explosion phase due to the very large dimension and thus can be neglected.

7.1.1 Premixing phase

The 2D calculations for the premixing phase are performed using the JEMI program code in cylindrical coordinates with one central melt jet. Fig 7-2 shows the numerical discretization of the calculation domain for 2D calculations. The domain radius is 1 m and the height is 4 m. Two water pool depths are studied: 1 m (a) and 2 m (b). The 3D calculations are carried out using JEMI in 3D Cartesian coordinates. The domain geometry and the numerical discretization in 3D calculations are shown in Fig. 7-3. Two different types of nodalization are presented for numerical reasons: for water levels of 1 m and 2 m. The melt outflow is represented as a melt jet close to the wall; see Fig. 7-3 (top). The cylindrical form of the reactor cavity is not modeled. The nodalization of both 2D and 3D configurations is identical, in order to avoid discretization effects.

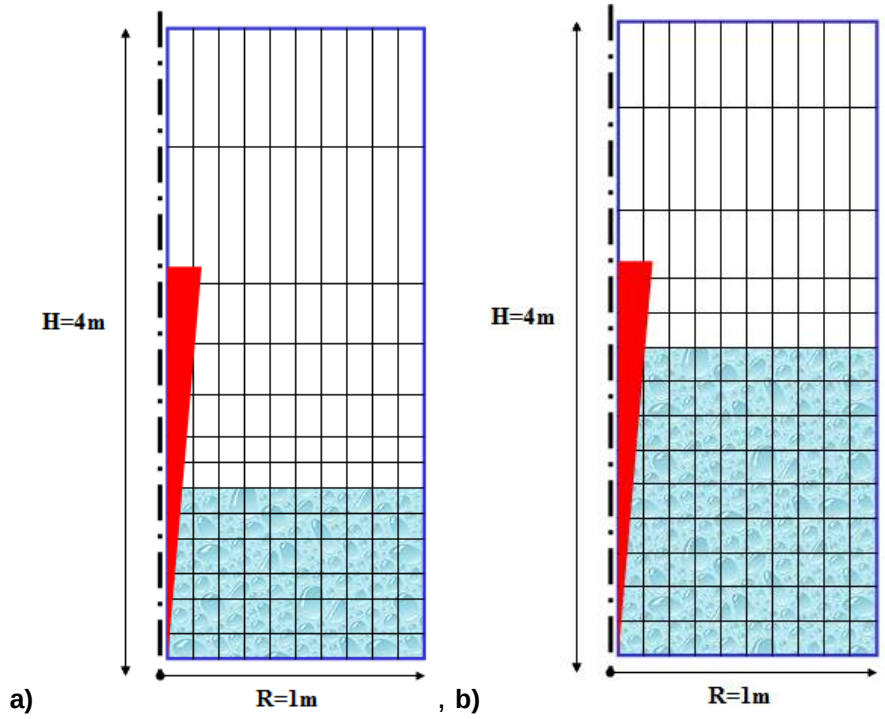

Fig. 7-2: **Numerical discretization used for premixing calculations performed with JEMI code in 2D, central melt jet, with water level of 1 m (a) and 2 m (b).**

Table 7-2 shows the results from the investigations with JEMI in a cylindrical geometry using 2D approximations. The investigation results of the 3D calculations are summarized in Table 7-3. In both cases, the depth of the water pool and the mass flow rate have been varied. Six configurations are studied: for a water level of 1 and 2 m and a mass flow rate of 188, 754 and 3016 kg/s. As discussed in Chapter 3, the fragmented melt mass mixed with limited void is considered as the main

characteristic for the mixture explosiveness. Fragmented melt mass is a key factor during steam explosion indicating the stored thermal energy available for release, i.e. available for conversation into mechanical work. The void leads to a moderation factor for pressure increases. For this, the role of geometrical constraints has to be discussed.

In order to assess the proportion of melt and void, the explosiveness potential of the pre-mixture, four different regions are distinguished with respect to melt and steam contents: the mass of fragmented melt in the mixture with a void less than 30%, 40%, 50%, 60%. The results are estimated at the first melt-bottom-contact (MBC). MBC is defined as the first contact of melt jet with the bottom by incomplete jet breakup or the moment of departure of the first melt fragments on the bottom if the melt jet is completely fragmented in water. MBC is assumed as the most likely moment when a steam explosion will be triggered due to entrapment of water by melt resulting in direct contact between the melt and the water. This induces an initial pressure rise generating a shock wave, which propagates through the mixture causing a vapor film collapse and fine fragmentation of melt drops inducing further pressure increases. In the configurations with a water level of 1 m, the MBC is obtained at 0.45 s. In cases with a water level of 2 m, the MBC is obtained at 0.79, 0.45 and 0.45 s for a jet diameter of 10, 20 and 40 cm, this is identical in 2D and 3D calculations. Except for the case with a jet diameter of 10 cm and water height of 2 m, the coherent jet contacts the bottom earlier than the fragmented melt due to the lower hydrodynamic drag of the jet modeled as a cylinder falling by gravity into water. Here, an incomplete jet breakup is observed. The amount of fragmented melt mass in the mixture in regions with different void fraction is an important indicator of the explosion strength. As a rule of thumb, larger quantities of fragmented melt masses in mixtures with lower void fraction mean an increase in the mixture explosiveness. Previous investigations with IDEMO to various premixing configurations [63,76] showed that the steam content in mixtures, higher than 50 - 60% significantly limits the possibility of pressure escalation and propagation reducing the resulting pressure loads.

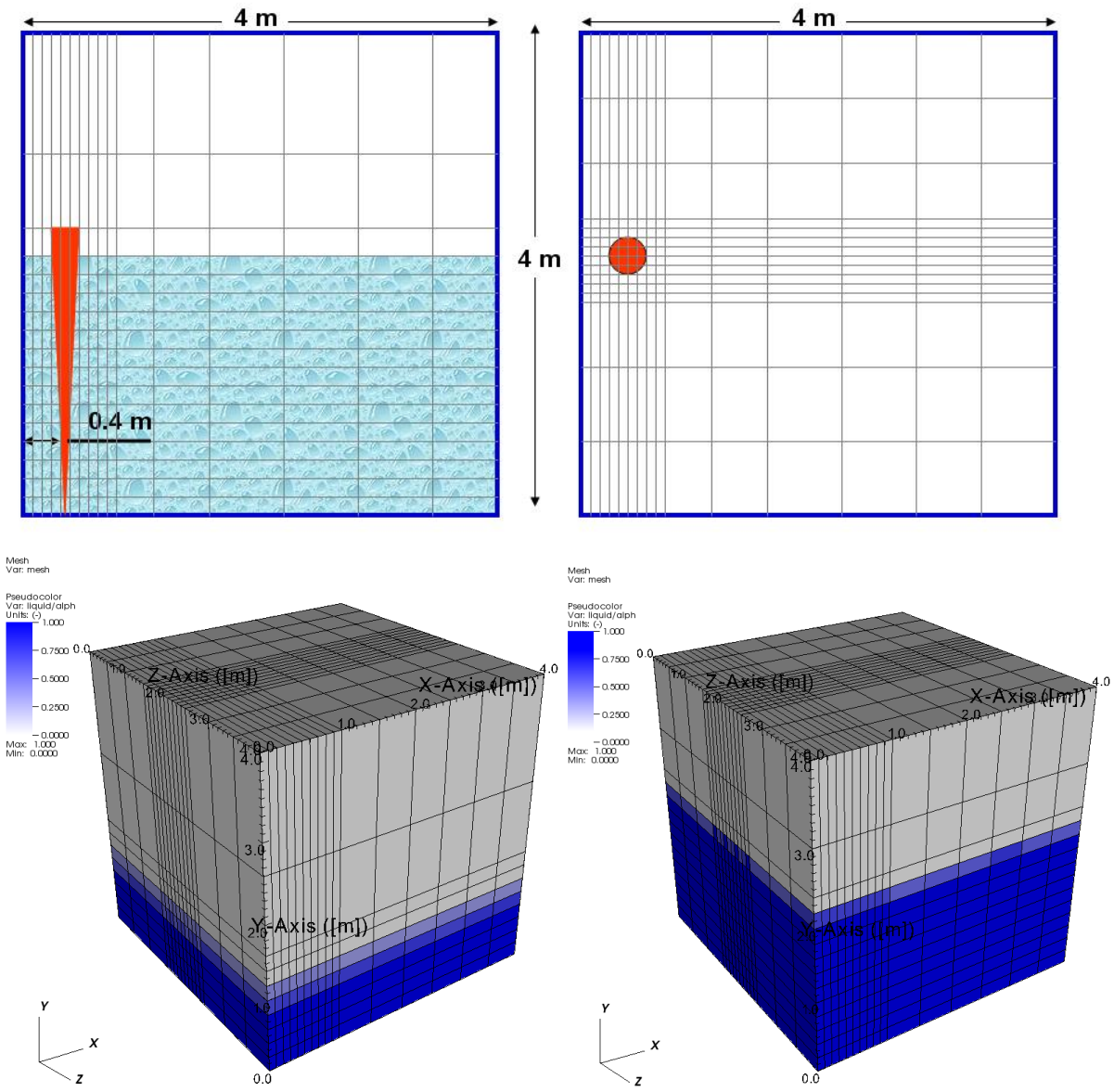

Fig. 7-3: **Numerical discretization used for premixing calculations performed with JEMI code, side and top views (left), 3D view for water pool depth of 1 m and 2 m (right)**

Table 7-2: Overview of the premixing results obtained with 3D code JEMI in 2D cylindrical geometry using 2D approximations for central melt outflow.

		Water level = 1m			Water level = 2m		
Variation		#1	#2	#3	#4	#5	#6
Djet	m	0.1	0.2	0.4	0.1	0.2	0.4
Melt bottom contact	s	0.45	0.45	0.45	0.79	0.45	0.45
Mass flow rate	kg/s	188	754	3016	188	754	3016
Dp (mass mean)	mm	3.75	4.0	4.2	3.7	3.75	3.85
Dp (Sauter mean)	mm	3.45	3.45	3.5	3.5	3.55	3.55
Total mass in mixture	kg	12	24.5	**53.5**	110	120	**277**
Mass in mixture with void less than 30%	kg	1.9	2	**4**	**14**	3.4	9
Mass in mixture with void less than 40%	kg	2	3.5	**5**	**28**	6	19
Mass in mixture with void less than 50%	kg	5	5	**11**	36	19.5	**37**
Mass in mixture with void less than 60%	kg	6	10	**27.5**	68	41	**87**

Table 7-3: Overview of the premixing results obtained with 3D code JEMI in 3D Cartesian geometry for asymmetric melt outflow

		Water level = 1m			Water level = 2m		
Variation		#1	#2	#3	#4	#5	#6
Djet	m	0.1	0.2	0.4	0.1	0.2	0.4
Melt bottom contact	s	0.45	0.45	0.45	0.79	0.46	0.45
Mass flow rate	kg/s	188	754	3016	188	754	3016
Dp (mass mean)	mm	4.0	4.1	4.2	3.6	3.8	3.8
Dp (Sauter mean)	mm	3.55	3.6	3.65	3.3	3.35	3.4
Total mass in mixture	kg	13	25	**53**	110	120	**277**
Mass in mixture with void less than 30%	kg	2.8	3	**4**	**14**	6	9
Mass in mixture with void less than 40%	kg	6	8	**13**	**28**	13	20
Mass in mixture with void less than 50%	kg	11	14	**19**	**37**	20	36
Mass in mixture with void less than 60%	kg	13	21	**33**	69	38	**88**

The 2D and 3D results are generally in very good agreement. The melt bottom contact occurs at the same time. In general, the premixing results both in 2D and 3D show that only a small part of the total melt mass released from the RPV becomes fragmented. The largest amount of mass stays within the melt jet, which is falling in the air and water. Due to incomplete jet breakup in the calculations, large melt amounts reach the cavity floor without being fragmented. The exception is only in configuration #4 with a complete jet breakup. In this case, triggering occurs later when the first melt fragments contacts the cavity floor. The largest mass thus is obtained in the calculations with the greatest mass flow rate of 3016 kg/s with a total fragmented mass of 53 kg and 277 kg for water level 1 m (#3) and 2 m (#6), respectively. The difference compared to the other configurations is due to a larger jet diameter and due to consequently larger fragmenting surface area of the jet, larger than that in cases #1, #2 and #4, #5, respectively. The drop sizes lay in the size range of 3.4-4.2 mm of diameter. This is expected due to a similar jet

fragmentation in 2D and 3D, since the jet breakup model implemented in a separate module is independent of the geometry and discretization. Negligible discrepancies can be caused by different voiding in the initial stage.

Besides the fragmented melt mass, the void in the mixture is another important attribute of the mixture explosiveness. Table 7-4 presents a proportional comparison of fragmented melt fraction in mixtures with a void less than 60% in relation to the total melt mass. The void in the mixture in 2D and 3D show a similarity. Discrepancies between 2D and 3D are obtained only in #1 and #2 with the smallest melt mass in the mixture. A possible explanation lies in the different geometry used for the numerical domain. The small melt amount is initially concentrated close the central region with smaller volume meshes than the outside cells causing a faster voiding in the initial stage. Case #4 with the smallest melt flow rate and later triggering demonstrates a good agreement between 2D and 3D for a later MBC. This indicates that a different behavior is caused by numerical discretization in initial phase only.

Table 7-4: Comparison of the 3D and 2D premixing results with respect to melt fraction in mixtures with void less than 60% in relation to the total melt mass

Case	**3D:** Melt fraction in mixture with void less than 60% (total melt mass)	**2D:** Melt fraction in mixture with void less than 60% (total melt mass)
#1	100% (13 kg)	50% (12 kg)
#2	84% (25 kg)	40% (25 kg)
#3	63% (52 kg)	51% (54 kg)
#4 (later MBC)	63% (110 kg)	62% (110 kg)
#5	32% (120 kg)	34% (120 kg)
#6	32% (277 kg)	31% (277 kg)

As already discussed, the central question as to the role of 3D effects is the radial extent of the mixture and the effect arising from the cavity wall Since an axis-symmetric mixture is always in the result of 2D cylindrical coordinates (no angular component), the mixture in 3D may, by contrast, be deformed by the wall. High asymmetric melt concentrations, stronger steam generation and local pressure rises at the wall are possible. The mixture is expected to expand along the wall and in the direction of water-rich regions. Figs. 7-4 to 7-15 show the volume fraction of fragmented melt and the void for the 3D premixing calculations and the qualitative representation of the melt drops upon triggering. The melt fraction is represented between 0.1% and 5%. In all calculations, the fragmented melt is obtained in the upper part of the water pool. The densest mixture is found in the region close to the

melt jet (left) in the region with the highest void (right). One exception is the two latter calculations #5 and #6, see Figs. 7-12 to 7-15. Here, the densest mixture as well as the highest void is obtained directly at the wall. This is due to the wall proximity confining the extent of the melt cloud and leading to melt concentration at the wall. The stretching effect of the melt concentrations has a compensating character leading to similar melt and void distribution in 2D and 3D.

In general, it can be concluded, that the mixture, melt cloud and void, remain almost symmetric with a light deformation along the wall. This can be only explained by the high density of the corium melt “cutting” into the surrounding water even though it may be fragmented. Also, large expansion of the void cloud towards the water-rich region does not occur, the steam content remains quite symmetric in the mixture. This indicates that the steam release due to local pressure rise occurs mainly in upward direction driven by the hydrostatic head.

The solidification of melt drops is only relevant in configuration #4 with a water level of 2 m and a jet diameter of 0.1 m. Here, a later melt bottom contact is obtained due to complete jet breakup. Fig 7-16 shows the distribution of the fragmented melt with respect to different crust thickness in 2D (a) and 3D (b) calculations. Since the void is the main mixing attribute determining the heat transfer from melt to coolant and thus the solidification of melt drops during the premixing, the melt mass distribution relative to the crust thicknesses is expected to be identical. The amount of fragments where no crust is formed at the surface is obtained in both configurations and stands at ~35 kg. The melt mass with a crust thickness of 175 µm stands at ~75 kg, again in both configurations. The crust thickness of 175 µm represents ~10% of drop radius considered to be the theoretical limit for fine fragmentation by Bürger et al. [10] and Nelson et al. [12].

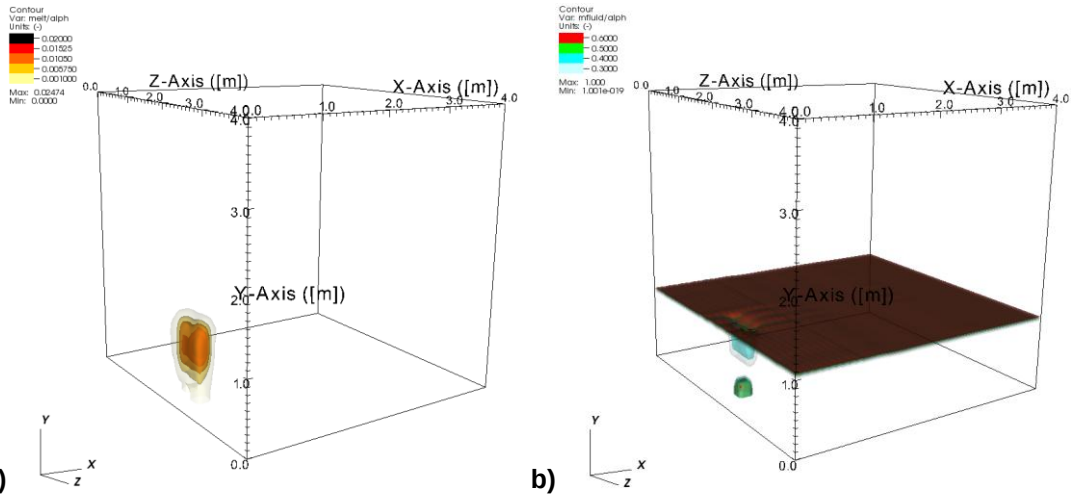

Fig. 7-4: **Contoured board of volume fraction of melt (a) and void (b) at the MBC calculated in JEMI used for explosion calculations, three-dimensional view, with jet diameter of 0.1 m and water level of 1 m**

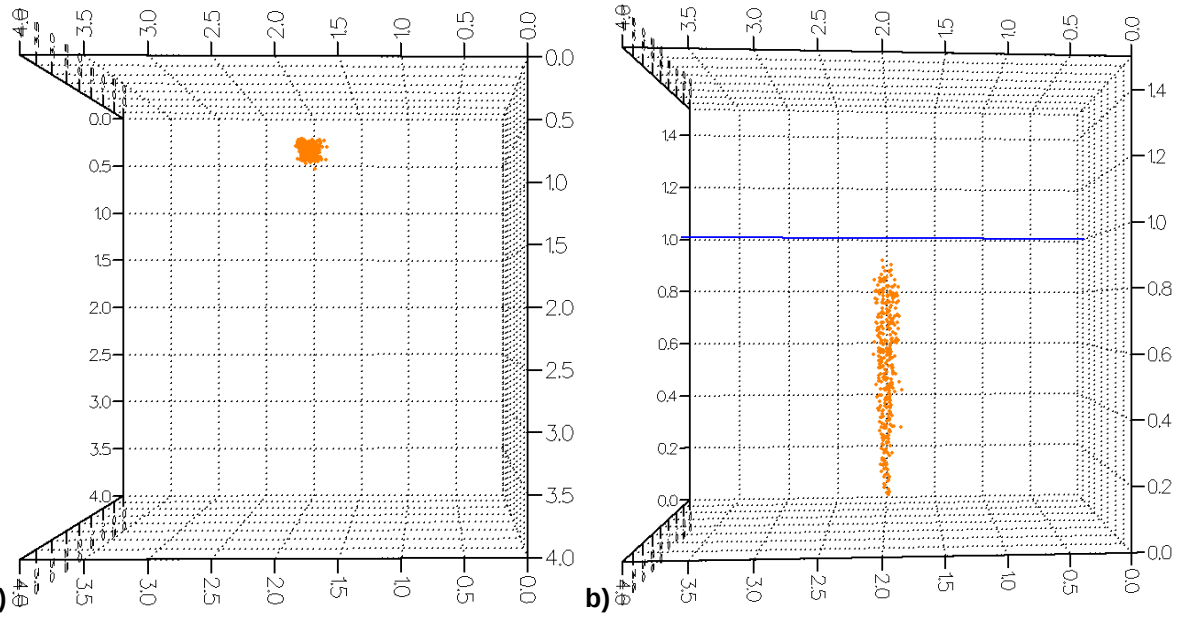

Fig. 7-5: **Representative distribution of melt drops at the MBC calculated in JEMI, (a) top view and (b) side view, three-dimensional view, with jet diameter of 0.1 m and water level of 1 m**

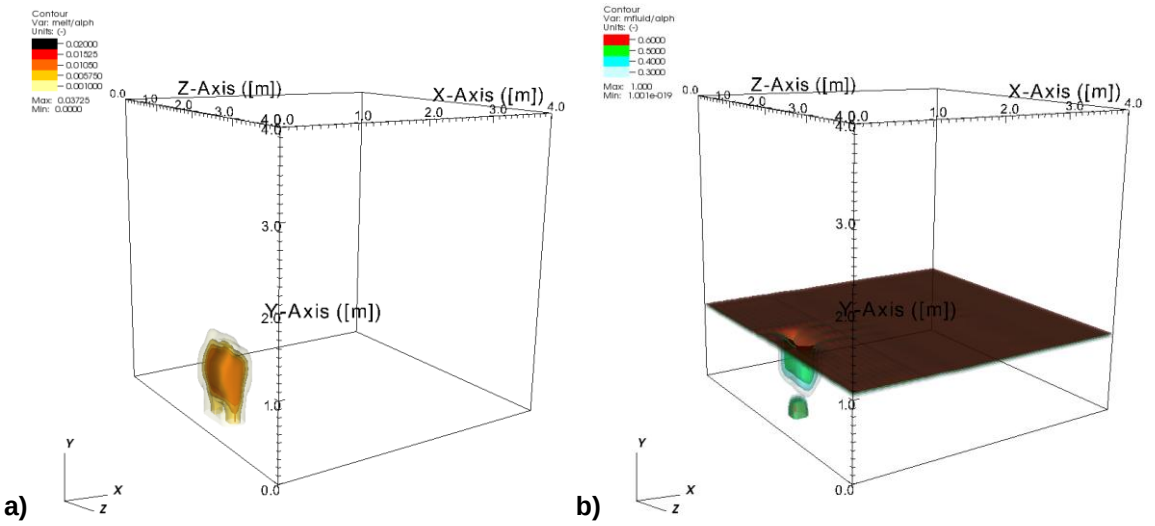

Fig. 7-6: **Contoured board of volume fraction of melt (a) and void (b) at the MBC calculated in JEMI used for explosion calculations, three-dimensional view, with jet diameter of 0.2 m and water level of 1 m**

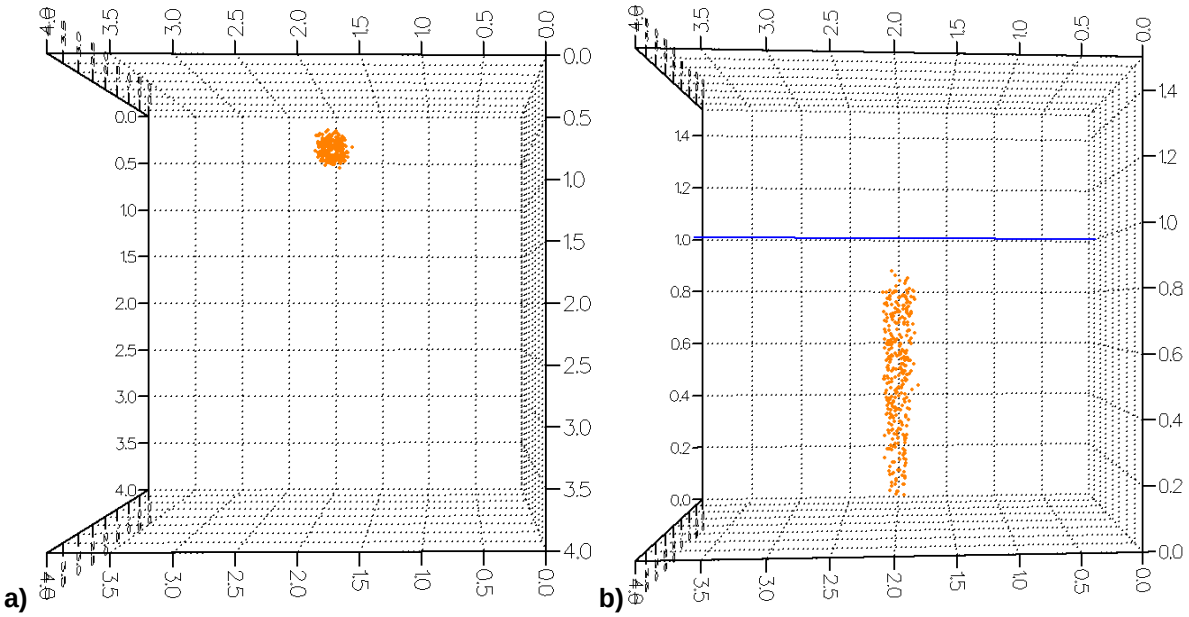

Fig. 7-7: **Representative distribution of melt drops at the MBC calculated in JEMI, (a) top view and (b) side view, with jet diameter of 0.2 m and water level of 1 m**

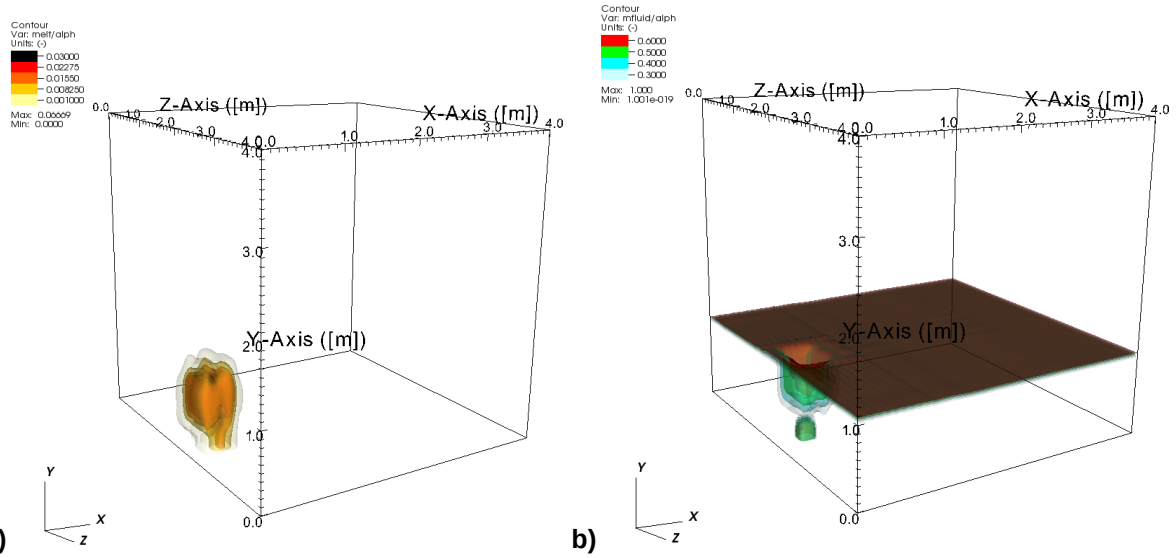

Fig. 7-8: **Contoured board of volume fraction of melt (a) and void (b) at the MBC calculated in JEMI used for explosion calculations, three-dimensional view, with jet diameter of 0.4 m and water level of 1 m**

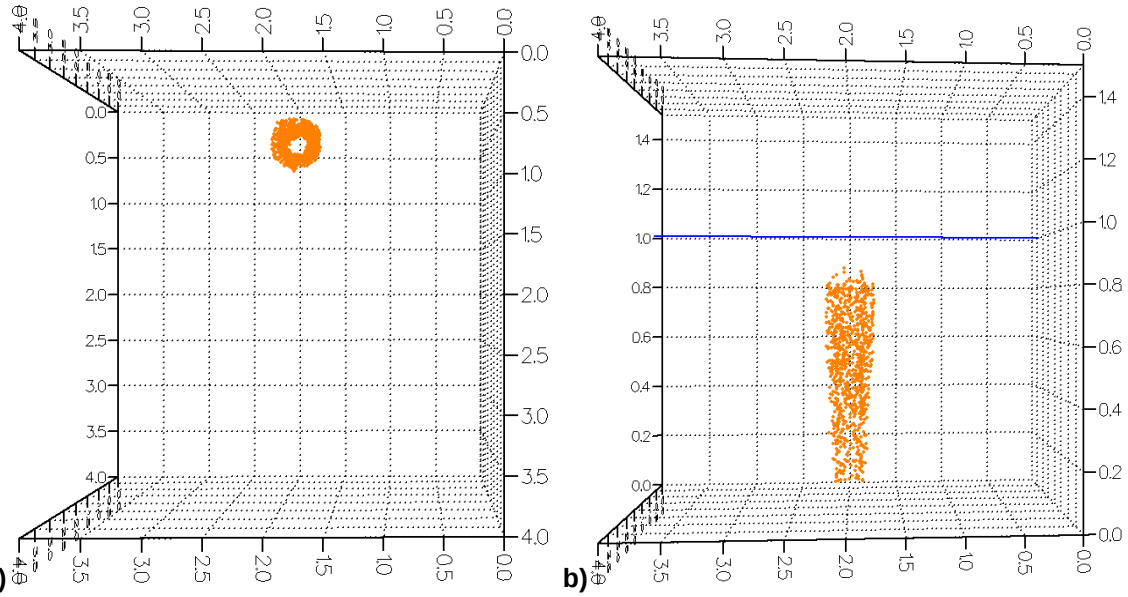

Fig. 7-9: **Representative distribution of melt drops at the MBC calculated in JEMI, (a) top view and (b) side view, with jet diameter of 0.4 m and water level of 1 m**

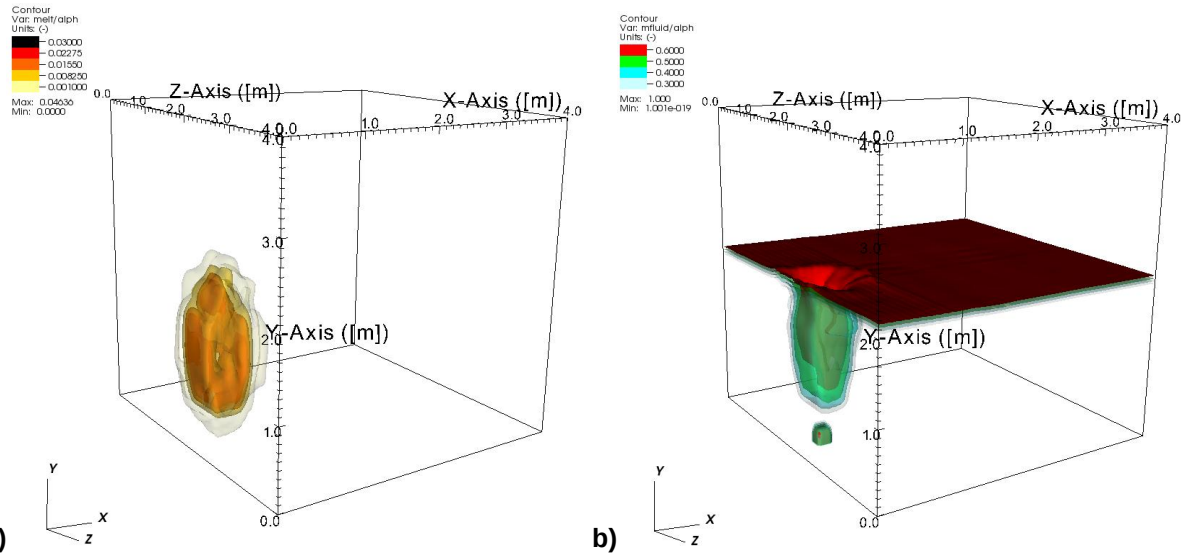

Fig. 7-10: **Contoured board of volume fraction of melt (a) and void (b) at the MBC calculated in JEMI used for explosion calculations, three-dimensional view, with jet diameter of 0.1 m and water level of 2 m**

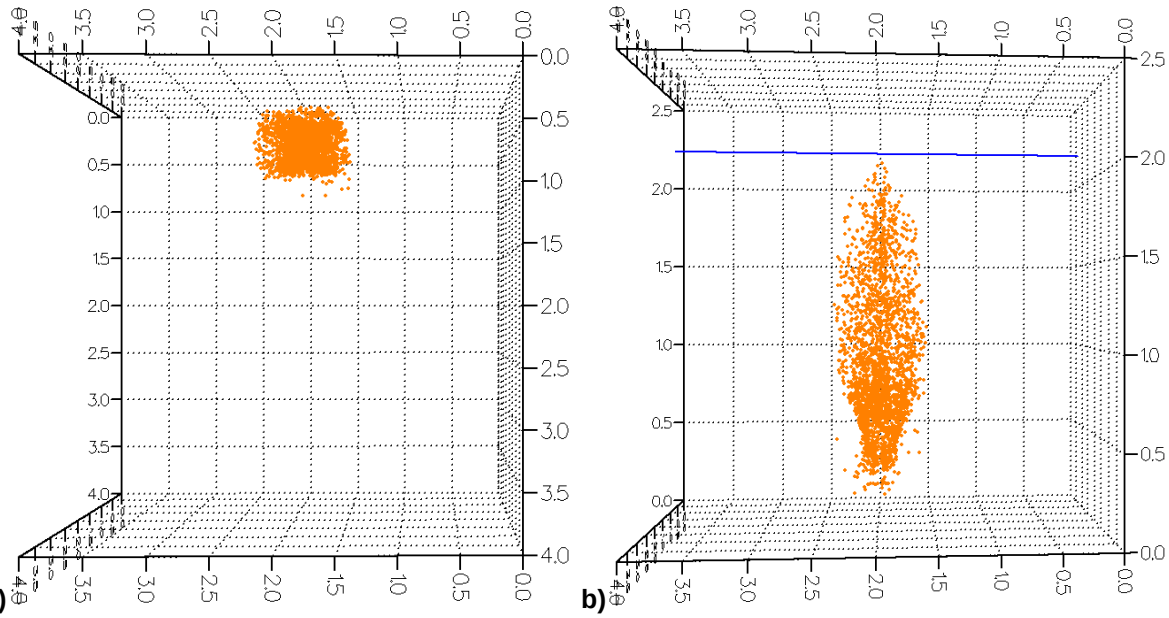

Fig. 7-11: **Representative distribution of melt drops at the MBC calculated in JEMI, (a) top view and (b) side view, with jet diameter of 0.1 m and water level of 2 m**

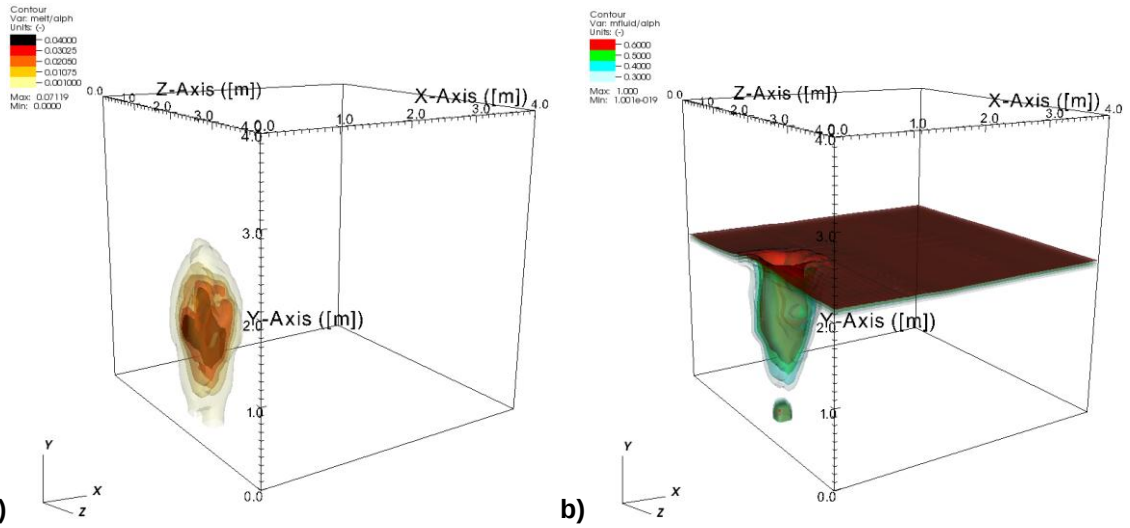

Fig. 7-12: **Contoured board of volume fraction of melt (a) and void (b) at the MBC calculated in JEMI used for explosion calculations, three-dimensional view, with jet diameter of 0.2 m and water level of 2 m**

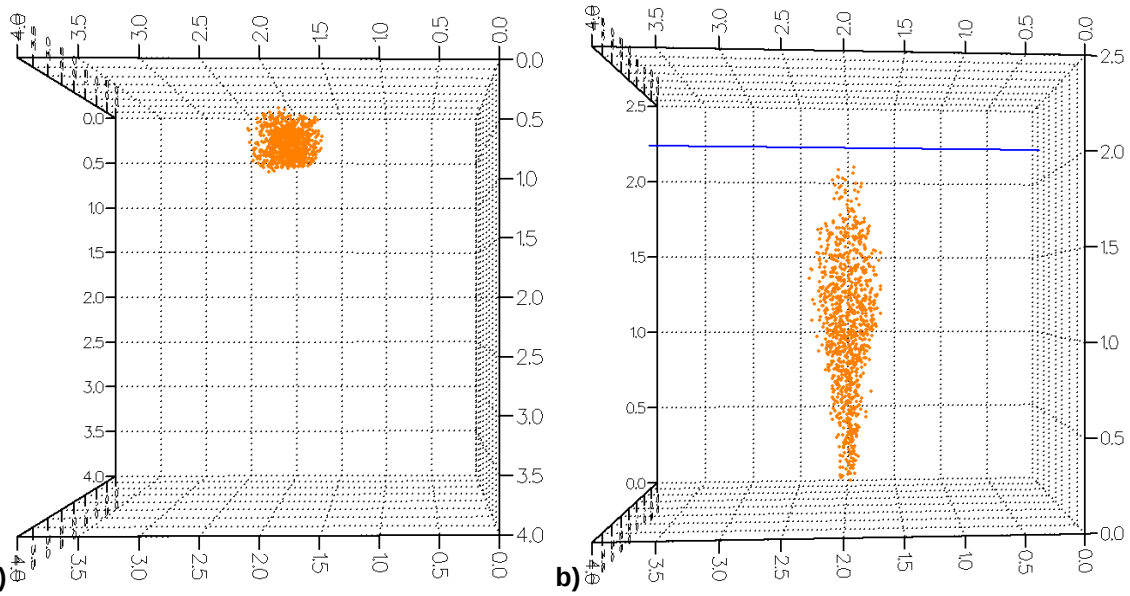

Fig. 7-13: **Representative distribution of melt drops at the MBC calculated in JEMI, (a) top view and (b) side view, with jet diameter of 0.2 m and water level of 2 m**

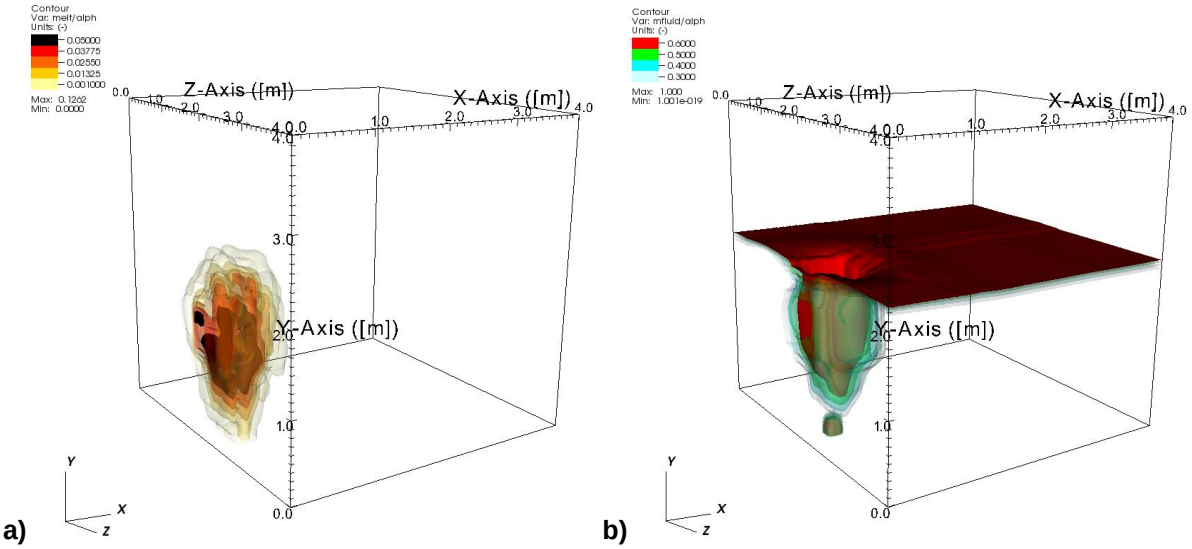

a) b)

Fig. 7-14: **Contoured board of volume fraction of melt (a) and void (b) at the MBC calculated in JEMI used for explosion calculations, three-dimensional view, with jet diameter of 0.4 m and water level of 2 m**

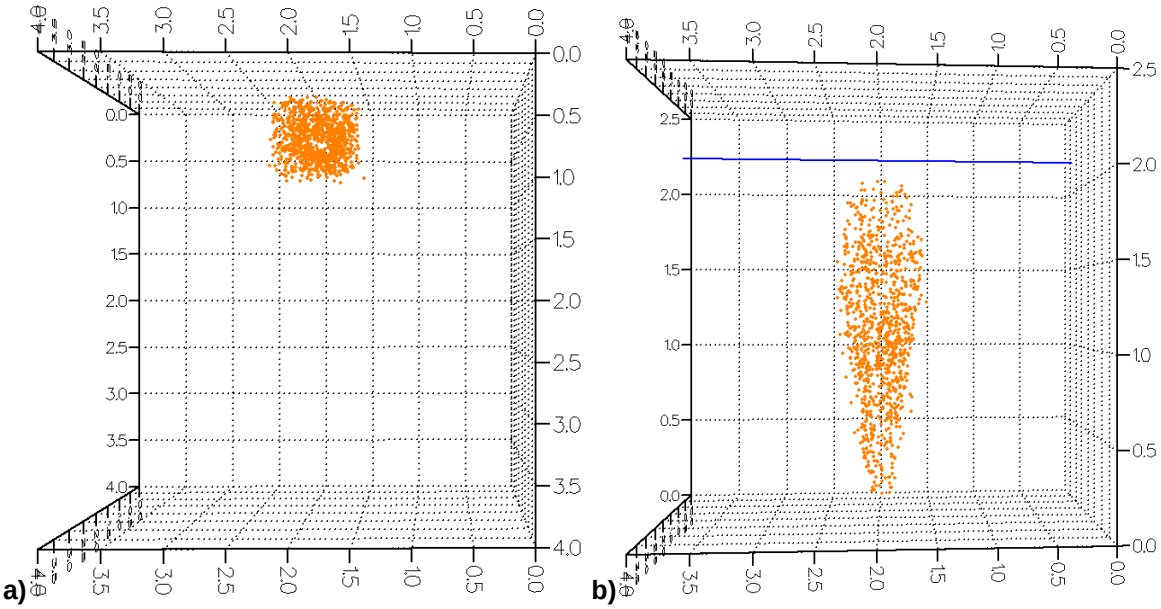

a) b)

Fig. 7-15: **Representative distribution of melt drops at the MBC calculated in JEMI, (a) top view and (b) side view, with jet diameter of 0.4 m and water level of 2 m**

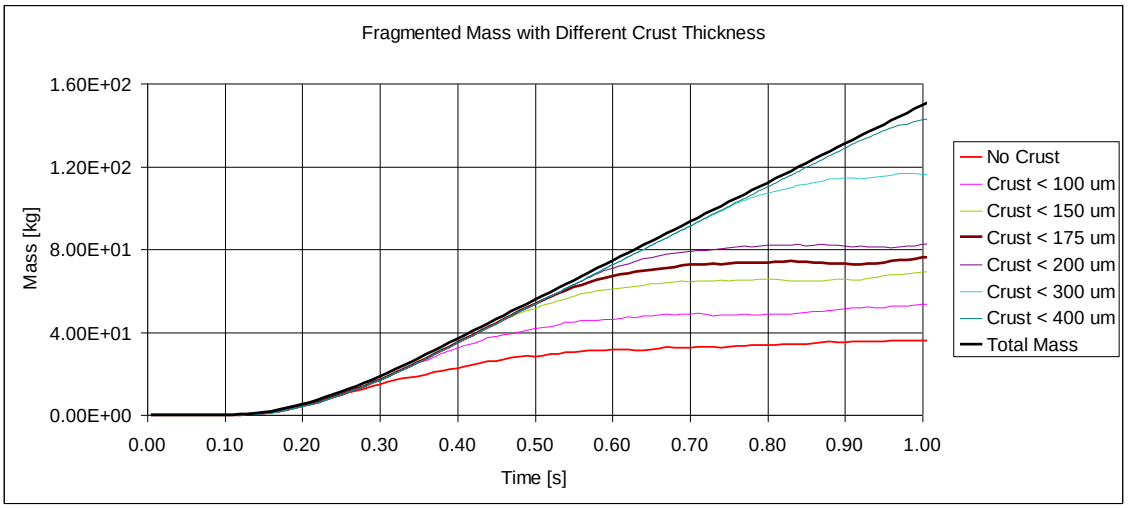

a)

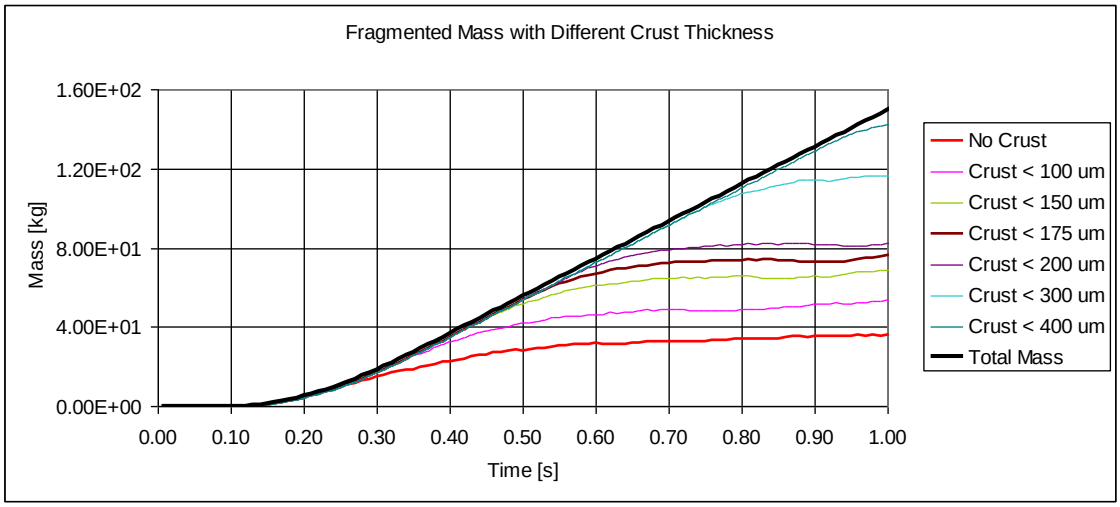

b)

Fig. 7-16: Fragmented melt mass in regions with different crust thickness in 2D and 3D calculations performed with JEMI code, water level = 2 m, D_{jet} = 0.1, 2D (a), 3D (b), triggering at 0.79 s.

7.1.2 Explosion phase

The premixing results from the 2D and 3D calculations presented above performed at the time of the melt-bottom-contact (MBC) have been used for the calculation of the explosion phase made with the IDEMO-3D code. The volume fractions of water, vapor and melt are directly imported from the premixing calculations performed with JEMI. The melt drops represented using the Lagrangian method in JEMI are transformed into the Eulerian description and partitioned into 7 different particle groups with respect to solidification degree, i.e. crust thickness. With the steam content in the mixing zone, the crust thickness at the surface of melt droplets is considered to be an important limitation for fine fragmentation due to strong breakup resistance determining the intensity of melt-coolant interactions and accordingly the magnitude of pressure increases and the strength of the steam explosion. Considering the different fine-fragmentation behavior of melt drops that solidifiy differently, the partitioning approach into crust thickness groups is applied for melt

drops with respect to their crusts, see for details Chapter 5. The melt temperature in the IDEMO-3D calculations is assumed constant at 2900 K. The representation of the melt jet is neglected in the performed calculations.

For conservatism, the trigger is considered to be strong enough to initiate a steam explosion. Bürger et al. [76] investigated the influence of the trigger on steam explosions. The conclusion, which is based on numerous calculations performed with the detonation model for different premixing configurations, implies that the trigger strength does not affect the increase and propagation of steam explosion, once the trigger is strong enough to induce a sharp shock wave. For this, a small volume with a pressure of 10 MPa and steam volume fraction of 0.99 at the bottom below the melt jet is implemented in the IDEMO-3D calculations and assumed as being sufficient to induce an explosion. The idea is to consider water that is trapped by melt arriving on the floor and is explosively evaporated by direct contact with the melt.

The numerical discretization used for IDEMO-3D calculations in 2D and 3D is shown in Figs. 7-17, 7-18. For the 2D cylindrical geometry, a calculation domain is set to 4 m axially and 0.4 m radially. Since pressure increases are going to be dampened in the water-rich regions without fragmented melt, the radius chosen as a distance to the wall is 0.4 m, in order to properly capture the pressure loads at the wall. In 3D case, the domain size is 4.0x4.0x4.0 m^3 and is identical to the domain size for the premixing phase. For the mixing region, a finer nodalization in the explosion as in the premixing calculations is applied in 2D and 3D, in order to catch local pressure increases and the change of relative velocities determining the fine-fragmentation. The nodalization is identical for both 2D and 3D, in order to avoid discretization effects. The water level corresponds to the imported water and vapor fractions from the corresponding JEMI calculations being interpolated into the IDEMO-3D nodalization.

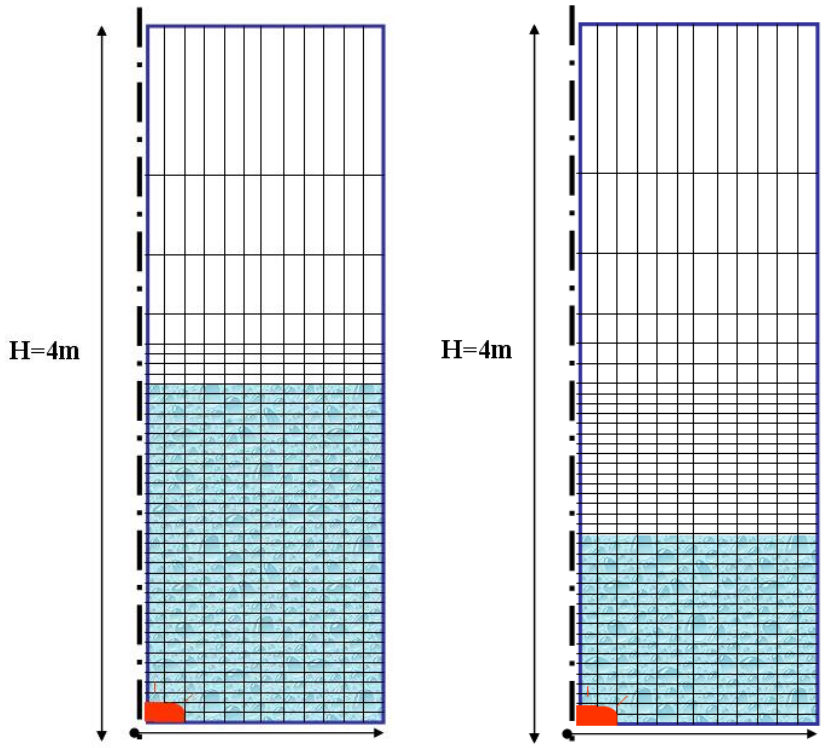

a) , b)

Fig. 7-17: **Numerical discretization in explosion calculation performed with IDEMO code for 2D case, two-dimensional view, with water level of 1 m (a) and 2 m (b)**

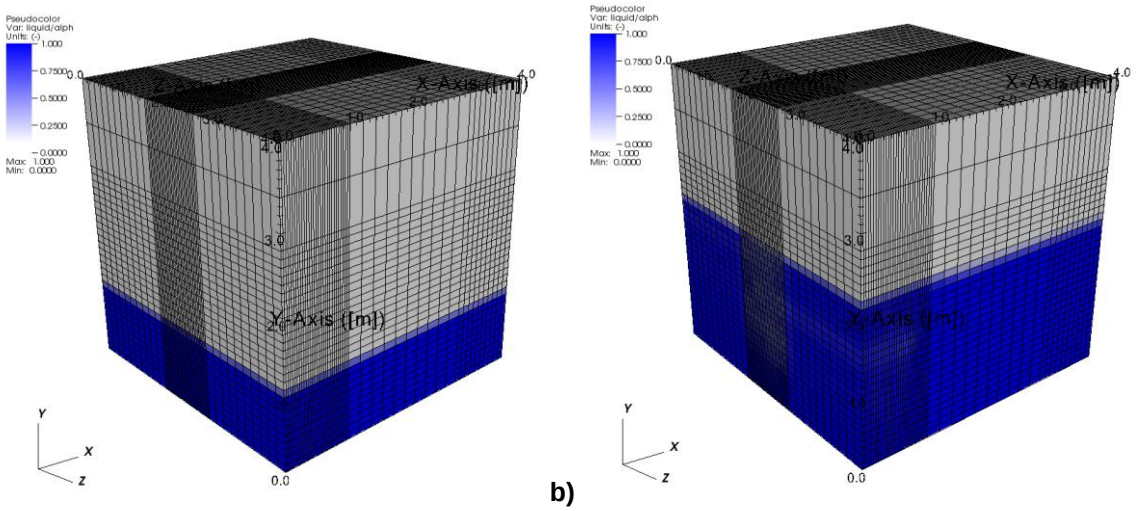

a) b)

Fig. 7-18: **Numerical discretization in explosion calculation performed with IDEMO-3D code for 3D case, three-dimensional view, with water level of 1 m (a) and 2 m (b)**

Figs. 7-19 to 7-24 present the time development of pressure loads and impulses at different heights in the cavity wall in relation to the explosion “epicenter” for the 2D and 3D geometries. In general, higher pressure loads are obtained in all 2D calculations. Table 7-5 shows a tabular overview of the highest pressure loads at the wall and the propagation velocities reached at the water surface in the 2D and 3D calculations. The results show that there is no strong coupling of the propagation velocity and the resulting loads. Rather, a strong confinement induced by geometry (in 2D) of the calculation domain supports stronger explosions due to less pronounced venting effects. Additionally, reflecting waves from the wall are expected to affect each other, leading to unphysical increases and short peaks in pressure loads.

Table 7-5: Comparison of the 3D and 2D explosion results, highest pressure loads at the cavity wall and the resulting propagation velocity

Case	**3D:** highest pressure loads at the wall (propagation velocity)	**2D:** highest pressure loads at the wall (propagation velocity)
#1	8 MPa (325 m/s)	12 MPa (280 m/s)
#2	10 MPa (300 m/s)	16 MPa (280 m/s)
#3	16 MPa (300 m/s)	28 MPa (270 m/s)
#4	16 MPa (300 m/s)	90 MPa (270 m/s)
#5	30 MPa (370 m/s)	50 MPa (380 m/s)
#6	40 MPa (330 m/s)	70 MPa (370 m/s)

The highest pressure loads 70 MPa and 40 MPa (for 2D and 3D, respectively) are obtained in case #6 with the largest ingress of melt into water and a water level of 2 m. The lowest pressure loads 12 MPa and 8 MPa result from configuration #1 with the lowest melt ingress and total fragmented melt in mixture. In configuration #4 with a later MBC, a large pressure peak up to 90 MPa is detected on the floor in the 2D calculations. Here, a rather homogeneous distribution of the fragmented melt in axial direction is obtained due to the later MBC. It is explained by wave reflexions inside the mixing zone and focusing effect on the floor. However, this pressure peak is very short and its contribution to the final impulse is less.

2D, pressure vs. time:

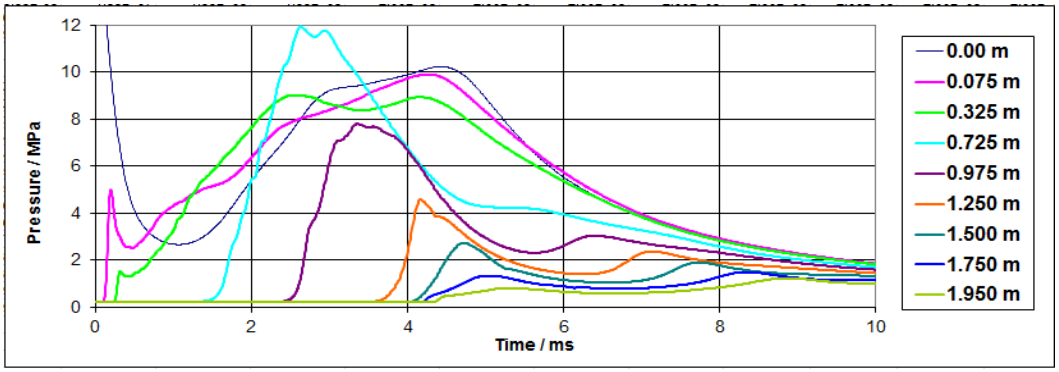

3D, pressure vs. time:

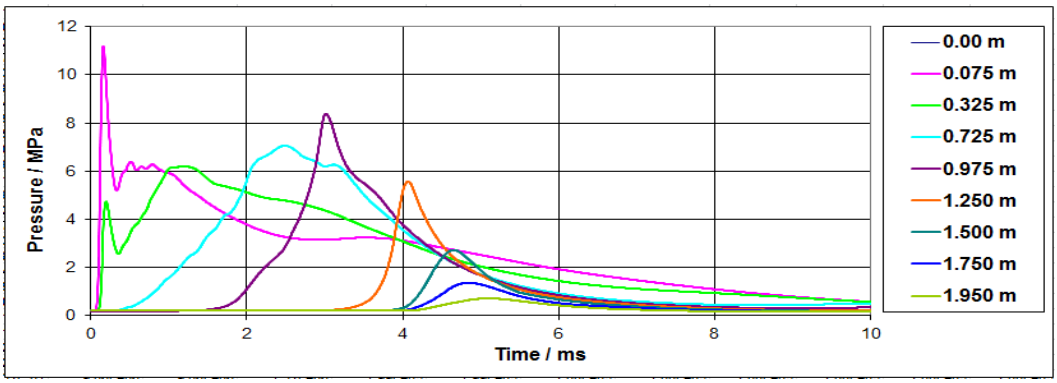

2D, impulse vs. time:

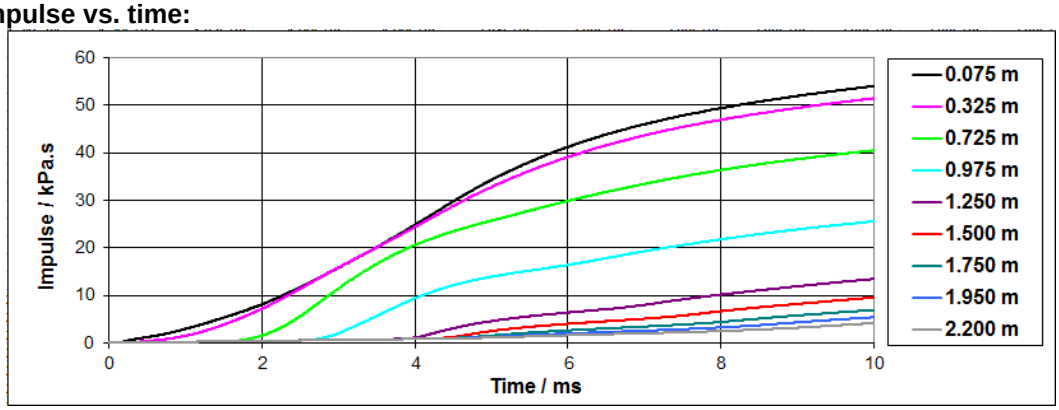

3D, impulse vs. time:

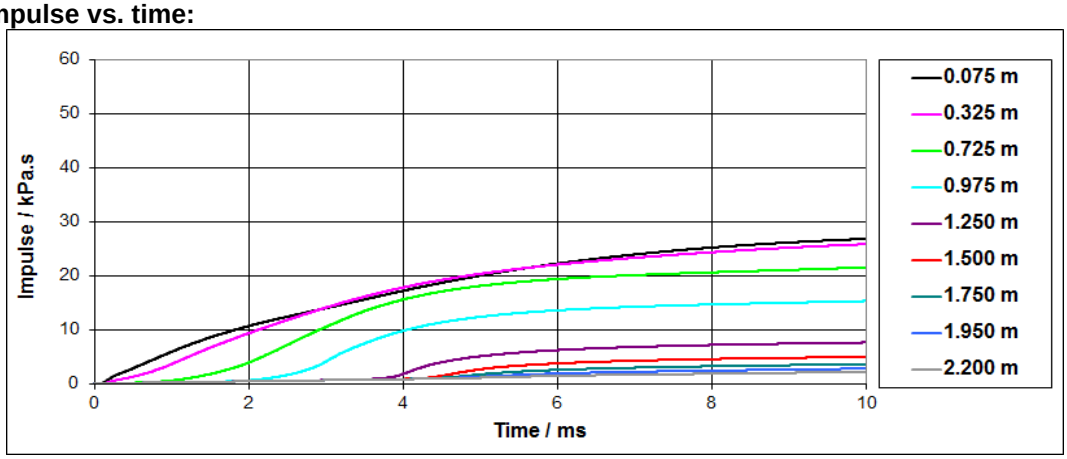

Fig. 7-19: **Pressure vs. time and impulse vs. time at different heights in explosion calculations performed with IDEMO-3D code in 2D cylindrical geometry for central melt outflow and 3D Cartesian geometry with lateral melt outflow, water level 1 m, jet diameter 0.1 m**

2D, pressure vs. time:

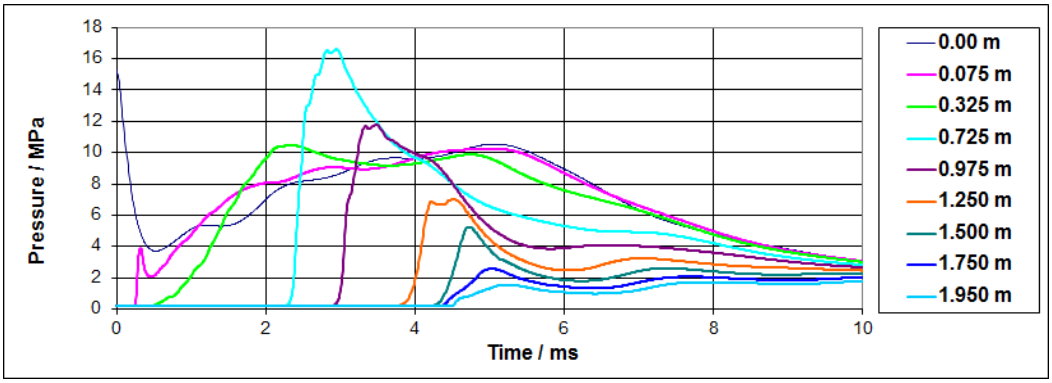

3D, pressure vs. time:

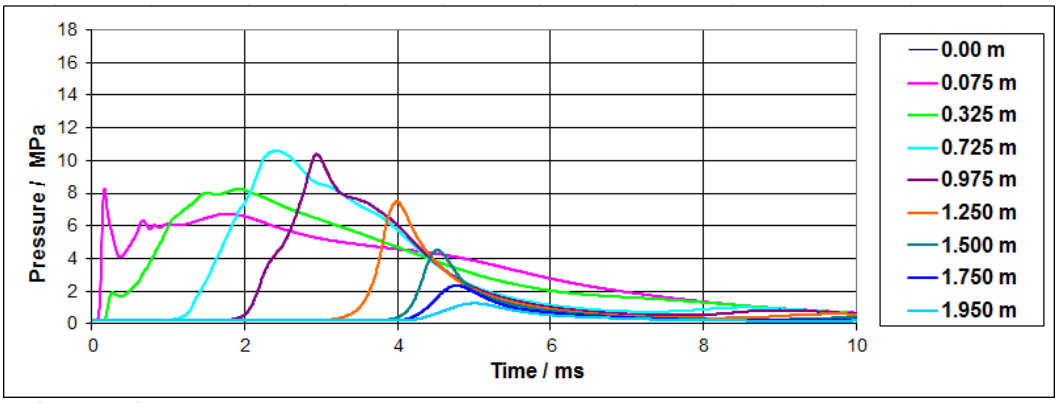

2D, impulse vs. time:

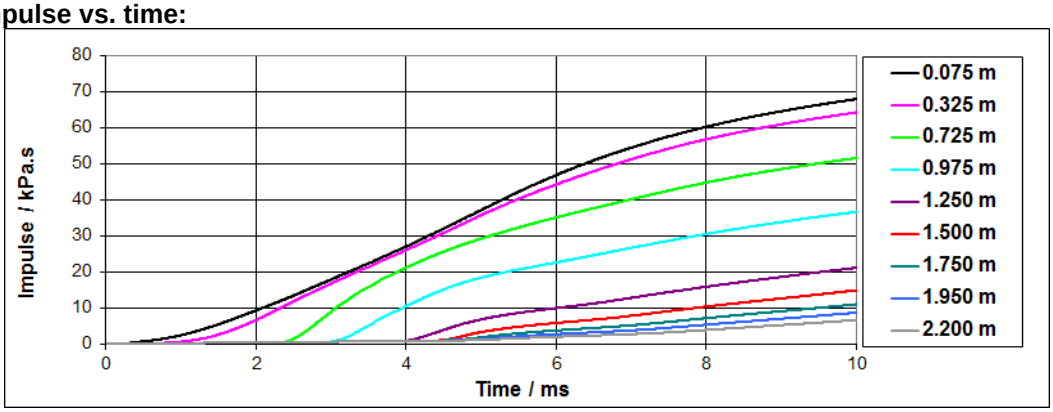

3D, impulse vs. time:

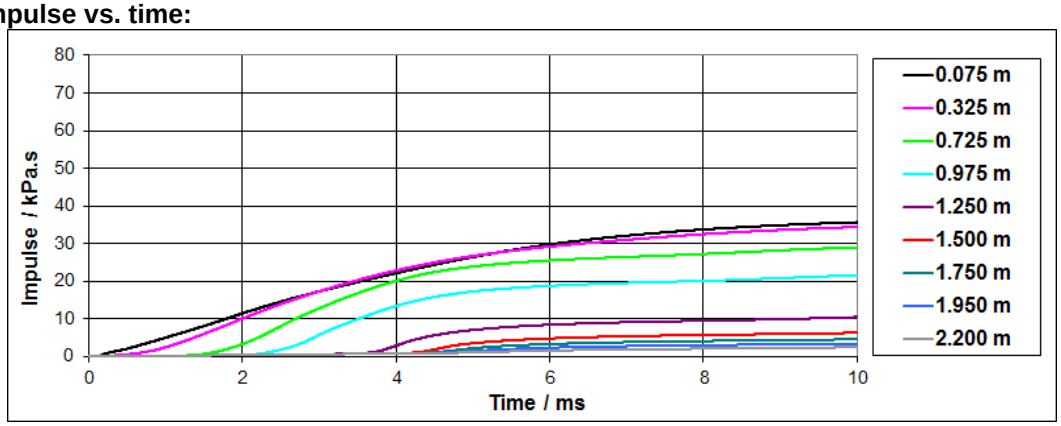

Fig. 7-20: **Pressure vs. time and impulse vs. time at different heights in explosion calculations performed with IDEMO-3D code in 2D cylindrical geometry for central melt outflow and 3D Cartesian geometry with lateral melt outflow, water level 1 m, jet diameter 0.2 m**

2D, pressure vs. time:

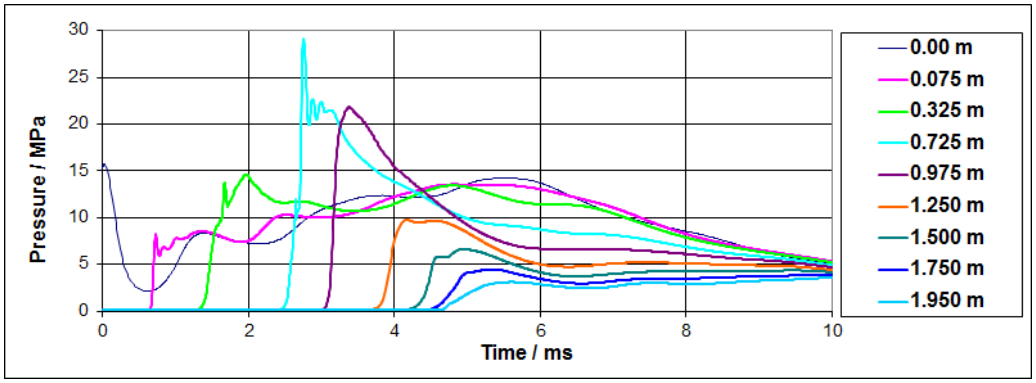

3D, pressure vs. time:

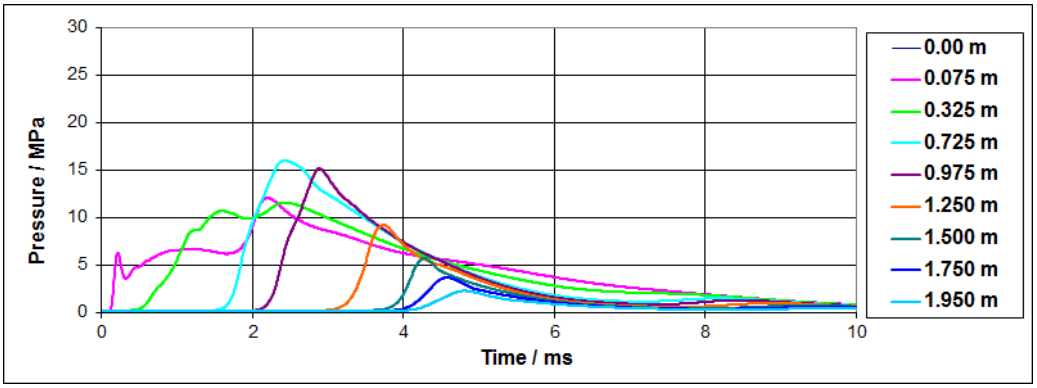

2D, impulse vs. time:

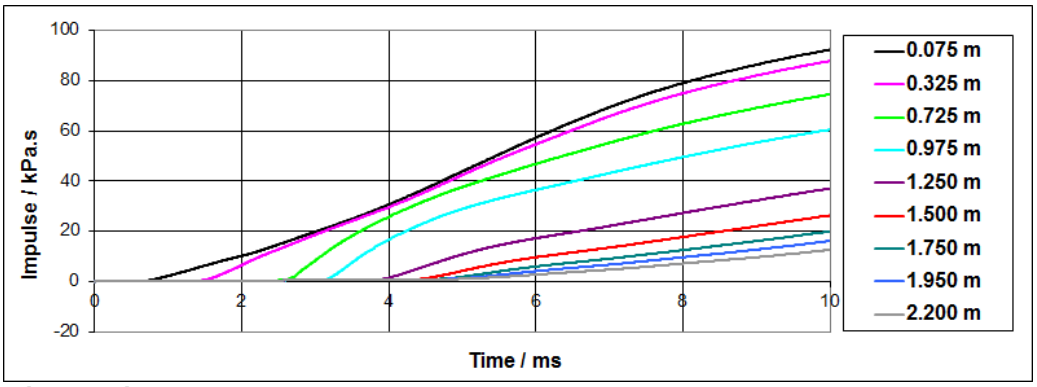

3D, impulse vs. time:

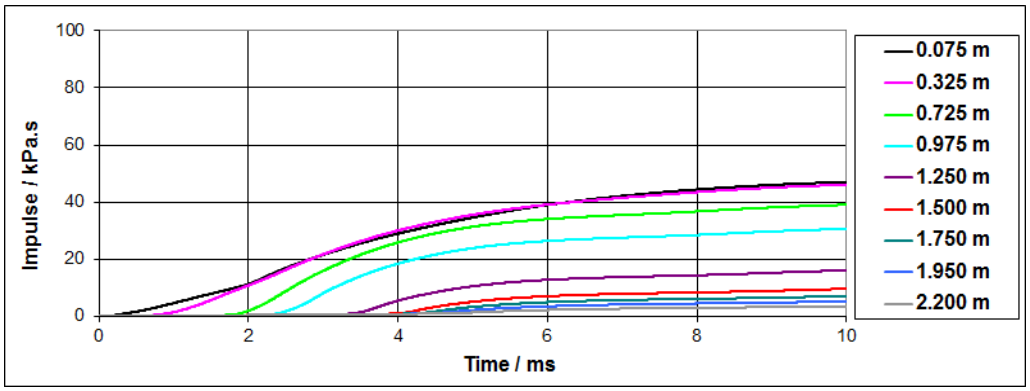

Fig. 7-21: **Pressure vs. time and impulse vs. time at different heights in explosion calculations performed with IDEMO-3D code in 2D cylindrical geometry for central melt outflow and 3D Cartesian geometry with lateral melt outflow, water level 1 m, jet diameter 0.4 m**

2D, pressure vs. time:

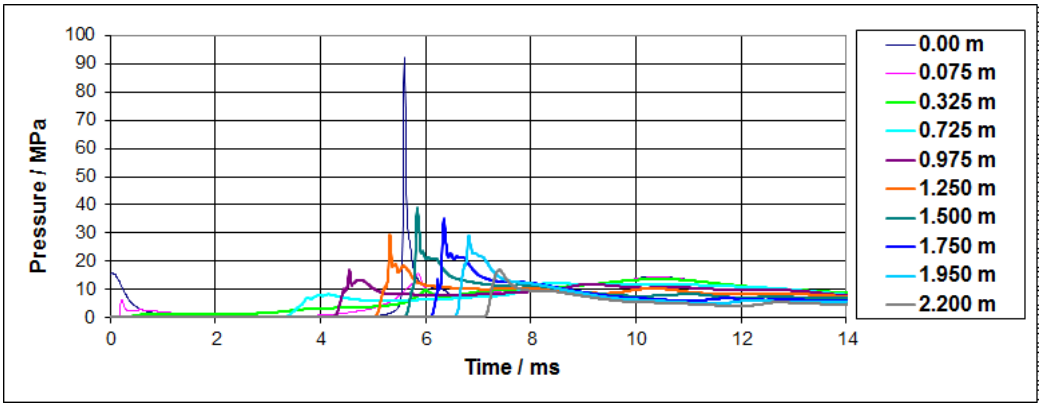

3D, pressure vs. time (changed axial scale):

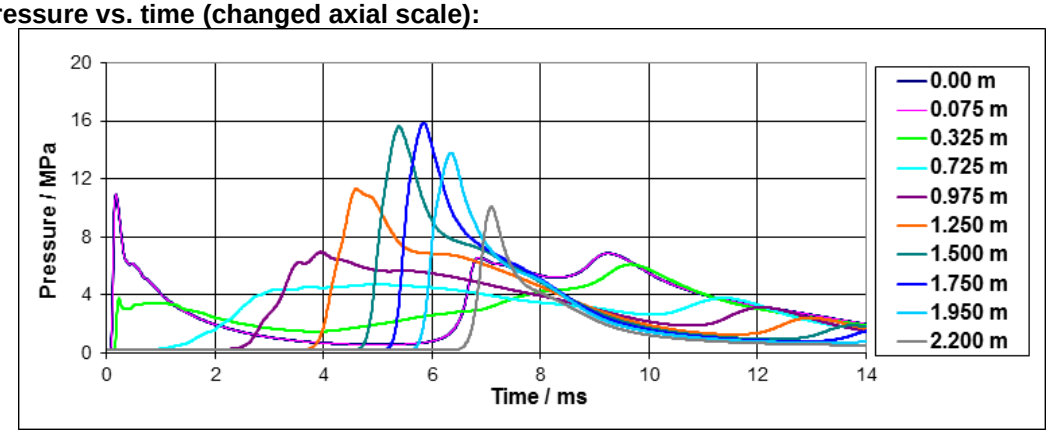

2D, impulse vs. time:

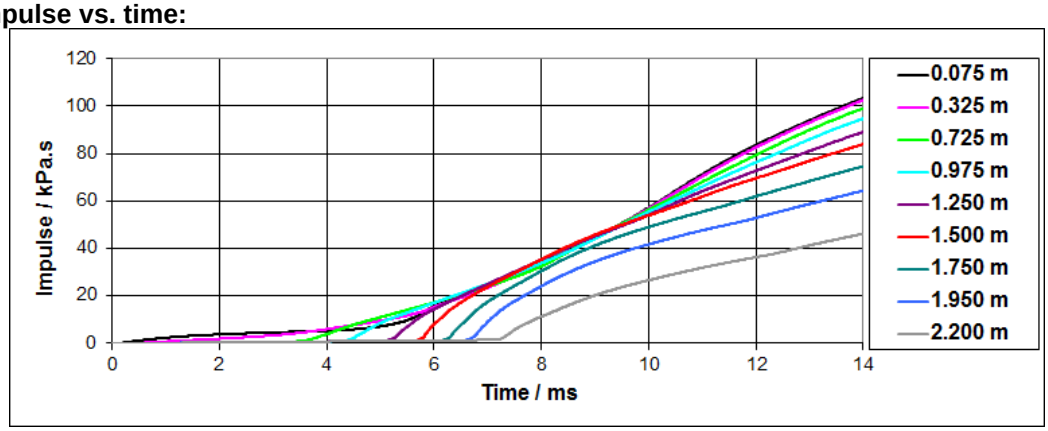

3D, impulse vs. time:

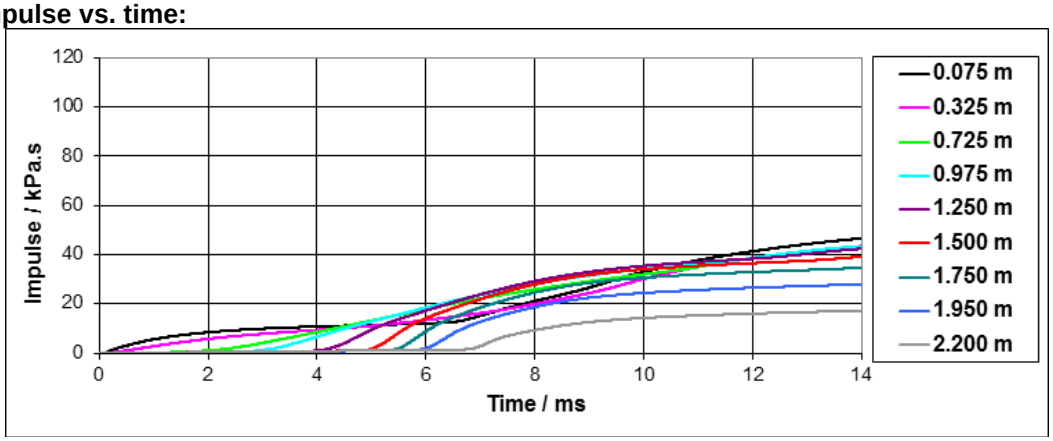

Fig. 7-22: **Pressure vs. time and impulse vs. time at different heights in explosion calculations performed with IDEMO-3D code in 2D cylindrical geometry for central melt outflow and 3D Cartesian geometry with lateral melt outflowwater level 2 m, jet diameter 0.1 m**

2D, pressure vs. time:

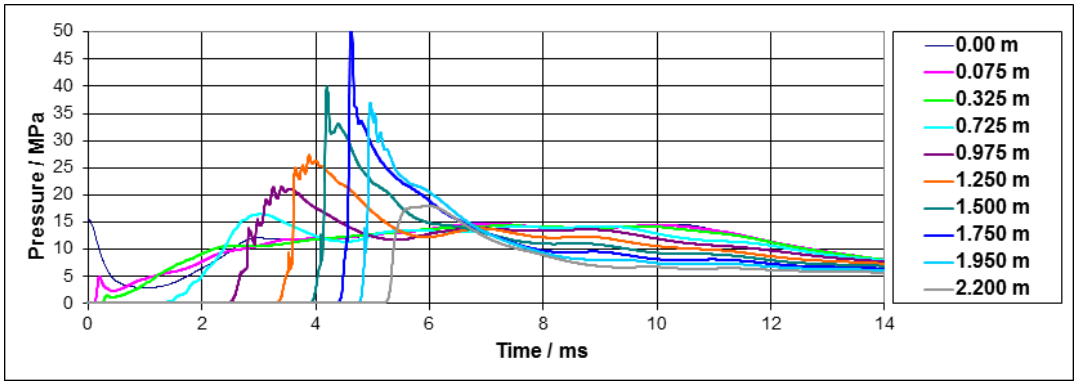

3D, pressure vs. time:

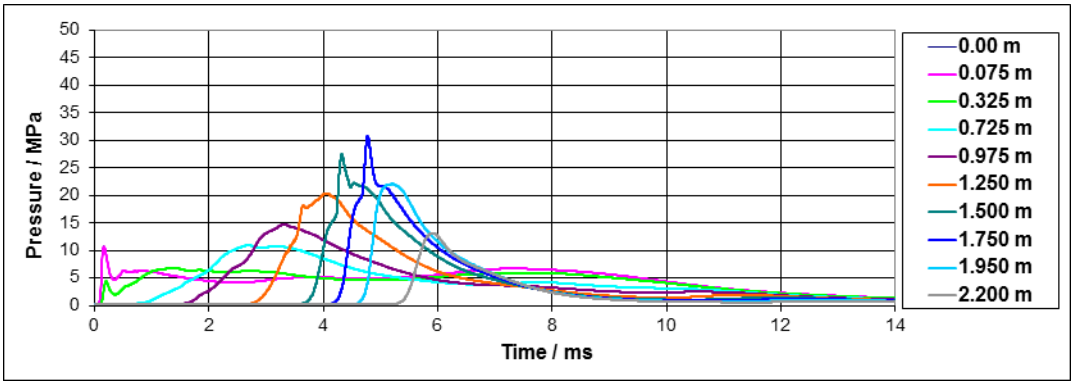

2D, impulse vs. time:

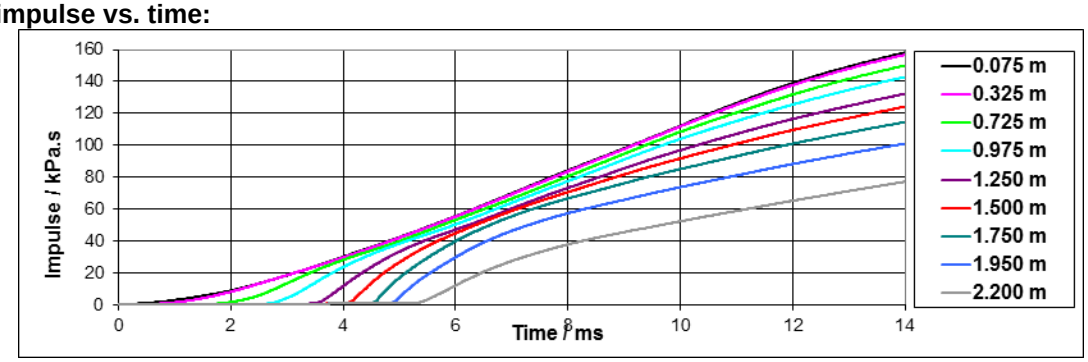

3D, impulse vs. time:

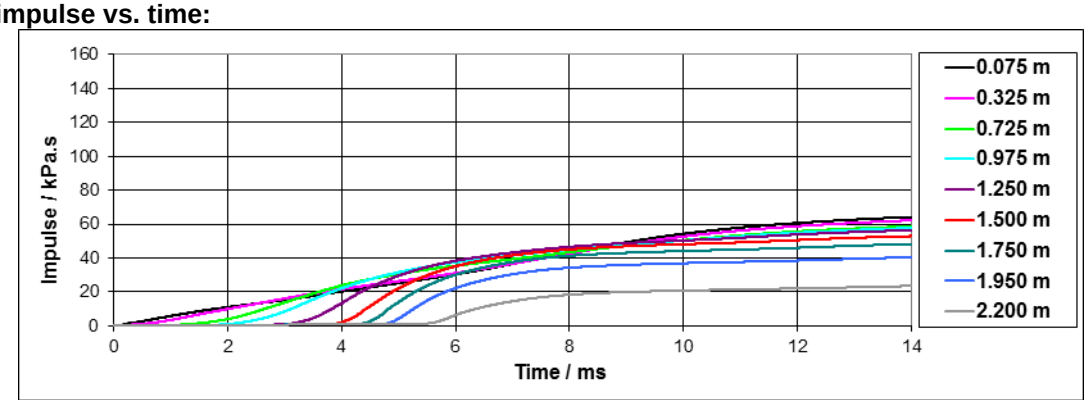

Fig. 7-23: **Pressure vs. time and impulse vs. time at different heights in explosion calculations performed with IDEMO-3D code in 2D cylindrical geometry for central melt outflow and 3D Cartesian geometry with lateral melt outflow, water level 2 m, jet diameter 0.2 m**

2D, pressure vs. time:

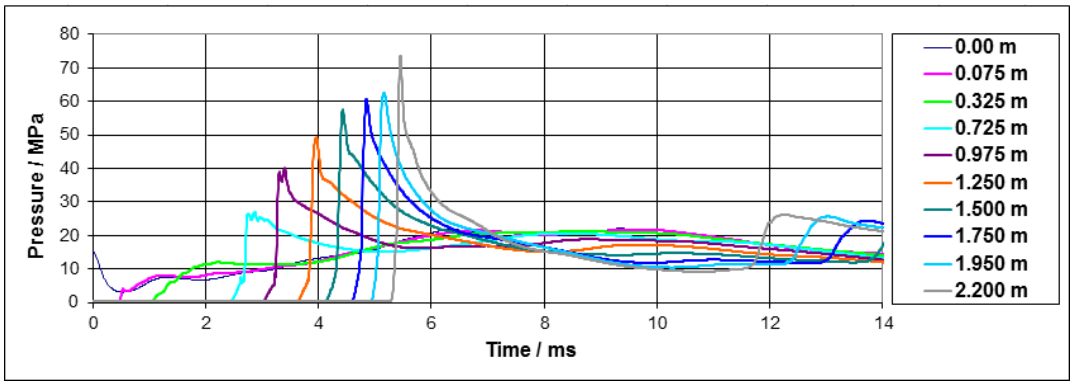

3D, pressure vs. time:

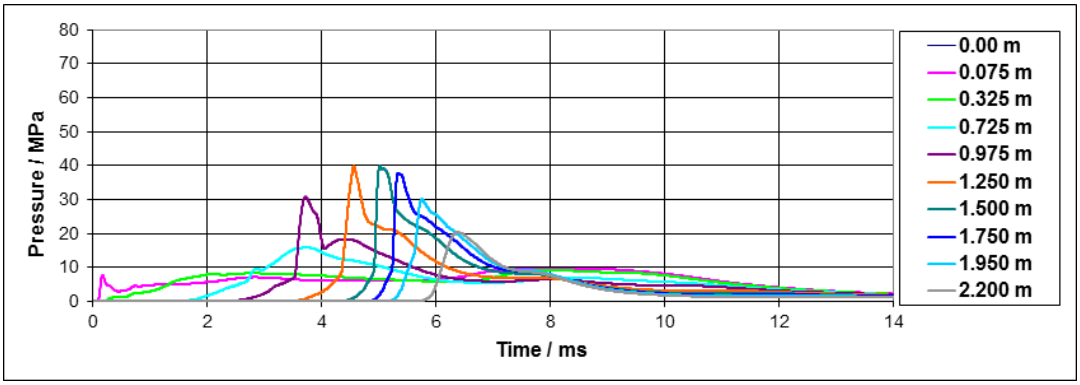

2D, impulse vs. time:

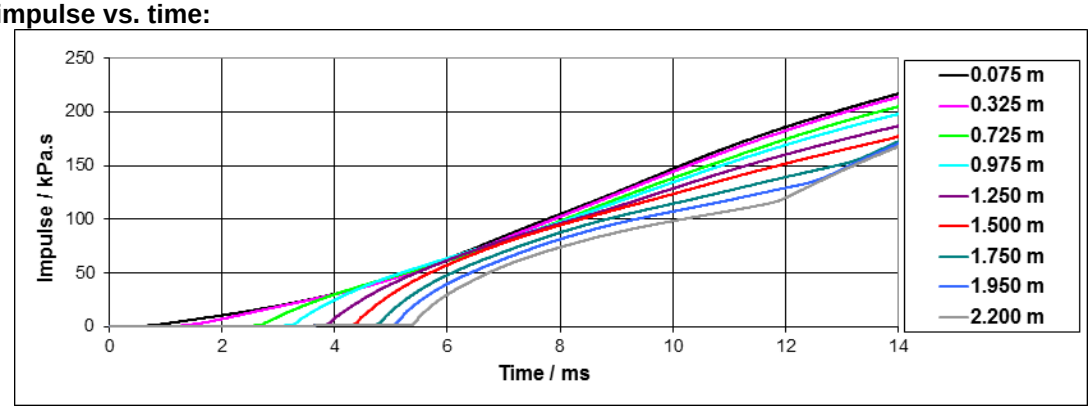

3D, impulse vs. time:

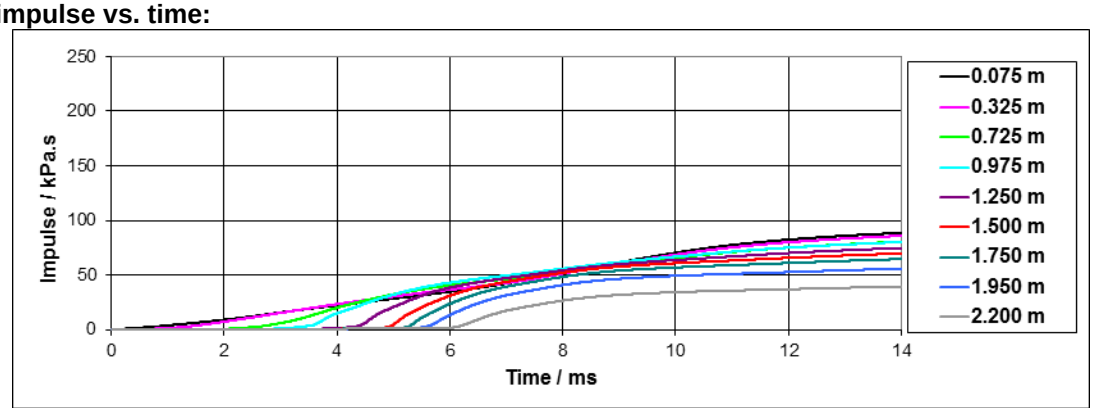

Fig. 7-24: **Pressure vs. time and impulse vs. time at different heights in explosion calculations performed with IDEMO-3D code in 2D cylindrical geometry for central melt outflow and 3D Cartesian geometry with lateral melt outflow, water level 2 m, jet diameter 0.4 m**

Based on the comparison of the two- and three-dimensional calculations, no significant effect caused by asymmetry can be observed during the premixing. A few cases featuring a slightly deformed character are obtained with the largest melt delivery. No large mixture deformation caused by the direct proximity of the cavity wall is observed. The biggest difference is obtained during the explosion. This is mainly due to the confining effect of the 2D cylindrical geometry. Here, pressure waves reflect at the wall and focus back into the mixing zone. This leads to an artificial pressure peak on the surrounding structures. The reflexion effect also causes significantly higher pressure impulses in 2D than those in 3D by approximately a factor of 2. In 3D, no strong confining effect is obtained due to existence of the water-rich region. The pressure wave reflexion plays a minor role during pressure increases in the asymmetric configurations.

7.2 Further reactor scenarios

Cases with one single asymmetric jet have not shown a strong 3D effect expected in proximity to constraining structures. In order to investigate the impact of strong asymmetry on the steam explosion strength, an initially asymmetric configuration is built. A non-symmetric ex-vessel reactor scenario is assumed with a multiple melt outflow from the reactor vessel close to the cavity wall. Such scenarios have been considered as critical with respect to resulting pressure loads on the structures challenging their integrity [62]. The configuration postulates an ex-vessel accident scenario with an RPV breaking circumferentially due to thermal loads and lateral corona-like melt outflow into the reactor cavity filled with saturated water. Large amounts of melt are then mixing spatially, distributed by multiple outpourings. Strong steam explosions can be the result, due to the large melt mass and limited void. The limitation of the steam content in the mixture is obtained by an initially better melt distribution due to an initially larger reach of the melt outflow. The aim of this investigation is to get a large amount of fragmented melt into the water and also to assess the explosiveness of the extended mixture in view of the melt and void interrelation.

Fig. 7-25 schematically shows the considered scenario. Five melt jets close to each other pouring from the RPV into the cavity with a radius of 2 m filled with saturated water with a system pressure of 0.2 MPa are assumed. The wall proximity is considered as in the previous investigation: 0.4 m from the wall to the outflow axis. The initial conditions are given in Table 7-1. The mass flow rate is considered as 940 kg/s: five melt jets each with 188 kg/s. Two different water pool depths are assumed: 1 m and 2 m. The triggering time is set at the melt bottom contact.

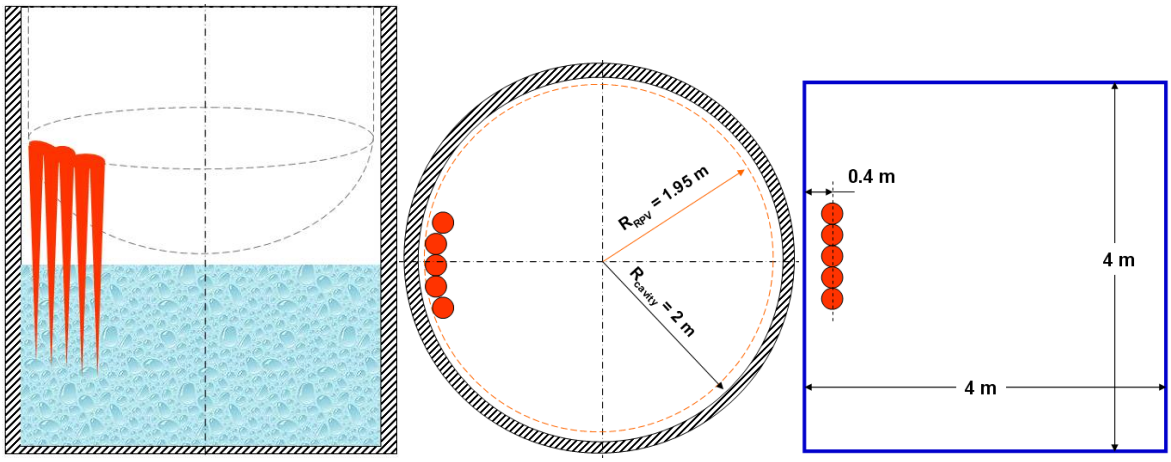

Fig. 7-25: **Schematic illustration of ex-vessel case with lateral corona-like melt outflow from the RPV into the reactor cavity filled with water; front, top and simplified views.**

Table 7-6: **Overview of the premixing results obtained with 3D code JEMI in 3D Cartesian geometry for asymmetric melt outflow**

		Water level = 1m	Water level = 2m
Configuration		5 jets	5 jets
Djet	m	0.1	0.1
Melt bottom contact	s	0.45	0.67
Mass flow rate (5 x 188)	kg/s	940	940
Dp (mass mean)	mm	3.8	3.8
Dp (Sauter mean)	mm	3.5	3.6
Total mass in mixture	kg	60 (100%)	**428** (100%)
Mass in mixture with void less than 30%	kg	4 (7%)	**5** (1%)
Mass in mixture with void less than 40%	kg	5 (8%)	**18** (4%)
Mass in mixture with void less than 50%	kg	10 (17%)	**54** (13%)
Mass in mixture with void less than 60%	kg	24 (40%)	**116** (27%)

The premixing results are given in Table 7-6. The yielded drop size varies in both configurations between 3.5 and 3.6 mm (Sauter mean). The total mass of fragmented melt in mixture is 60 kg for a water level of 1 m at the time 0.45 s and 428 kg with a water level of 2 m at the time 0.67 s. Comparing with single jet configurations in Table 7-3, there is a significantly higher melt mass becoming fragmented in the mixture with a lower mass flow rate, e.g. configuration #3 and #6 from Table 7-3. This is due to a higher fragmentation rate, since a greater effective fragmentation surface area results from using multiple jets.

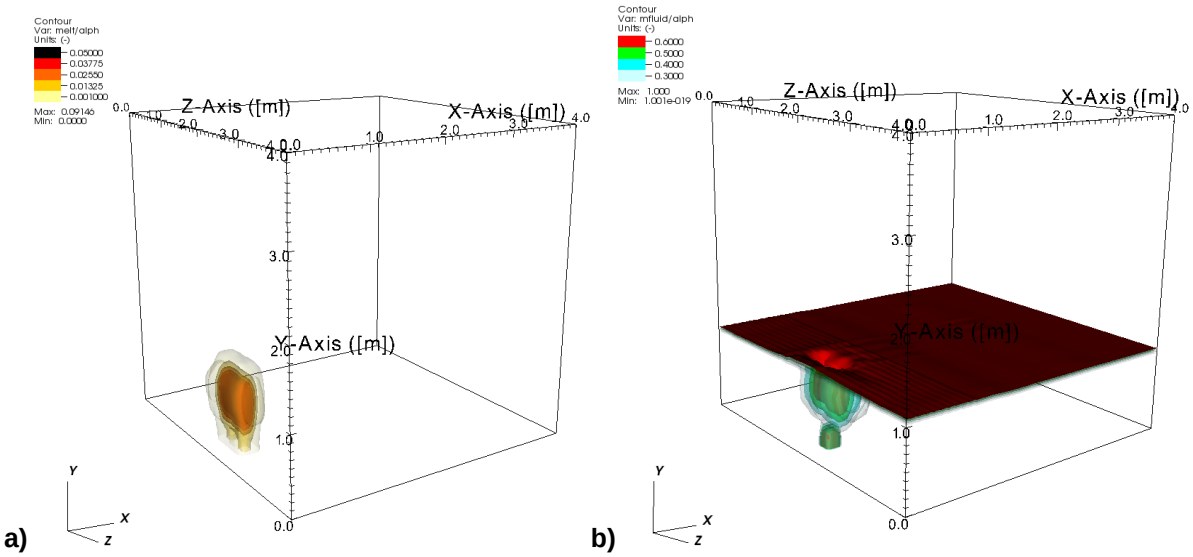

Fig. 7-26: **Contoured board of volume fraction of melt (a) and void (b) at the MBC calculated in JEMI, three-dimensional view, five melt jets with diameter of 0.1 m and water level of 1 m**

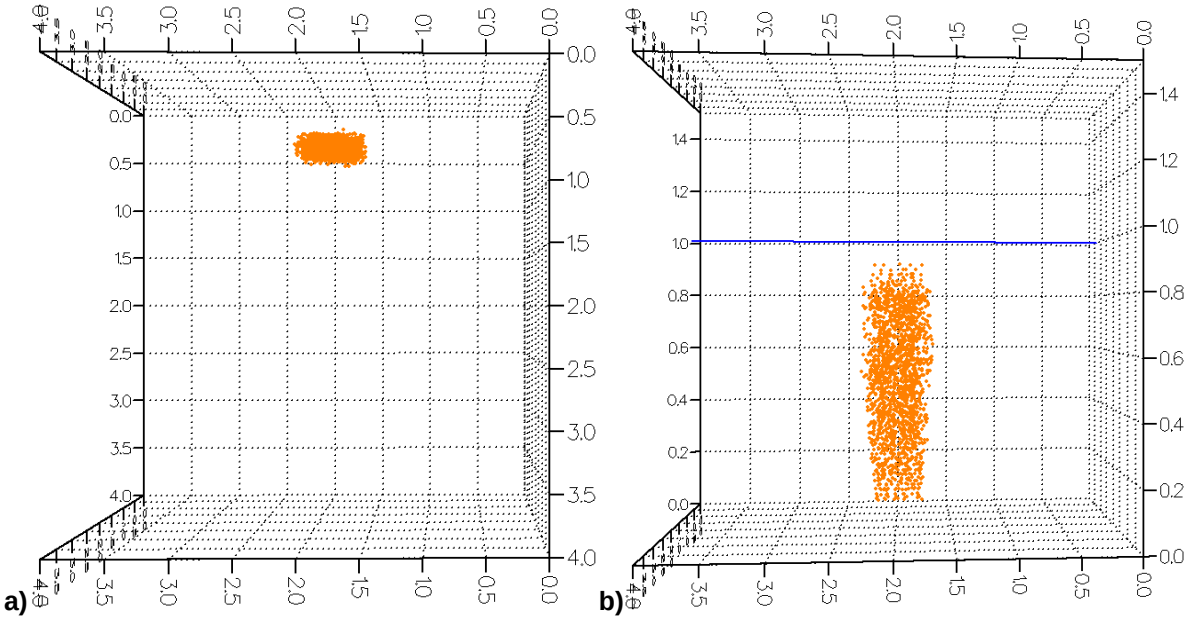

Fig. 7-27: **Representative distribution of melt drops at the MBC calculated in JEMI, (a) top view and (b) side view, three-dimensional view, five melt jets with diameter of 0.1 m and water level of 1 m**

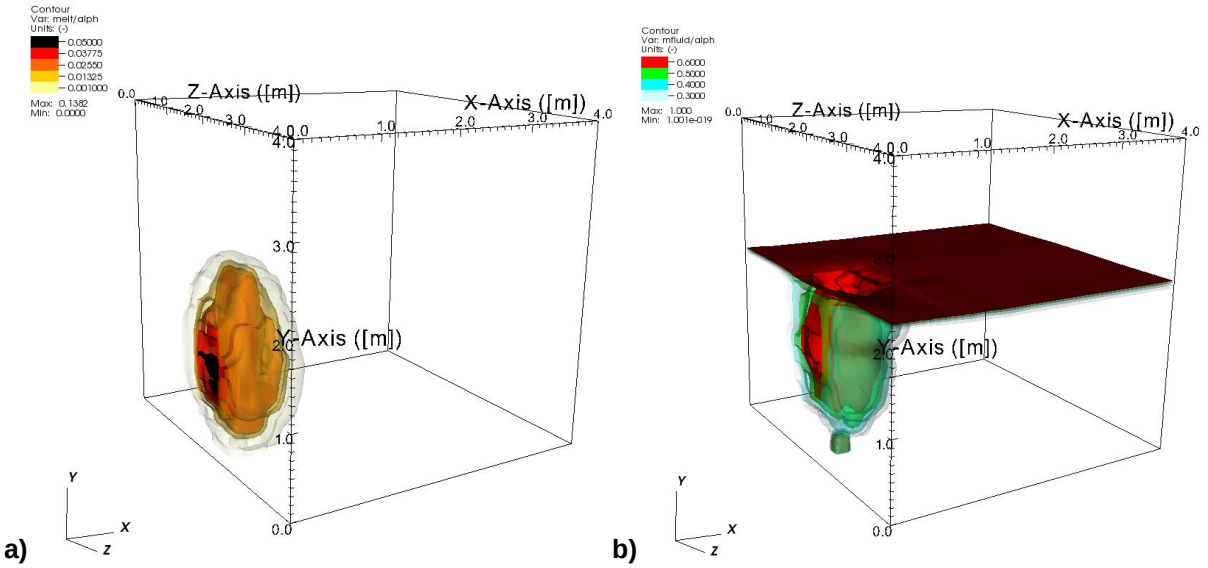

Fig. 7-28: **Contoured board of volume fraction of melt (a) and void (b) at the MBC calculated in JEMI, three-dimensional view, five melt jets with diameter of 0.1 m and water level of 2 m**

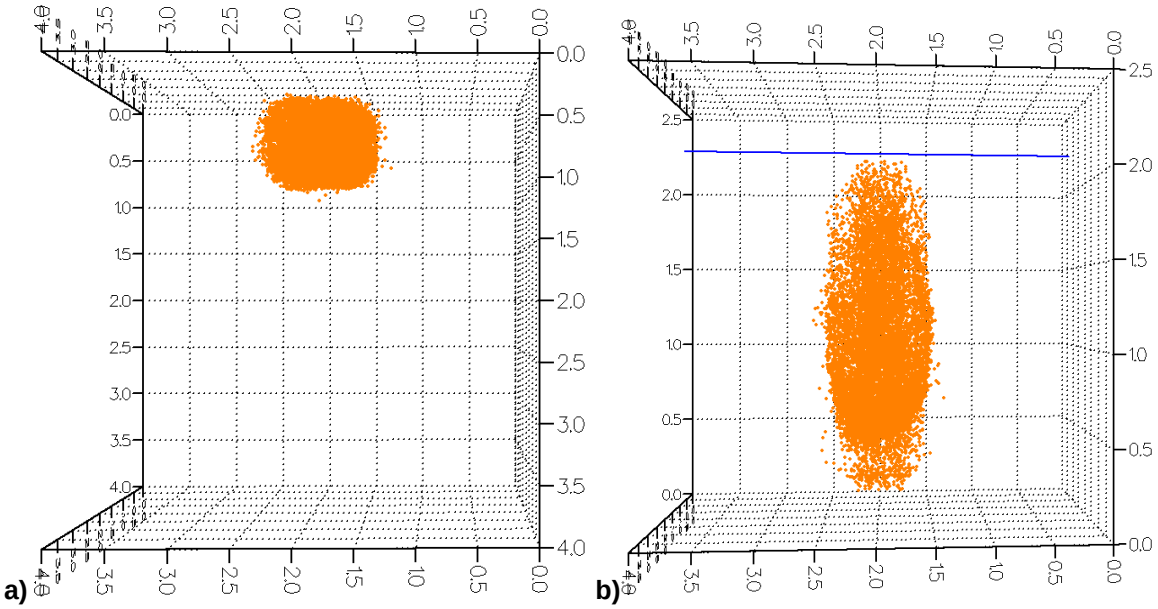

Fig. 7-29: **Representative distribution of melt drops at the MBC calculated in JEMI, (a) top view and (b) side view, three-dimensional view, five melt jets with diameter of 0.1 m and water level of 2 m**

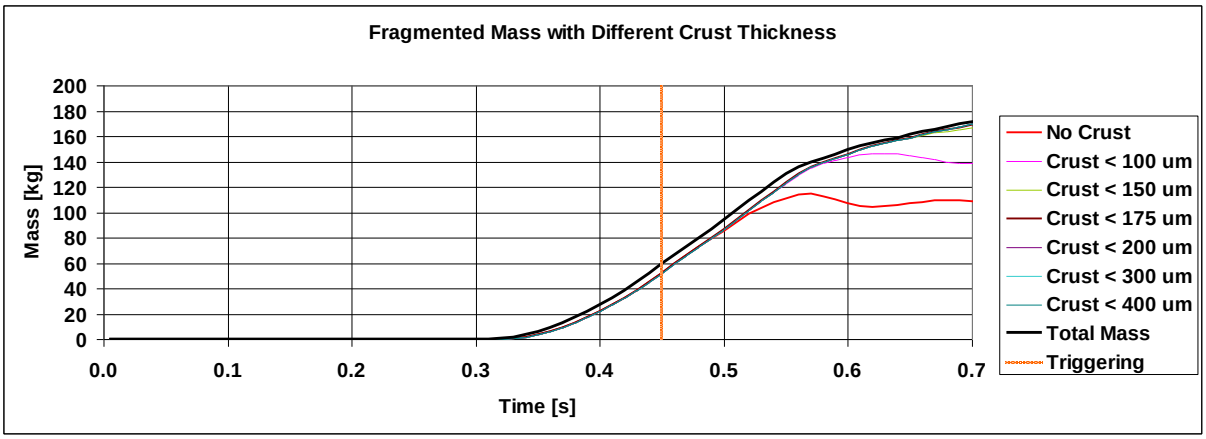

Fig. 7-30: **Fragmented melt mass in regions with different crust thickness in 3D calculations performed with JEMI code, water level = 1 m, 5 lateral jets with D_{jet} = 0.1**

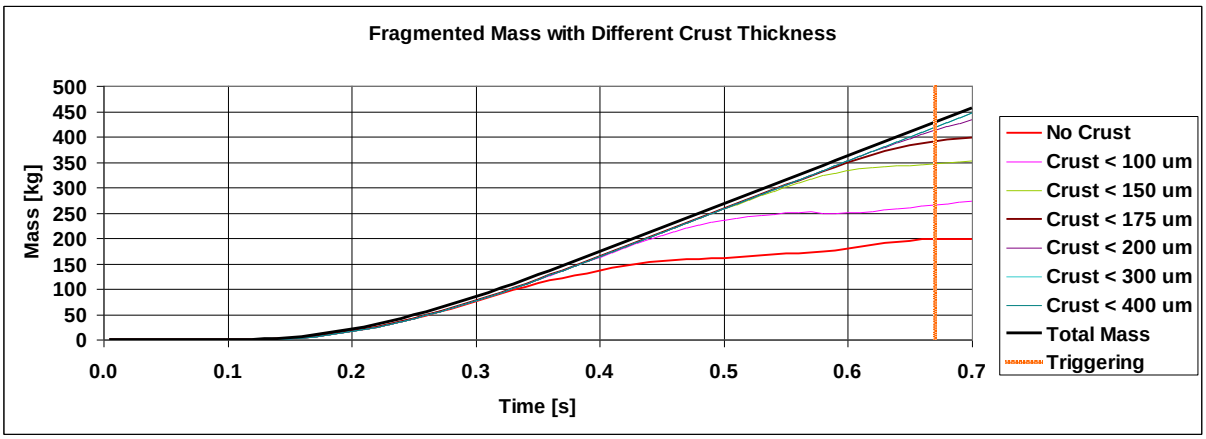

Fig. 7-31: **Fragmented melt mass in regions with different crust thickness in 3D calculations performed with JEMI code, water level = 2 m, 5 lateral jets with D_{jet} = 0.1**

Another important characteristic is the proportion of void in the mixture. Due to the relatively dense melt outflow, only 40% and 30% of the total melt mass stays in regions with void below 60%, which is assumed to be a physical limitation for pressure increases and propagations during the explosion phase. The high steam content is explained primarily by the overlapping of the existing mixing zones leading to high melt concentrations in the space between the jets and intense vaporization of these regions.

The radial extent of the mixture caused by asymmetry is observed only in the configuration with the deeper water pool of 2 m due to later triggering and thus longer mixing times. While the “shallow” configuration, Fig. 7-27, shows a distinctive stretched form defined initially, the “deeper” case shows a nearly round form. The high melt concentrations at the wall and between the jets produce a high void, which leads to a pressure buildup in these regions displacing the melt clouds into water-rich

regions besides. This effect is particularly notable in the central region at the wall where it is arrested by the boundary jets. The void there can only escape in axial direction without extending along or from the wall. The local high void fraction and pressure buildup at the wall press the melt and void clouds away from the wall and extend the mixture. The mixture, initially stretched, becomes rather circular.

Further, Figs 7-30 and 7-31 show the solidification of the fragmented melt mass on a large time scale. The melt drops are apportioned according to different crust thicknesses. This shows, that the solidification occurs only in the configuration with a later triggering time of 0.67 s due to longer periods in the water (earlier melt water contact due to higher water level and shorter falling time in gas) ~0.5 s in contrast to 0.12 s. 250 kg of fragmented melt is still liquid or without crust of the total melt mass in the mixture of 428 kg. Here, the formation of crust at the droplet surface is expected to have a limiting effect on fine fragmentation in the explosion stage, thus reducing the total melt mass participating in the pressure escalations.

Figs. 7-32 and 7-33 show the development of pressure and impulse at different heights along the cavity wall. Higher pressure loads up to 65 MPa are obtained in the configuration with a higher water surface and larger fragmented melt compared to 20 MPa in the “lighter” configuration. While the melt mass in the mixture with a void fraction below 30% is nearly the same ~5 kg (see Table 7-6), significantly larger melt masses are obtained especially in the mixture regions with higher voids: between 30% and 60% and above. This leads to higher but shorter pressure peaks: higher due to a larger melt mass and shorter due to a higher void. The resulting impulses differ only by a factor of 2: 100 kPa s to 50 kPa s. This is as mentioned due to the higher but shorter pressure peaks resulting from a higher void fraction caused by a larger melt mass. The highest impulse 100 kPa s is only slightly higher than the impulse in the configuration #6 with the largest single melt pour into a 2 m-deep water pool, see Fig. 7-24.

3D, pressure vs. time:

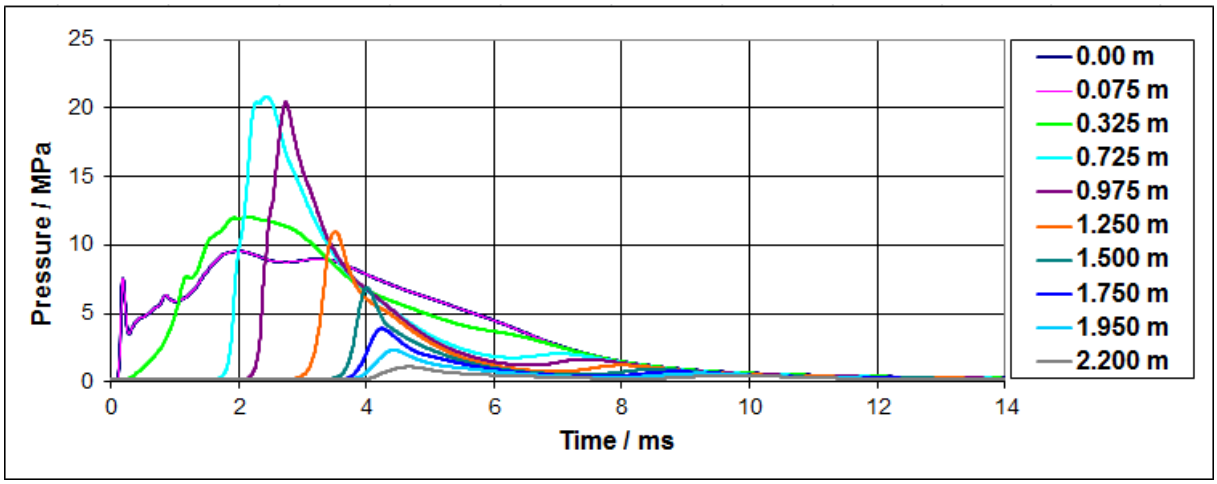

3D, impulse vs. time:

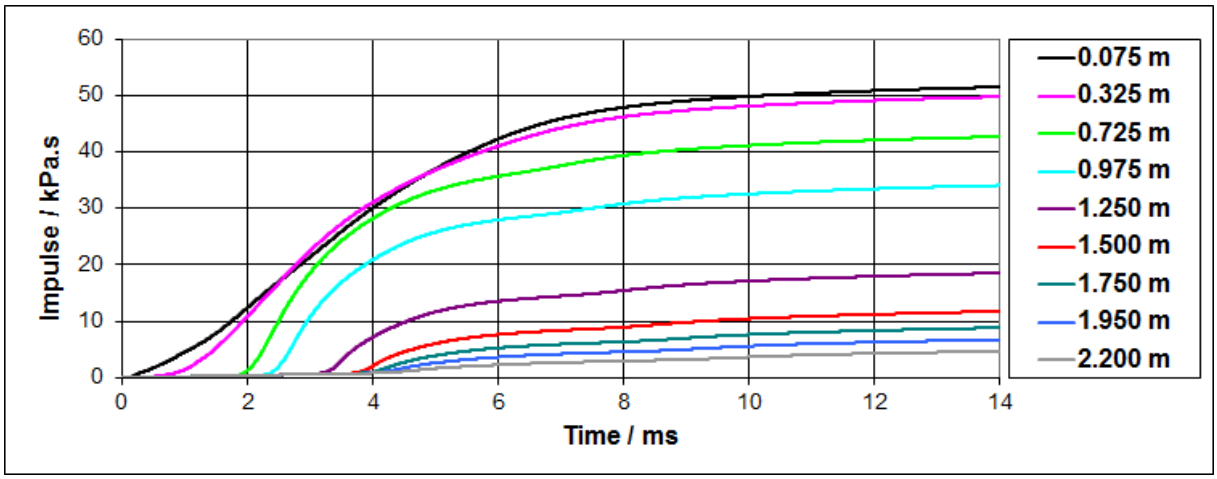

Fig. 7-32: **Pressure vs. time and impulse vs. time at different heights in explosion calculations performed with IDEMO-3D code in 3D Cartesian geometry with lateral multiple melt outflow, water level 1 m, jet diameter 0.1 m**

3D, pressure vs. time:

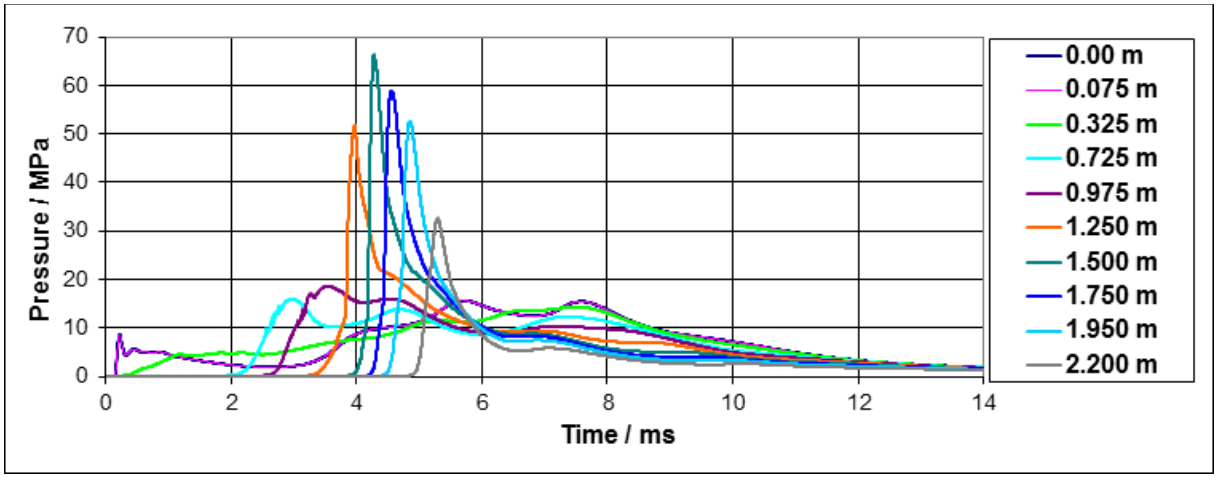

3D, impulse vs. time:

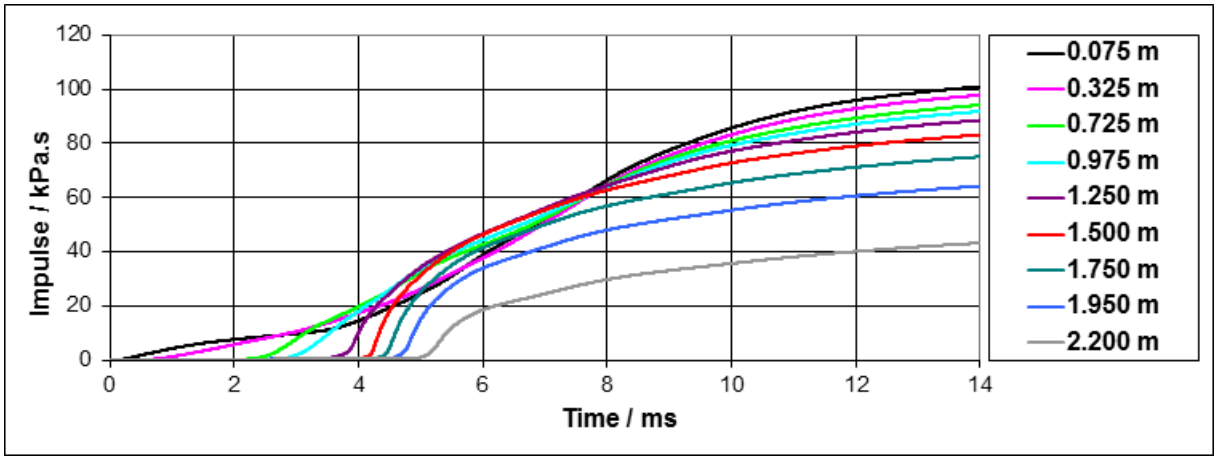

Fig. 7-33: **Pressure vs. time and impulse vs. time at different heights in explosion calculations performed with IDEMO-3D code in 3D Cartesian geometry with lateral multiple melt outflow, water level 2 m, jet diameter 0.1 m**

7.3 Discussion

Premixing and explosion calculations are performed with the three-dimensional codes, JEMI and IDEMO-3D, for non-symmetric ex-vessel reactor scenarios. The aim was to assess the effect of the asymmetry on the mixing of fragmented melt and coolant, steam production and explosion strength in non-symmetric scenarios. Here, the proximity of structures, e.g. the wall of the reactor vessel or reactor cavity, was of special interest, since they may be susceptible to damage by pressure increases in case of vapor explosions.

To investigate such configurations, an ex-vessel scenario with a single melt pour close to the wall of the reactor cavity has been considered. The water pool depth and the melt flow rate have been varied. The depth of the water pool defines the axial extension of the mixture and the duration of the premixing phase before the melt-bottom contact. The melt flow rate determines the mass of melt that can be fragmented from the jet and participates in the explosion. In order to assess the 3D effect, i.e. impact of the nearest wall, on the mixture extension and its explosiveness, 2D and 3D calculations have been performed. The 2D calculations are performed using 2D approximations: an axis-symmetric melt pour into a water pool. The radial extension of the calculation domain has been chosen considering the “average” mixture, i.e. steam content and radial spreading of the melt. Two different domain sizes are considered for 2D: with a radius of 1 m for premixing and 0.4 m for explosion. The smaller domain size in the explosion phase is considered according to the minimal distance between the melt jet and the wall. In the investigation to the premixing phase, the 2D and 3D calculations have shown a good agreement in the results, see Tables 7-2 and 7-3. It is due to a symmetric mixture extension and insignificant 3D effect of the wall. Only in the cases with the largest melt delivery, higher melt concentrations did occur at the wall side compared to other boundary regions. However, the pressure buildup in regions with significant melt concentrations was too small to strongly displace the high dense corium drops. The void migration from highly concentrated regions occurs dominantly in axial direction.

The melt bottom contact is assumed as the most likely triggering time for a vapor explosion. The explosion calculations with the obtained premixing data showed that the vapor explosion strength is slightly overestimated by using two-dimensional approximations. It shows significantly higher pressure peaks in 2D. This fact is explained by wave reflexion inside the mixing zone and focusing on the floor, resulting in reinforcing and escalating effects. However, the pressure peaks are very short contributing weakly to the final impulse. In conclusion, the 2D approximations show a satisfactory capability to predict the melt fragmentation in the water, the distribution of fragmented melt, the solidification of melt drops and void production even for markedly asymmetric reactor scenarios. Furthermore, no strong 3D effect has been observed in the comparison calculations, even with a distinctive three-dimensional character. Comparing with the results obtained by Vujic [77] in the

investigations of similar reactor conditions, it can be concluded that pressure loads have been generally underestimated by Vujic. This is primarily explained by differences in modeling the jet breakup yielding smaller fragments and significantly denser mixture with high melt and void concentrations, which counteract pressure increases in [77]. In addition, dense mixtures obtained in the previous investigations are generally questionable, since the jet fragmentation process would be chocked in reality due to very high melt fractions adjacent to the jet reducing the hydrostatic head inside the mixture. Thus, such high void fraction as obtained in [77] would entail very intense void production. This then requires again a certain water content in the mixture.

The investigation accomplished showed that no significant 3D effect has occurred. Hence, further asymmetric configurations have been considered, in order to attain asymmetric effects typically for a 3D reactor case. A non-symmetric ex-vessel reactor scenario has been constructed assuming a multiple melt outflow from the reactor vessel close to the cavity wall. The scenario postulates an ex-vessel accident scenario with an RPV breaking circumferentially due to thermal loads and lateral corona-like melt outflow into the reactor cavity filled with saturated water. The configuration means the delivery of a large amount of melt available for mixing by multiple outpourings. This provides significant masses of fragmented melt distributed in water with limited void fraction. The initial melt distribution due to the melt outflow extending azimuthally in the initial phase provides a limitation of steam content in the mixture. Such scenarios were considered as being a critical concern for pressure loads on the structures and as a challenge to integrity [62]. The aim of this investigation is to get a large amount of fragmented melt into the water and to assess the melt-coolant interaction and the explosiveness of asymmetrically extended mixtures. Two configurations have been considered by varying the water level in the reactor cavity: 1 m and 2 m. Melt delivery has been assumed as 940 kg/s portioned into five single melt outpourings aligned in contact. The principal consequence of the multiple outflows in the premixing calculations was significantly higher fragmented melt mass compared to the configurations with a single melt jet with nearly similar melt delivery. This effect is the result of partitioning the melt inflow into five equal melt jets that increases the total strip-off surface area of the inflowing melt. The aligned melt outflows by fragmenting provide a dense mixture with a high fraction supporting the void production, especially in regions between the jets. The consequence is a quicker voiding of the mixing zone, a higher steam content in the mixture and a lower melt fraction (in relation to the total mass) in the regions with void below 60%, in comparison to the single jet cases. However, the multi-jet configurations have showed higher fragmented melt masses with limited void fraction than the single jet ones, in absolute terms. This means more melt is available for fine fragmentation supporting stronger vapor explosions. The explosion calculations based on the data from premixing have confirmed the assumption of higher pressure loads due to more melt mass being available with limited void fraction. However, the pressure peaks are

here shorter than those with a single jet, following generally higher void fractions in the mixture and a very small melt fraction percentage in regions with void less than 30% and 40%, see Table 7-6. The maximal pressure impulses correlate with the single jet configuration with jet diameter of 0.4 m.

Initially, the multi-jet cases are markedly three-dimensional and thus impossible to describe in a two-dimensional approach. The 3D effect caused by the cavity wall is only observed by later triggering when the water pool depth is 2 m. A later triggering causes a longer mixing time. Intense steam production and local pressure buildup displaces the melt fragments radially, in fact from the central mixing zone to the water-rich region. No azimuthal mixture extension along the wall takes place. The radial extension gives the mixture (initially distributed along the wall) a nearly round form. Taking into account the melt delivery into the water, significantly higher pressure loads have been obtained in the multi-jet cases. Considering higher void in the mixture on average and higher fragmented melt masses, the melt fragmentation during the premixing phase is felt to be a cause for that stronger explosion. The partitioning of the melt delivery by multiple sources provides a better (mass-richer) jet breakup and more fragmented melt in the mixture which is then available for fine fragmentation during the explosion phase.

The present 3D results (single and multi-jet) agree with indications from the investigations of Esmaili on ex-vessel fuel coolant interaction energetics for AP1000 [89]. The calculations have been performed using the two-dimensional premixing PM-ALPHA [31] and explosion ESPROSE.m [32] computer codes. For the base case, a failure of the RPV lower head with a break size of 0.4 m in diameter is assumed. The outflow rate is 1709 kg/s. The particle diameter is set to a constant value of 10 mm. The water is subcooled by 30 K. The explosion is triggered on the bottom at 1 s of premixing time. The calculations yield maximum pressure loads at the cavity wall of up to 90 MPa. The decreasing of the drop size has resulted in higher steam generation and voiding of the mixture region. The high void limits the explosiveness of the mixture and leads to weakening of the resulting pressure loads.

8 Summary and conclusion

The purpose of this thesis has been to extend the existing two-dimensional premixing and explosion models IKEJET/IKEMIX and IDEMO to 3D and to investigate the effect of asymmetry during a severe accident with steam explosion in a Light Water Reactor (LWR). A steam explosion may occur during a severe accident in LWR's with core melting as a consequence of the interaction of molten core materials with water, inside the reactor pressure vessel (RPV) or outside the RPV in the reactor cavity which is likely to be filled with water. Such steam explosions may significantly enhance the risk of a severe accident, challenging the integrity of the surrounding structures such as the reactor pressure vessel, the primary containment and possibly even of the reactor building. The loss of the primary containment integrity as a result of an ex-vessel steam explosion will cause a release of large amounts of fission products into the atmosphere and contamination over a large area. Measures to alleviate the consequences, to inhibit or even to prevent the vapor explosions must be investigated in the context of reactor safety research.

Factors affecting the development of explosive mixtures and determining the strength of a steam explosion are given by:

- Fragmented melt mass in water mixture due to limited melt delivery,
- Jet breakup determining the melt drop size and the melt fraction which can fragment,
- Void buildup during premixing inhibiting pressure escalation during the detonation,
- Solidification at the surface of melt drops during premixing, reducing the participating melt and
- Reflection and venting processes during the detonation, affecting the pressure escalation and buildup of shockwaves.

Asymmetries caused by geometrical constraints and confinements (e.g. wall proximity, distributed melt pouring), which are likely during an accident with core melting, may have a strong impact on the explosion development by affecting the interaction of melt and coolant during both premixing and explosion stages. In the past, asymmetric configurations have been investigated with 2D models using 2D approximations. Questions regarding the mixing of fragmented melt, water and steam and thus the mixture explosiveness still remained open due to uncertainties existing with the 2D approach. The 2D approximations which were used, may not deliver a satisfactory representation of the role of geometrical restrictions on the extent of mixing. In order to provide an adequate answer to the influence of geometrical restrictions and predict the explosion strength in a conservative manner, the two-dimensional premixing and explosion codes IKEJET/IKEMIX and IDEMO have been extended to 3D in the present work. Additionally to the 3D extension, further

modeling adaptations were needed with regard to their applicability to real reactor conditions:

- Modification of the jet-breakup modeling for reactor scenarios with long melt jets in deep water pools,
- Representation of melt drops during the mixing with coolant using a Lagrangian approach,
- Solidification of melt drops and crust growth at the drop surface using a temperature drop approach and
- Modeling of different fine-fragmentation behavior of melt drops with different crust thicknesses during the explosion phase.

The extended premixing model JEMI has been presented in Chapter 4. JEMI is a suitable tool for the analysis of the phenomena of mixing of molten fuel in water with strong steam production. The model includes a description of the entry of molten fuel into water in the form of jets, the fragmentation of a melt jet under film boiling, heat transfer from very hot melt fragments to water, strong evaporation and re-condensation processes as well as solidification of melt drops. The focus has been particularly on applicability to real reactor conditions: pouring of large melt masses into a deep water pool very close to the vessel or cavity wall. The delivery of large melt masses might occur after the failure of the reactor vessel resulting in large breaks with a consequent melt outflow due to a moderate overpressure inside the RPV. Scenarios with large melt masses are expected to inflict severe damage due to more melt being available for energy release causing potentially strong pressure escalations and loads on the surrounding structure. Large melt outflow rates lead to thick and long melt jets. This has required a modification of the jet breakup modeling used in IKEJET/IKEMIX, in order to avoid melt fragments that would be too small (~1 mm and smaller) in the premixing due to direct coupling of the drop size and upward steam velocity in the vapor film around the melt jet. Furthermore, the Lagrangian approach used for the melt drops in the premixing allows one to track of each drop with regard to its location, velocities, temperatures and crust thickness. The solidification of melt fragments, i.e. crust development, has been modeled using the temperature drop approach assuming two different temperature profiles for the liquid and solid boundary layers. The storage of latent heat is assumed at the solidification front corresponding to the melting temperature and is represented as a line source of heat. The solidification at the surface of melt drops represents a limitation for fine fragmentation during the explosion phase.

The extended explosion model IDEMO-3D has been represented in Chapter 5. The detonation model implemented in IDEMO has been carried over into IDEMO-3D by merely extending it to 3D. With the objective of examining differently solidified melt fragments from the premixing phase, a discretization of the crust thickness for the melt has been implemented. The effect of a thin solidified layer at the surface on the

fine fragmentation ability for melt drops has been covered using a crust stability criterion. The stiffness and elasticity of the crust at the drop surface is considered as the stabilizing force against the disruptive hydrodynamic force due to fluid movement. Thus, once the solid crust develops at the surface of a melt droplet, the crust stability criterion determines the ability of this droplet to participate in fine fragmentation.

In Chapter 6, verification and validation calculations have been performed. The verification of the premixing model JEMI is based on the experimental results performed in the FARO experimental facility at JRC. At first, separate evaluations for partial models have been performed. The aim was first of all to verify the separate JEMI modules to guarantee a correct prediction of partial aspects. Evaluations of the jet breakup, i.e. the coherent jet length and resulting droplet size, have been made by the modified IKEJET module for jet fragmentation in water with film boiling. The feedback with the surrounding mixture states was not included in this separate analysis. The evaluation has showed that the fragmentation process is similar in all FARO tests due to the similarity of particle size distribution found in the loose debris. Especially, for low pressures, expected in reactor scenarios with core melting, jet fragmentation showed a good agreement with the experiments. The modeling of jet breakup used in JEMI offers an adequate description of jet breakup in water with film boiling for the coherent jet lengths and resulting fragment sizes. Further, separate evaluations of the new solidification model CFOR presented in Chapter 4.7 have been performed for common drop sizes expected in accidents with vapor explosion in reactor scenarios. The CFOR model is a one-dimensional analytical solution describing the development of the temperature profile inside a spherical droplet due to heat exchange with coolant and the progress of the solidification front from the surface into the droplet. Droplet sizes of 3 and 5 mm with corium material properties have been chosen to show the ability of the separate solidification modules to resolve the development of the surface temperature and the thickness of the solid layer at the droplet surface (crust). The surface temperature is necessary in the premixing phase to determine the heat exchange between melt and coolant over the surface. The crust thickness is required in the explosion phase to assess the mechanical stability of the drop against hydrodynamic disturbances at the surface and ability to fragment finely. The calculation results of the analytical solution CFOR have been compared with a numerical solution. The comparison results have shown a good agreement between both solutions. Deviations have been noticed after 78% of the entire drop is already solidified. Thus, CFOR represents a good tool to predict the surface temperature drop and the solidification of melt fragments during their mixing with coolant.

The JEMI validations of the complete code have been made using the FARO L-24, L-28 and L-31 experiments. The chosen experiments give relatively detailed results which allow critical checking by comparison with test. In particular, a long melt pouring duration of ~ 5 s in FARO L-28 and initial (outlet) jet diameter of 5 cm, allow the establishment of clear conditions. Generally, long melt pouring durations of

several seconds and thick melt jets (10 cm to 40 cm of jet diameter) are considered as representative for reactor conditions with respect to large melt outflow rates, high temperatures and material properties (i.e. corium) as used in the FARO tests. A comparison of the obtained particle size distributions with experimental data from FARO showed satisfactory agreement. However, the calculated size distribution lacks sufficient resolution for smaller particles. Nevertheless, the average calculated particle sizes fall well within the experimental band width. The present modeling of jet breakup aims to yield information on the fraction of melt broken up into droplets. It also aims to furnish indications on the dominant particle sizes that can be considered as generally applicable for void generation in the premixing phase. A full description of the whole particle size range is not considered. A good agreement has been achieved calculating the average void fraction and the system pressure increase. The pressure development is the main indication of steam production, and of the heat exchange between melt and coolant. Too high void in the mixture chokes the steam production and too low void means that less steam is produced. Both lead to a slowing of the pressure increase and to an underestimation of steam production. The void in the mixture is an important indication for the validity of the modeling of all mixing processes, including the jet fragmentation, drop size, mixture extent and heat transfer. The information on the void fraction and drop size is required in explosion calculations.

The IDEMO-3D verifications are based on the KROTOS experiments performed at JRC. KROTOS tests have been performed with various stimulant materials such as tin, Al_2O_3 and prototypical corium mixture (80 w% UO2 + 20 w% ZrO2). These tests provide unique experimental data base on steam explosions considered essential for the model development. The alumina melt produces a coarse mixture with large fragments independently of water sub-cooling, being able to produce a vapor explosion either triggered or spontaneously. Corium melts produce a mixture with relatively fine fragments. No spontaneous steam explosion is produced by the tests with corium. Moreover, higher pressures have been measured with alumina melts up to 100 MPa, while the corium melts yielded rather moderate pressure increases up to 20 MPa. Experimental results have led to the conclusion that jet fragmentation during the premixing and the material properties of alumina and corium melts are the reason for the discrepancy in the explosion strength. A closer examination of this difference has been the major focus of KROTOS tests and the validation calculations in the scope of this verification. Three KROTOS tests are considered as suitable basis for the verification of IDEMO-3D: KROTOS K-44, K-52 and K-58. The IDEMO-3D code uses the same modeling as its predecessor 2D code version IDEMO. In the present work, it is enhanced with regard to the three-dimensionality and the consideration of drop solidification during premixing. The chosen tests provide a detailed experimental data on explosion propagation forming a good base for validation of models. Detailed information for important results exists, e.g. the debris size distribution, no irregularities are observed, which are responsible for the observed differences in the

resulting loads between alumina and corium melts. The initial conditions for the calculations with IDEMO-3D have been obtained with the premixing model JEMI. The premixing data (i.e. melt fraction, solidification status of each particle, steam content, and pressures) have been converted as input data into IDEMO-3D. The premixing calculations have been considered as an additional verification of the premixing model JEMI. The aim of the coupled investigation was to check the capability to predict the pressure loads obtained in the experimental facility in the adequate range and indicate the important factors yielding the difference between the corium and alumina melts with respect to the obtained pressure loads. A good agreement regarding the pressure escalation and propagation has been achieved with K-44 using the stimulant melt Al_2O_3. Solidification of melt drops of ~9 mm has not occurred in the premixing stage. This is due to a larger drop size, higher thermal conductivity and higher solidification enthalpy of Al_2O_3 drops compared with corium. The verification analysis based on K-52 and K-58 using corium has shown a satisfying agreement concerning the pressure increases and propagations. The range of the pressure loads could be reproduced with some deviations caused by the initial pressure impulse from triggering. The experimental results have given a definite explanation for the differences between the alumina and corium melts. The solidification of melt drops in the tests with corium is a key limitation for the explosion. In the calculations, only ~20% of the entire melt mass entered the water has had no crust at the surface. The mass fraction with crust thickness below 10% of radius (low-crusted) was ~58%. The propagation velocities in tests with corium were lower than those in tests with Al_2O_3, reducing fine fragmentation ability of low-crusted particles. Generally, the IDEMO-3D have shown a good ability to predict pressure loads within an adequate range using coupled solutions with JEMI. It can be used for investigation of reactor scenarios.

Calculations on reactor relevant configurations have been presented in Chapter 7. The aim was to assess the impact of asymmetry in real reactor conditions. For this, a non-symmetric ex-vessel configuration with a single melt outflow from a failed reactor vessel was considered by varying the melt entry and water pool configuration. The melt delivery was varied between 188 kg/s and 3016 kg/s; the pool filled with saturated water was considered with depth of 1 m and 2 m. The defined configurations were investigated in 2D and 3D geometries. This primarily addresses the extent and distribution of the melt and voids under the impact of geometrical restrictions, in this case, the wall cavity. The extent of the mixture has been considered as a key characteristic of the mixture explosiveness. Spatial extents of the mixture (e.g. stretching and dilution of mixing region) affect the melt concentration and steam content in the mixture. Melt concentrations indicate the energy amount which may be potentially released; the steam acts as a limiting factor for pressure increase and shock wave propagations due to its high compressibility. Concentration of melt fragments leads locally to an increase in explosiveness. The void reduction always brings with it as a consequence an increase in pressure loads. The proximity

of structures, such as the cavity wall, potentially leads to an increase in melt concentrations at these locations. This can cause significantly higher loads on these structures leading to their potential failure. High melt concentrations also cause intense evaporation and local pressure buildup. The latter affects the mixture, thus potentially displacing and deforming the void and melt clouds.

During the mixing of melt and coolant, the investigations performed with 2D and 3D geometries have shown no significant effect of the asymmetry on the mixture extent in the typical considered 3D reactor case. The 2D and 3D have shown a very good agreement with the experimental results in particular with respect to the jet fragmentation and the void in the mixture. The solidification of fragmented melt has been obtained in cases with delayed triggering. No significant displacement or deformation of the mixing zone under local pressure buildups has been observed. The explosion calculations with the premixing data have shown that the explosion strength was slightly overestimated in the 2D geometry. Here, significantly higher pressure peaks have resulted. However, the pressure peaks were very short and contributed little to the final impulses. Concluding the achieved results, the 2D approximations have shown a satisfactory capability to predict the melt fragmentation in water, distribution of fragmented melt, solidification of melt drops and void production even in distinctive 3D reactor cases.

The investigations with a single melt pour close to a wall have shown no significant 3D effect and a good agreement with the 2D approximate investigations. Hence, an additional asymmetric reactor case is considered: a multiple melt outflow from the reactor vessel close to the cavity wall. This reactor scenario has postulated an ex-vessel accident scenario with a circumferentially breaking RPV due to thermal loads and lateral corona-like melt outflow (five aligned melt jets in contact) into the cavity filled with saturated water. The melt delivery has been assumed 940 kg/s and the water pool has been varied between 1 m and 2 m. The principal result has been significantly more fragmented melt compared to the single jet configurations due to initial partitioning of the melt entry into five single melt pours. This is due to an increase of the total strip-off surface area of the inflowing melt. The stronger jet breakup has provided a denser mixture with high melt fraction supporting a strong evaporation. While the multi-jet scenarios have yielded more fragmented melt in absolute terms, percentally a very small melt fraction (in relation to the total mass) was in the regions with void below 30% and 40%. For this reason, the pressure peaks up to 65 MPa have been shorter than those in case of single jet. The pressure impulses have correlated with the single jet configurations with melt outflow of 3016 kg/s. This makes factor 3. Considering the asymmetry, 3D effects caused by the cavity wall (i.e. spatial deformation of the mixing zone) have occurred in the case with delayed triggering (pool depth of 2 m) causing a longer mixing time. The mixture has been deformed in radial direction to the water-rich region due to local pressure buildup in the regions at the wall and between the melt jets. As consequence, the initially stretched mixing zone has become nearly round.

In general it can be concluded, that JEMI and IDEMO-3D are available as suitable tools for investigations of steam explosions for real reactor applications as well as separate effects determining the explosion strength. No significant 3D effect during the premixing has been obtained in asymmetric single-jet configurations. Deformations induced by a close cavity wall have occurred in the case with the multiple pours into the deepest water pool. Taking into account the melt amount entered into water, the multi-jet configurations have provided significantly higher pressure loads and impulses, and can be considered as most critical. Since the highest pressure loads have occurred at the water surface, further theoretical investigations are necessary for ex-vessel scenarios, where the lower plenum of the RPV is partially arrested by water. Such configurations might yield higher loads on the RPV with a consequence of integrity failure of the RPV or creating of missiles.

9 List of References

[1] N.E. Todreus, M.S. Kazimi. Nuclear System I: Thermal Hydraulics Fundamentals. Massachusetts Institute of Technology, Taylor & Francis Group, New Your, 1990. ISBN 1-56032-051-6, pp. 64-70.

[2] INES: The International Nuclear Safety Scale, User's Manual, Revised and Extended Edition 1992, Vienna 1992.

[3] U.S. Nuclear Regulatory Commission Regulations: Title 10, *Code of Federal Regulations*. § 50.47.

[4] Swiss Nuclear Environment Regulation 732.112.2: Verordnung des UVEK vom 17. Juni 2009 über die Gefährdungsannahmen und die Bewertung des Schutzes gegen Störfälle in Kernanlagen. SR-Nr. 732.112.2, 17. Juni 2009, Switzerland.

[5] W. Eggleston. Canada's Nuclear Story. Clarke, Irwin & Company, Toronto, 1965.

[6] A.W. Cronenberg, R. Benz. Vapor Explosion Phenomena with Respect to Nuclear Reactor Safety Assessment, US Nuclear Regulatory Commission/ CR.O245-TREE-1242, 1978.

[7] P.T. Speis, S. Basu. Fuel-Coolant Interaction (FCI) Phenomena in Reactor Safety: Current Understanding and Future Research Needs. In: Proceedings of the OECD/CSNI Specialists Meeting on Fuel-Coolant Interactions, Tokai-Mura, Japan, May 19-24, 1997.

[8] GRS, Gesellschaft für Anlagen und Reaktorsicherheit mbH, 1996. The Accident and the Safety of RBMK-Reactors, February 1996.

[9] N. Fujii. Various styles of intense multiphase interactions viewed from volcanic explosions. Proc. US (Natl. Sci. Found.-Japan (Jpn. Soc. Promo. Sci.) Joint Seminar. June 9–13, 1995. Santa Barbara, California, USA, 1995.

[10] M. Bürger, S.H. Cho, D.S. Kim, C. Carachalios, G.Fröhlich, K. Müller, H. Unger, 1985. Effect of solid crusts on the hydrodynamic fragmentation of melt drops. Final Report, IKE 2 TF-74, June,1985.

[11] M. Bürger, M., S.H. Cho, C. Carachalios, K. Müller, H. Unger., H. Jacobs, 1986. Effect of solid crusts on the hydrodynamic fragmentation of melt drops. Science and technology of fast reactor safety, BNES, London, 1986.

[12] L.S. Nelson, P.M., Duda. Steam explosion experiments with single drops of iron oxide melted with a CO_2 laser. Parametric studies. NUREG/CR-2718, Sandia National Laboratories, 1985.

[13] L.S. Nelson, L.D. Buxton. Steam Explosion Triggering Phenomena: Stainless Steel and Corium-E Simulants Studied with a Floodable Arc Melting Apparatus, Sandia Laboratories SAND77-0998, NUREG/CR-0122, May 1978.

[14] L.S. Nelson et al. Steam Explosion Triggering Phenomena; Part 2: Corium-A and Corium-E Simulants and Oxides of Iron and Cobalt Studied with a Floodable Arc Melting Apparatus, Sandia Laboratories SAND79-0260, NUREG/CR-0633, May 1980.

[15] L.S. Nelson. Steam Explosion Studies with Single Drops of Modlten Refractory Materials, ANS Thermal Reactor Safety Meeting, Knoxville, TN, April 1980.

[16] G. Fröhlich, H. Unger. Investigation of Steam Explosion for Prevention of Severe Accidents in Plants. Assoc. for Structural Safety and Reliability, pp. 597-601, New York, USA, 1985.

[17] L.D. Buxton, W.B. Bendedick. Steam Explosion Efficiency Studies;: Corium Experiments, Sandia Laboratories SAND79-1399, NUREG/CR-0947, November 1979.

[18] W.B. Bendedick, L.D. Buxton, M.L. Corradini. Steam Explosion Efficiency Studies; Part 2: Corium Experiments, Sandia Laboratories SAND79-1399, NUREG/CR-0947, November 1979.

[19] D. Magallon, H. Hohmann. High Pressure Corium Melt Quenching Tests in FARO. Nuclear Engineering and Desing, 155, pp. 123-270, 1995.

[20] D. Magallon, H. Hohmann. Experimental Investigation of 150-kg-scale Corium Melt Quenching in Water. Nuclear Engineering and Desing, 177, pp. 321-337, 1995.

[21] I. Huhtiniemi, D. Magallon, H. Hohmann. Results of recent KROTOS FCI Tests: Alumina vs. Corium Melts, Nuclear Engineering and Design 189, 379-386, 1999.

[22] A. Kaiser, W. Schütz, H. Will: PREMIX TEST PM12, PM14 and PM14 Description and First Results, IRS-4-Notiz Nr. 1409/98, 16. June 1998.

[23] A. Kaiser, W. Schütz, H. Will: PREMIX Tests PM12, PM13 and PM14, Documentation of Experimental Results, FZK-Bericht on Printing, INV-MFCI (99) D050, 1999.

[24] A. Kaiser, W. Schütz, H. Will: PREMIX 15, Description. Data Report and First Results, IRS-4-Notiz Nr. 1445/99, 7. INV-MFCI (99) D049, July 1999.

[25] A. Kaiser, W. Schütz, H. Will: PREMIX-16, Description, Data Report and First Results, IRS-4-Notiz Nr. 1431/99, 15. INV-MFCI (99) D031, March 1999.

[26] A. Kaiser, W. Schütz, H. Will: PREMIX-17, Description, Data Report and First Results, IRS-4-Notiz Nr. 1440/99, INV-MFCI (99) D036, June 1999.

[27] M.F. Young. IFCI: An Integrated Code for Calculation of All Phases of Fuel-Coolant-Interactions. NUREG/CR-5084, SAND87-1048, 1987.

[28] F.K. Davis, M.F. Young. Integrated Fuel-Coolant Interaction (IFCI 6.0) Code. NUREG/CR-6211, SAND94-0406,1994.

[29] M.F. Young. The TEXAS Code for Fuel-Coolant Interaction Anylsis. Liquid Metal Fast Breeder Reactor Safety Topical Meeting, Lyon, France, 1982.

[30] C.C. Chu et al. A Code Manual for TEXAS-V: One Dimensional Transient Fluid Model Fuel-Coolant Interaction Analysis. Revision June 1996.

[31] W.W. Yuen, T.G. Theofanous. PM-ALPHA: A Computer Code for Addressing The Premixing of Steam Explosion. DOE/ID-10502, 1995.

[32] T.G. Theofanous, W.W. Yuen. ESPROSE.m: A Computer Code For Addressing The Escalation/Propagation of Steam Explosions. DOE/ID-10501, 1995.

[33] T.G. Theofanous, W.W. Yuen, K. Freeman, X. Chen. The Verification Basis of the ESPROSE.m Code, Nuclear Engineering and Design, vol. 189, pp. 103-138, 1999.

[34] C. Brayer, G. Berthoud. First Vapor Explosion Calculations Performed with the MC3D Code. In: Proceedings of the OECD/CSNI Specialists Meeting on Fuel-Coolant, Interactions, Tokai-Mura, Japan, May 19-24, 1997.

[35] R. Meignen. MC3D Version 3.5: Description Of The Physical Models Of The PREMIXING Application. NT/DSR/SAGR/05-66, Directions de la Sûreté des Réacteurs, IRSN, France, 2006.

[36] K. Moriyama, N. Yamano, Y. Maruyama, T. Kudo, J. Sugimoto, J. Study of Premixing Phase of Steam Explosion with JASMINE Code in ALPHA Program. In Proceedings of 4th International Conference on Nuclear Engineering, New Orleans, volume 1B, pp. 903–915, 1996.

[37] K. Vierow, K. Nagano, K. Araki. Development of the VESUVIUS Module: Molten Jet Break-up Modelling and Model Verification. In: Proceedings of the OECD/CSNI Specialists Meeting on Fuel–Coolant Interactions, Tokai-Mura, Japan, May 19–21, pp. 541–566.

[38] C.C. Chu et al. Ex-Vessel Melt Coolant Interactions in Deep Water Pool: Studies and Accident Management for Swedish BWR's. Nuclear Engineering and Design, 155, pp. 159-213, 1995.

[39] C.C. Chu et al. Comparison of THIRMAL-1 Predictions with FARO and CCM Experiments, Transactions of the ANS. Vol. 71, 1994.

[40] G. Pohlner, Z. Vujic, M. Bürger G. Lohnert. Simulation of Melt Jet Break-up and Debris Bed Formation in Water Pools with IKEJET/IKEMIX. Nuclear Engineering and Design 236, pp. 2026-2048, 2006.

[41] M. Buck. Weiterentwicklung und Verifikation des thermischen Detonationsmodell IDEMO, Diploma Thesis, IKE, Universität Stuttgart, Report IKE 2D-110, Aug. 1994.

[42] M. Buck, M. Bürger. IDEMO - A Thermal Detonation Model of Vapor Explosions: Multi-Fluid Model, Constitutive Laws and Verification Lines. In: Proceedings of the 2nd Japanese-German Symposium on Multi-Phase Flow, Tokyo, September 25-27, 1997.

[43] Magallon, D. et al.: OECD Programme SERENA (Steam Explosion REsolution for Nuclear Applications) Work Programme and First Results, Proc. of NURETH-10, Seoul, Korea, October 5-11, 2003.

[44] D. Magallon. OECD Programme SERENA (Steam Explosion Resolution for Nuclear Applications) Task 2, Reference Data for Calculation of FARO Tests L-28, L-31 and L-33. Internal Report, 2002.

[45] D. Magallon. Formation and Characterisation of Corium Debris Arising From Fuel–Coolant Interaction. Nuclear Engineering and Design 236, pp. 1998–2009, 2006.

[46] R. Silverii, D. Magallon. FARO LWR PROGRAMME, Test L-28 Data Report, Technical Note No.I.99.76, INV-MFCI(99)-D033, European Commission, Joint Research Centre, Ispra Site, April, 1999.

[47] S.J. Board, R.W. Hall. Recent Advances in Understanding. Large Scale Steam Explosions. In: Proceedings of the 3rd Specialist Meeting on Sodium-Fuel Interactions in Fast Reactors, Tokyo, PNC N251, 76-12, pp. 249-283, 1976.

[48] M.L. Corradini. Analysis and Modeling of Steam Explosion Experiments. Sandia National Laboratories, SAND80-2131, NUREG/CR-2072, April 1981.

[49] M.L. Corradini. Analysis and Modeling of Large-Scale Steam Explosion Experiments. Nuclear Science and Engineering, vol. 82, pp. 429-447, 1982.

[50] M.L. Corradini et al. Vapor Explosions in Light Water Reactors: A Review of Theory and Modeling. Progress in Nuclear Energy, 22(1), pp. 1-117, 1968.

[51] M. Bürger, S.H. Cho, E.v. Berg, A. Schatz. Break-up of Melt Jets as Pre-condition for Premixing: Modeling and Experimental Verification. Nuclear Engineering and Design 155, pp. 215-251, 1995.

[52] Y. Abe, E. Matsuo, T, Arai, H. Nariai, K. Chitose, K. Koyama, K. Itoh, 2006. Fragmentation behavior during molten material and coolant interactions, Nucl. Eng. Design vol. 236, pp. 1668-1681, 2006.

[53] T. Ginsberg. Liquid Jet Breakup Characterization with Application to Melt-Water Mixing. ANS Proc. National Heat Transfer Conference, Denver, USA,1985.

[54] E. Matsuo, Y. Abe, K. Chitose, K. Koyama, K. Itoh. Study on jet breakup behavior at core disruptive accident for fast breeder reactor. Nuclear Engineering and Design 238, pp. 1996–2004, 2008.

[55] K.H. Bang, J.M. Kim, D.H. Kim. Experimental Study of Melt Jet Breakup in Water. Journal of Nuclear Science and Technology, vol. 40, No. 10, pp. 807-813, 2003.

[56] J.W. Strutt, Lord Rayleigh. On The Instability of Jets. Proceedings of the London mathematical society, vol. 10, pp. 4-13, London, 1878.

[57] T.G. Theofanous, W.W. Yuen and T.N.Dinh. Calculations of Pre-Mixing Experiments With the PM-ALPHA.L.3D code. Part1: Calculation of FARO L-28 experiment. CRSS-02/12-02, Center for Risk Studies and Safety, University of California, Santa Barbara, CA, USA, 2002.

[58] T.N. Dinh, V.A. Bui, R.R. Nourgaliev, J.A. Green, B.R. Sehgal. Experimental and Analytical Studies of Melt Jet-Coolant Interactions: A Synthesis. Nuclear Engineering and Design, vol. 189, pp. 299-237, 1999.

[59] L.S. Nelson, L.D. Buxton. Steam Explosion Triggering Phenomena: Stainless Steal and Corium-E Simulants Studied with a Floodable Arc Melting Apparatus, Sandia Laboratories SAND77-0998, NUREG/CR-0122, May 1978.

[60] L.S. Nelson et al. Steam Explosion Triggering Phenomena; Part 2: Corium-A and Corium-E Simulants and Oxides of Iron and Cobalt Studied with a Floodable Arc Melting Apparatus, Sandia Laboratories SAND79-0260, NUREG/CR-0633, May 1980.

[61] Y. Abe, H. Nariai, Y. Hamada. The Trigger Mechanism of Vapor Explosion. Journal of Nuclear Science and Technology, vol. 39, No. 8, pp. 845-853, 2002.

[62] M. Schröder, Z. Vujic, G. Pohlner, M. Buck, M. Bürger, G. Lohnert. Investigation of Main Limiting Effects to Strong Steam Explosions in 3D Geometry Considering Real Accident Scenarios. In Proceedings of the Conference Nuclear Energy for New Europe, Lubljana, Slovenia, 15.-17. Sep 2009.

[63] M. Bürger, G. Pohlner, M. Buck, M. Schröder. Abschlussbericht zum Forschungsvorhaben BMWA 1501266, Institut für Kernenergetik und Energiesysteme (IKE), Universität Stuttgart, Bericht IKE 2-151, September 2004.

[64] M. Bürger, M. Buck, Z. Vujic: Stand der Arbeiten zur Vorvermischung, Zwischenbericht zum Vorhaben BMWA 150 1266, IKE 2-151, Universität Stuttgart, Februar, 2005.

[65] M. Schröder. Three Dimensional Modelling and Simulation of Steam Explosion – Need for Three Dimensional Analyses and First Development Steps.Jahrestagung Kerntechnik, Aachen, 16.-18. Mai 2006.

[66] M. Bürger, M. Buck, M. OECD Programme SERENA (Steam Explosion Resolution for Nuclear Applications), Analyses of Task 2 Calculation Results. Internal Report, 2005.

[67] M. Ishii and N. Zuber: Drag Coefficient and Relative Velocity in Bubbly, Droplet or Particulate Flows. AIChE J. 25 (1979) 843.

[68] Z. Vujic, M. Bürger, M. Buck, G. Lohnert. Investigation of Limitations to Steam Explosions Strength due to Water Depletion. In: Proceedings of the 15th International Conference on Nuclear Engineering (ICONE15), Nagoya, Japan, April 22-26, 2007.

[69] Bürger M., Pohlner G., Vujic Z.: Stand der Arbeiten zur Vorvermischung. Zwischenbericht zum Forschungsvorhaben BMWA 1501266, Institut für Kernenergetik und Energiesysteme (IKE), Universität Stuttgart, Bericht IKE 2-151, September 2004.

[70] L.S. Carreto, A.D. Gosman, S.V. Patankar, S.B. Spalding. Two calculation procedures for steady, three-dimensional flows with recirculation. In proceedings of the 3rd International Conference Numerical Methods of Fluid Dynamics, Paris, France, 1972.

[71] M. Epstein, G. Hauser. Subcooled Forced-Convection Film Boiling in the Forward Stagnation Region of a Sphere or Cylinder. International Journal of Heat and Mass Transfer 23, pp. 179–189, 1980.

[72] M. Leskovar, R. Meignen, C, Brayer, M. Bürger, M. Buck, Material influence on steam explosion efficiency: state of understanding and modelling capabilities, The 2nd European Review Meeting on Severe Accident Research (ERMSAR-2007), June 12-14, 2007, FZK, Karlsruhe, Germany, 2007.

[73] T. Okkonen, B.R. Sehgal. “Influence of Melt Freezing Characteristics on Steam Explosion Energetics”, Proc. ICONE Conference, 1, pp. 923-934, 1996.

[74] K. Moriyama, H. Nakamura, Y. Maruyama. Analytical Tool Development for Coarse Break-Up of a Molten Jet in Deep Water Pool. Nuclear Engineering and Design, 236, pp. 2010–2025, 2006.

[75] M. Buck, M. Bürger, Z. Vujic: OECD Programme SERENA (Steam Explosion Resolution for Nuclear Applications) Task 3, Comparison of various approaches for calculating explosions. Step 1, Calculation of explosion experiments. Description of the thermal detonation model IDEMO-2D. Contribution of IKE, Universität Stuttgart.

[76] M. Bürger, M. Buck, Z. Vujic. Stand der Arbeiten zur Explosionsphase. Zwischenbericht zum Vorhaben BMWA 150 1266, IKE Universität Stuttgart, Report: IKE 2-155, Oktober 2007.

[77] Z. Vujic. Improvement and Verification of Steam Explosion Models and Codes for Application to Accident Scenarios in Light Water Reactors. PhD Thesis,

Institute of Nuclear Technology and Energy Systems (IKE), University of Stuttgart, 2008.

[78] M. Pilch, C.A. Erdman, A.B. Reynolds. Acceleration induced fragmentation of liquid drops, Charlottesville, VA: Department of Nucl. Eng., University of Virginia, NUREG/CR-2247, 1981

[79] R.R. Schröder, R.C. Kitner. Oscillation of drops falling in liquid field, A.I.Ch.E. Journal, vol 11 no 1 pp 5-8, 1965

[80] N.I. Kolev. Multiphase Flow Dynamics 2. Thermal and Mechanical Interactions. 2nd Edition, Springer Verlag Berlin Heidelberg, 2005

[81] D. F. Fletscher. Propagation investigations using the CULDESAC model. Nuclear Engineering and Design, vol. 155, pp. 271-287, 1995.

[82] M. Epstein. “Stability of a Submerged Frozen Crust”, ASMA Journal on Heat Transfer, Vol.99, pp. 527-532, 1977

[83] M. Cooper and J. Dienes, 1978. The role of Rayleigh-Taylor instabilities in fuel-coolant interactions. Nucl. Science and Eng., vol. 68, pp. 308-321, 1978.

[84] M. Bürger, C. Carachalios, D.S. Kim, H. Unger H. Theoretical investigations on the fragmentation of drops of melt with respect to the description of thermal detonations and their application in the code FRADEMO, *Rep. 10660.* Comm. Eur. Commun. Brussels, 1986.

[85] M. Uršič, M. Leskovar, I. Kljenak, B. Mavko. Modelling of material properties influence in fuel-coolant interaction codes, ICONE17-75039, Proceedings of the 17th International Conference on Nuclear Engineering (ICONE17), July 12-16, Brussels, Belgium, 2009.

[86] I. Huhtiniemi, D. Magallon: Insight into steam explosions with corium melts in KROTOS, Nuclear Engineering and Design 204, 391-400, 2001.

[87] M. Uršič, M. Leskovar, R. Meignen, M. Schröder, M. Buck, M. Bürger. Improved melt solidification influence modelling in Fuel Coolant Interactions, ERMSAR-2010, Bologna, Italy, Mai 2010.

[88] I. Huhtiniemi, H. Hohmann, R. Faraoni, M. Field, R. Gambaretti, K. Klein. KROTOS 38 TO KROTOS 44: Data Report. Technical Note No. I.96.37, March 1996.

[89] H. Esmaili, M. Khatib-Rahbar: Analysis of Likelihood of Lower Head Failure and Ex-Vessel Fuel Coolant Interaction Energetics for AP1000. Nuclear Engineering and Design, vol. 235, pp. 1583-1605, 2005.